Micromechanics of Strength-Related Phenomena in Composite Materials

by

Scott Wayne Case

Thesis submitted to the Faculty of the

Virginia Polytechnic Institute and State University

in partial fulfillment of the requirements for the degree of

Master of Science

in

Engineering Mechanics

Kenneth L. Reifsnider, Chair

Scott L. Hendricks

Demetri P. Telionis

May, 1993

Blacksburg, Virginia

LD
5655
V855
1993
C374
C.2

C.2

ABSTRACT

Micromechanical models are presented which can be used to evaluate: stress concentrations in the vicinity of single and multiple fiber fractures in unidirectional composites under axial loading; the tensile strength of unidirectional composites; fiber coatings that can be used to maximize the transverse strain-to-failure and longitudinal shear strain-to-failure of composites; and the compression strength of composite materials containing embedded cylindrically shaped sensors or actuators. In each case, with the exception of the longitudinal shear model, the micromechanical predictions are compared with the experimental results. In the cases of the fiber fracture model and the transverse strain-to-failure model, these experimental results are obtained by employing a macro-model composite. It is demonstrated that the constituents of the macro-model composite can be systematically altered in order to study physical parameters such as fiber volume fraction and fiber coatings.

ACKNOWLEDGEMENTS

The author wishes to thank the following people for their contribution to this work:

- Dr. Greg Carman, for his encouragement, friendly advice, and confidence in my abilities. without his support this work would not have been possible.
- Jack Lesko who took a chance in hiring me two years ago. His friendship and support have been more than anyone could ask for.
- Dr. K. L. Reifsnider who has helped me by his dedication to the advancement of science and his careful insight to research and life in general.
- Drs. S. L. Hendricks and D. P. Telionis for taking time out of their schedules to serve on my graduate committee.
- Jennifer Elmore, who taught me what true dedication to a friend really is. She always was there to listen when something was wrong.
- Suresh Subramanian for his many insightful and thought provoking comments into research. Just when I thought I knew some of the answers, he showed me that I didn't.
- Ann Fajardo for graciously allowing me access to her senior project data. In addition, her wit and charm have helped to brighten my day many times.
- Charnell Haldeman for aiding me in running the model composite tests. Without her conversation and aid, those nights of testing would have been unbearable.
- Carrie Stephens, Laura Boyer, and Stephanie Slusher for their friendship and advice in the trying times.
- Martin Donnelly for making sure that I didn't work *all* the time. Everyone has to go skiing occasionally...
- Lynessa Smith for keeping me headed in the right direction.
- Sheila Collins, Melba Morrozoff, Paula Lee, and Cindy Hopkins for all their help.
- The fellow members of the Materials Response Group, for their camaraderie and friendship in the past two years.
- The National Science Foundation, for their financial support under Grant No. MSS-9115380.
- Most of all to my parents and family, whose love and support through the years have not gone unnoticed.

TABLE OF CONTENTS

LIST OF ILLUSTRATIONS

LIST OF TABLES

1.0 INTRODUCTION

The failure of composite materials in the presence of general loadings involves a complex interaction between the fiber and the matrix. In addition, the nature of the interface between these two constituents plays an important role in determining the resulting composite strength. Traditional composite failure theories on the lamina level are generally extensions of the isotropic yield criteria (such as von Vises) which include the effects of anisotropy. An example of such an extension is the Tsai and Wu [1] theory. However, these failure theories often require material properties obtained from biaxial tests which in practice are difficult to perform. In addition, recent experimental results presented by Madhukar and Drzal [2 - 4] have shown that the strength of composites are tied directly to micro-level composite properties such as the presence of fiber surface treatments and fiber coatings. As a result, accurate strength predictions require models which address the stress states in fiber and the matrix (as well as any fiber coating which may be present). These *micromechanical* models can then be used in conjunction with macromechanical models to predict laminae and laminate performance.

One such micromechanical model has been presented by Pagano and Tandon [5]. Their fundamental representative volume element consists of three concentric circular cylinders with displacements prescribed on the boundary. These cylinders represent the fiber, any coating which may be present on the fiber surface, and the matrix. By assuming perfect bonding and linear elastic behavior, they are able to determine the stress distribution in the fiber, the coating and the matrix. Although their results consider only a three-phase model, the analysis itself may include any number of phases. The model does not, however, consider the presence of damage in the composite or the effects of fiber-fiber interaction.

Aboudi [6] has presented a micromechanical analysis of the strength of unidirectional fiber composites. The analysis makes use of "artificial" fibers of square cross section arranged in a double periodic array in the matrix. This model is used to determine the transversely isotropic behavior of the composite. Results are presented for predicted failure stresses for different material systems and different fiber orientations with respect to the loading direction. These predictions are made by assuming a maximum stress theory in conjunction with material strengths in the principal directions. The agreement between the predicted failure stresses and the experimentally determined values was shown to be good. However, no basis was given for predicting the failure stresses in these principal directions.

Other researchers have attempted to use concentric cylinder analyses similar to that proposed by Pagano and Tandon to reduce the residual stresses resulting from mismatches in coefficient of thermal expansion (CTE) between the fiber and the matrix. Ghosn and Lerch [7] used a three-phase concentric cylinder model in an attempt to minimize the average distortional energy in the matrix and interphase due to residual stresses in metal matrix composites. Their analysis considered only these residual stresses and did not address the effects of mechanical loading. These results showed that the number of coating possibilities whose modulus and CTE fit the optimized values from the minimization procedure were limited. In order to increase the number of possible coating materials, candidate materials with less than the optimum modulus and CTE were examined. The residual stress state in the matrix and coating were calculated for these materials. However, the benefits of this analysis are questionable. If the goal is solely to minimize residual thermal stresses, this may be accomplished by allowing the fiber coating to be as compliant as possible. However, such a compliant coating may be detrimental to composite performance under mechanical loadings.

Arnold and Wilt [8] used a concentric cylinder model and a three-dimensional finite element model with period boundary conditions representing a hexagonally packed composite to study the effect of a compliant interphase material on the residual stresses in and mechanical response of metal matrix composites. Their analysis included temperature dependent material properties. In addition, they considered the effect of plasticity in the matrix and the interphase material using a Von Mises yield criterion. Their results showed that the compliant interphase had only a minor influence on longitudinal tensile response. Further, the application of this compliant coating produced a slight decrease in the transverse stiffness of the composite systems compared to those systems with no coating.

Carman et al. [9] used a three-phase concentric cylinder model to analyze the stress state in a continuously reinforced coated fiber composite subjected to transverse loading. This analysis did not include the effects of residual thermal stresses in the fiber, interphase, and matrix. By applying a constant strain boundary condition, Carman et al. suggest a criterion by which the modulus of the interphase material may be selected to minimize the principal stresses in the matrix. This suggests that the composite strain to failure may be correspondingly increased. Numerical studies are conducted on a graphite-epoxy composite which shows that the strain to failure may be increased as much as six times by coating the structural fibers with the optimum coating.

In a related study, Carman and Reifsnider [10] use a similar analysis to reduce the stress concentrations in a composite material containing an embedded sensor or actuator (so called *smart* materials). Their analysis uses a three-phase concentric cylinder model consisting of a fiber (the sensor or actuator), a coating, and a surrounding host material. The properties of the host material

are assumed to be those of the bulk composite. Numerical studies are conducted on a graphite-epoxy composite containing a cylindrically-shaped glass sensor. These results suggest that the onset of damage due to the embedded sensor in the composite subjected to transverse loading may be delayed, and may suggest a material system whose transverse strength is nearly that of the host material without an embedded sensor.

In each of the above models, it was assumed that no defects were present in the material. However, in reality there are always defects present in a composite, either due to processing or in-service damage. One of the most common types of damage to be present in a composite material is a fiber fracture. Rosen [11] was one of the first individuals to consider the stress state surrounding a fiber fracture. By assuming that the matrix supports no normal stresses and that the fiber supports no shearing stresses, he was able to formulate what is often referred to as the *shear lag* analysis. This analysis suggests that the stress terms increase exponentially as axial distance increases along the fractured fiber. In addition, by making use of an efficiency parameter which relates the stresses in the vicinity of the fiber fracture to those far removed, it is possible to predict an *ineffective length*--the axial distance over which the stress field is perturbed.

Whitney and Drzal [12] considered the case of a single fractured fiber embedded in an infinite matrix. Their analysis extended the shear lag concepts to include axial loading in the matrix and shearing stresses the fractured fiber. By using the equilibrium equations in conjunction with constitutive relations, and assumed functional dependence of the stresses on the radial and axial coordinates, they were able to formulate an approximate solution to the ineffective length problem. This solution does not satisfy the compatibility conditions. The ineffective lengths calculated using this analysis were compared with experimentally determined values using a single fiber

fracture test for on composite systems to validate the micromechanical model.

Hedgepeth and Van Dyke [13] considered the stress concentrations on neighboring fibers due to single and multiple adjacent fiber fractures. Their analysis used an influence function approach along with shear lag concepts. Results were presented for both three-dimensional square and hexagonal arrays where specified fibers were broken and for the stress concentration factor in a fiber adjacent to a broken fiber in a two-dimensional array where the shear stress in the matrix is restricted by a limiting stress value. Due to the inherent shear lag assumptions, however, the model does not include the effects of the fiber and matrix stiffness values and fiber volume fraction. Therefore, it is applicable to high fiber modulus, low matrix modulus, high fiber volume fraction systems.

Carman et al. [14] attempted to include the effect of fiber volume fraction, material properties, crack size, and fiber eccentricity on the resulting stress concentrations in the vicinity of a fiber fracture. Their analysis represents the fibers adjacent to a fractured fiber by a ring of material. Using an assumed functional dependence of strains in the vicinity of the fractured fiber in conjunction with a mechanics of materials approach and elasticity concepts, an approximate stress field is developed in each of the constituent materials. They present numerical results for stress concentrations with variables such as fiber volume fraction, stiffness values, crack size, and fiber eccentricity. In addition, the analytical predictions are compared with direct experimental measurements obtained from a macro-model composite system. The results are shown to be in good agreement with the analytical predictions.

Fajardo [15] performed an experimental study of fiber fracture in a glass/epoxy composite using

a macro-model composite. In particular, the effects of fiber volume fraction and crack size on stress concentration and ineffective length due to a single fiber fracture were studied. The experimental results were compared with theoretical predictions made using the annular ring model proposed by Carman et al. [14] and the shear lag model [11]. It was shown that the annular ring model provided closer agreement with the experimental results, although both models still overpredicted the ineffective length.

The ultimate goal in modelling the stress concentrations and ineffective length surrounding a fiber fracture is to obtain accurate lamina level tensile strength predictions. Harlow and Phoenix [16] used a statistical analysis in conjunction with an assumed load sharing rule for a single ply tape to predict composite strength for this idealized problem. They considered both the case of the usual Weibull distribution and what they considered to be a more realistic double version which has the effect of putting an upper bound on fiber strength. They found that for typical cases the use of the double Weibull distribution for fiber strength does not affect the behavior of the probability distribution for the strength of composite materials and therefore its use may not be justified. The difficulty in calculating the probability distribution for the two-dimensional case suggests that it would be extremely difficult to extend the analysis to include three-dimensional effects.

Batdorf [17] has presented a somewhat simpler approach to the tensile strength of composite materials. The analysis is based on that proposed by Harlow and Phoenix [16], but through many simplifications the analysis may be used to predict the tensile strength of three-dimensional composite materials. The analysis uses theoretically determined stress concentrations and ineffective lengths due to multiple fiber fractures to estimate the fiber load level at which an

instability occurs. This load level corresponds to the load at which the composite itself experiences catastrophic failure. To study the effects of the simplifications on the predicted strength, a comparison is made to the results published by Harlow and Phoenix [16]. It was shown that the failure stresses predicted by both methods differ by only a few percent, suggesting that the simplifying assumptions did not significantly affect the predictions made by the model.

Gao et al. [18] conducted a study of strength prediction and optimization of composites. Their analysis used a modified shear lag approach in conjunction with the statistical analysis of Batdorf [17] to achieve tensile strength predictions. As part of their shear lag analysis, they showed that there was a direct relationship between stress concentrations due to fractured fibers and ineffective length. In addition, they considered the effects of irregular fiber spacing and the ratio of fiber to matrix stiffness values on the predictions for composite tensile strength. Their analysis suggests that there may be an optimum ineffective length which maximizes the tensile strength.

One advantage that composite materials have is that it is easily possible to embed a sensor or actuator in a laminate. Such embedded sensors have been shown to have the greatest effect on the transverse tensile (see Roberts and Davidson [19] and Carman et al. [20]) and compression (Roberts and Davidson [19]) strengths of the host material. Accurate strength predictions for these materials requires that we understand the factors influencing the geometry in the vicinity of an embedded sensor or actuator. Dasgupta et al. [21] have conducted a linear elastic study of an embedded fiber optic sensor embedded in a composite laminate. By using a Ritz approximation method, they have been able to mathematically represent the undulated region surrounding the embedded sensor. Comparisons are presented between the predicted and actual geometries for various laminae stacking sequences. The results show good agreement for each of the laminate

configurations. No attempt was made to study the effect of these embedded sensors on the composite performance.

The goal of the present study is to expand upon the previous micromechanical models which relate to composite tensile strength. In this thesis, micromechanical models are presented which can be used to evaluate:

- Stress concentrations and ineffective lengths in the vicinity of single and multiple fiber fractures
- Tensile strength of unidirectional fiber composites
- Fiber coatings which can be used to maximize the transverse strain to failure and longitudinal shear strain to failure of composites
- Compression strength of composite materials containing embedded cylindrically shaped sensors or actuators.

In each case, with the exception of the longitudinal shear model, the theoretical predictions are compared with experimental results. In this way we are able to validate the predictions and to gain a greater insight into the processes which control the strength of composite materials. It is hoped that with this insight we can begin to tailor the performance of composite materials to meet specific design criteria without resorting to a "make-it-and-break-it" method of determining the performance.

2.0 CONCENTRIC CYLINDERS FORMULATION

The general assumptions made in the present analysis are as follows. First, we assume that the fiber, interphase, and matrix can be adequately represented by a set of N concentric cylinder elements (see Hashin and Rosen [22]). Second, the fiber, interphase, and matrix are assumed to be linearly elastic with transversely isotropic properties. At the interphase between each of the constituents, we assume that "perfect" bonding exists. This assumption requires that displacements and tractions be continuous at each interface. Finally, we assume that the effective strains experienced by the representative volume element are equivalent to those experienced by the bulk composite. For our analysis, we allow the composite to be subjected to displacements on the boundary of the form

$$u_i(S) = \varepsilon^0_{ij} x_j \tag{1}$$

where S and x_j are the cartesian coordinates of the boundary, $\varepsilon_{ij}^{\,0}$ are constants, and u_i are the components of the boundary displacement. For boundary conditions specified in the form given by Equation 1, it can be shown that

$$\overline{\varepsilon_{ij}} = \varepsilon^0_{ij} = constant \tag{2}$$

where an overbar denotes the average value over the representative volume element (RVE). Based on these statements, the displacements at the boundary of the RVE can be written as (see Pagano and Tandon [5])

$$u_z^N = \varepsilon_{zz}^0 z + \frac{1}{2}\gamma_{yz}^0 r_N \sin\theta + \frac{1}{2}\gamma_{xz}^0 r_N \cos\theta$$

$$u_r^N = \frac{1}{2}\varepsilon_{xx}^0 r_N(1 + \cos 2\theta) + \frac{1}{2}\varepsilon_{yy}^0 r_N(1 - \cos 2\theta) + \frac{1}{2}\gamma_{xy}^0 r_N \cos 2\theta + \frac{1}{2}\gamma_{yz}^0 z \sin\theta + \frac{1}{2}\gamma_{xz}^0 z \cos\theta \qquad (3)$$

$$u_\theta^N = -\frac{1}{2}\varepsilon_{xx}^0 r_N \sin 2\theta + \frac{1}{2}\varepsilon_{yy}^0 r_N \sin 2\theta + \frac{1}{2}\gamma_{xy}^0 r_N + \frac{1}{2}\gamma_{yz}^0 z \cos\theta - \frac{1}{2}\gamma_{xz}^0 r_N \sin\theta$$

where r_N is the outer radius of the *N-th* cylinder element and the u_i in Equation 3 are evaluated at r_N. These boundary conditions dictate the functional dependence of each displacement field on θ and z. To determine the functional dependence of the displacements on r, we utilize the equilibrium equations, the constitutive relations, and the strain-displacement relations. The equilibrium equations in the absence of body forces are given by

$$\frac{\partial \sigma_{rr}^n}{\partial r} + \frac{1}{r}\frac{\partial \sigma_{r\theta}^n}{\partial \theta} + \frac{\partial \sigma_{rz}^n}{\partial r} + \frac{\sigma_{rr}^n - \sigma_{\theta\theta}^n}{r} = 0$$

$$\frac{\partial \sigma_{\theta r}^n}{\partial r} + \frac{1}{r}\frac{\partial \sigma_{\theta\theta}^n}{\partial \theta} + \frac{\partial \sigma_{\theta z}^n}{\partial z} + \frac{2\sigma_{\theta r}^n}{r} = 0 \qquad (4)$$

$$\frac{\partial \sigma_{zr}^n}{\partial r} + \frac{1}{r}\frac{\partial \sigma_{z\theta}^n}{\partial \theta} + \frac{\partial \sigma_{zz}^n}{\partial z} + \frac{\sigma_{zr}^n}{r} = 0$$

Letting the indices 1, 2, 3, 4, 5, and 6 refer to z, r, θ, $r\theta$, $z\theta$, and rz, respectively, we obtain the stress-strain relations for the *n-th* transversely isotropic cylinder

$$\begin{aligned}
\sigma_{zz}^n &= C_{11}^n(\varepsilon_{zz}^n - e_{zz}^n) + C_{12}^n(\varepsilon_{rr}^n - e_{rr}^n) + C_{12}^n(\varepsilon_{\theta\theta}^n - e_{\theta\theta}^n) \\
\sigma_{rr}^n &= C_{12}^n(\varepsilon_{zz}^n - e_{zz}^n) + C_{22}^n(\varepsilon_{rr}^n - e_{rr}^n) + C_{23}^n(\varepsilon_{\theta\theta}^n - e_{\theta\theta}^n) \\
\sigma_{\theta\theta}^n &= C_{12}^n(\varepsilon_{zz}^n - e_{zz}^n) + C_{23}^n(\varepsilon_{rr}^n - e_{rr}^n) + C_{22}^n(\varepsilon_{\theta\theta}^n - e_{\theta\theta}^n) \qquad (5) \\
\sigma_{r\theta}^n &= C_{44}^n \gamma_{r\theta}^n \\
\sigma_{\theta z}^n &= C_{55}^n \gamma_{\theta z}^n \\
\sigma_{rz}^n &= C_{55}^n \gamma_{rz}^n
\end{aligned}$$

where C_{ij} are the elastic stiffness constants of the individual materials and e_z, e_r, and e_θ are the expansional (non-mechanical) strain components along the longitudinal (z) and transverse (r - θ) directions, respectively. Further, for a transversely isotropic material,

$$\begin{aligned} e_r &= e_\theta \\ C_{44} &= \frac{1}{2}(C_{22} - C_{23}) \end{aligned} \tag{6}$$

The engineering strain-displacement relations are given by

$$\begin{aligned} \varepsilon_{zz}^n &= u_{z,z}^n \\ \varepsilon_{rr}^n &= u_{r,r}^n \\ \varepsilon_{\theta\theta} &= \frac{1}{r}u_{\theta,\theta}^n + \frac{1}{r}u_r^n \\ \gamma_{r\theta}^n &= \frac{1}{r}u_{r,\theta} + u_{\theta,r} - \frac{1}{r}u_\theta^n \\ \gamma_{rz}^n &= u_{z,r}^n + u_{r,z}^n \\ \gamma_{\theta z}^n &= u_{\theta z}^n + \frac{1}{r}u_{z,\theta} \end{aligned} \tag{7}$$

Pagano and Tandon [5] have shown that the generalized displacement fields for each constituent corresponding to the boundary conditions prescribed in Equation 1 can be written as

$$\begin{aligned} u_r^n(r, \theta, z) &= U_1^n(r)\cos 2\theta + U_2^n(r)\sin 2\theta + U_3^n(r) \\ &\quad + U_4^n(r)\, z\cos\theta + U_5^n(r)\, z\sin\theta \\ u_\theta^n &= V_1^n(r)\sin 2\theta + V_2^n(r)\cos 2\theta + V_4^n(r)\, z\sin\theta + V_5^n(r)\, z\cos\theta \\ u_z^n &= zW_3^n(r) + W_4^n(r)\cos\theta + W_5^n(r)\sin\theta \end{aligned} \tag{8}$$

where n = 1, 2, ... N, and $U_1^n(r)$, $U_2^n(r)$, ... $W_5^n(r)$ are defined as

$$
\begin{aligned}
U_1^n(r) &= A_1^n r^3 + \frac{A_2^n}{r^3} + A_3^n r + \frac{A_4^n}{r^4} \\
V_1^n(r) &= -\frac{(3C_{22}^n + C_{23}^n)}{2C_{23}^n} A_r^n r^3 + \frac{A_2^n}{r^3} - A_3^n r + \frac{(C_{23}^n - C_{22}^n)}{2C_{22}^n r} A_4^n \\
U_2^n(r) &= B_1^n r^3 + \frac{B_2^n}{r^3} + B_3^n r + \frac{B_4^n}{r} \\
V_2^n(r) &= \frac{(3C_{22}^n + C_{23}^n)}{2C_{23}^n} B_1^n r^3 - \frac{B_2^n}{r^3} + B_3^n r + \frac{(C_{22}^n - C_{23}^n)}{2C_{22}^n r} B_4^n \\
U_3^n(r) &= D_1^n r + \frac{D_2^n}{r} \\
W_3^n(r) &= D_3^n \\
U_4^n(r) &= F_4^n \\
V_4^n(r) &= F_3^n \\
W_4^n(r) &= \frac{F_5^n}{r} + F_5^n r \\
U_5^n(r) &= H_4^n \\
V_5^n(r) &= H_3^n \\
W_5^n(r) &= H_5^n + H_6^n r
\end{aligned}
\tag{9}
$$

and A_1^n, A_2^n, ... H_6^n are constants.

By using these displacements in the strain-displacement relations of Equation 7 and the constitutive relations of Equation 5 and Equation 6, Pagano and Tandon formulate the stresses as

$$
\begin{aligned}
\sigma_{zz}^n &= \alpha_1^n(r)\cos 2\theta + \alpha_2^n(r)\sin 2\theta + \alpha_3^n(r) \\
\sigma_{\theta\theta}^n &= \beta_1^n(r)\cos 2\theta + \beta_2^n(r)\sin 2\theta + \beta_3^n(r) \\
\sigma_{rr}^n &= \zeta_1^n(r)\cos 2\theta + \zeta_2^n(r)\sin 2\theta + \zeta_3^n(r) \\
\sigma_{rz}^n &= \delta_4^n(r)\cos\theta + \delta_5^n(r)\sin\theta \\
\sigma_{z\theta}^n &= \xi_4^n(r)\sin\theta + \xi_5^n(r)\cos\theta \\
\sigma_{r\theta}^n &= \gamma_1^n(r)\sin 2\theta + \gamma_2^n(r)\cos 2\theta
\end{aligned}
\tag{10}
$$

where the following definitions are made:

$$\alpha_1^n = -2C_{12}^n C_{44}^n \left[\frac{3A_1^n r^2}{C_{23}^n} + \frac{A_4^n}{C_{22}^n r^2} \right]$$

$$\beta_1^n = 2C_{44}^n \left[-\frac{3(C_{22}^n + C_{23}^n)}{C_{23}^n} A_1^n r^2 + \frac{3A_2^n}{r^4} - A_3^n \right]$$

$$\zeta_1^n = 2C_{44}^n \left[-\frac{C_{22}^n + C_{23}^n}{C_{22}^n} \frac{A_4^n}{r^2} - \frac{3A_2^n}{r^4} + A_3^n \right]$$

$$\gamma_1^n = C_{44}^n \left[-\frac{3(C_{22}^n + C_{23}^n)}{C_{23}^n} A_1^n r^2 - \frac{6A_2^n}{r^4} - 2A_3^n - \frac{(C_{23}^n + C_{22}^n)}{C_{22}^n} \frac{A_4^n}{r^2} \right]$$

$$\alpha_2^n = -2C_{12}^n C_{44}^n \left[\frac{3B_1^n r^2}{C_{23}^n} + \frac{B_4^n}{C_{22}^n r^2} \right]$$

$$\beta_2^n = 2C_{44}^n \left[-\frac{3(C_{22}^n + C_{23}^n)}{C_{23}^n} B_1^n r^2 + \frac{3B_2^n}{r^4} - B_3^n \right]$$

$$\zeta_2^n = 2C_{44}^n \left[-\frac{C_{22}^n + C_{23}^n}{C_{22}^n} \frac{B_4^n}{r^2} - \frac{3B_2^n}{r^4} + B_3^n \right] \qquad (11)$$

$$\gamma_2^n = C_{44}^n \left[\frac{3(C_{22}^n + C_{23}^n)}{C_{23}^n} B_1^n r^2 + \frac{6B_2^n}{r^4} + 2B_3^n + \frac{(C_{23}^n + C_{22}^n)}{C_{22}^n} \frac{B_4^n}{r^2} \right]$$

$$\alpha_3^n = C_{11}^n (D_3^n - e_z^n) + 2C_{12}^n (D_1^n - e_r^n)$$

$$\beta_3^n = C_{12}^n (D_3^n - e_z^n) + (C_{22}^n + C_{23}^n)(D_1^n - e_r^n) + (C_{12}^n - C_{23}^n) \frac{D_2^n}{r^2}$$

$$\zeta_3^n = C_{12}^n (D_3^n - e_z^n) + (C_{22}^n + C_{23}^n)(D_1^n - e_r^n) - (C_{12}^n - C_{23}^n) \frac{D_2^n}{r^2}$$

$$\delta_4^n = C_{55}^n \left[F_4^n - \frac{F_5^n}{r^2} + F_6^n \right]$$

$$\xi_4^n = C_{55}^n \left[F_3^n - \frac{F_5^n}{r^2} - F_6^n \right]$$

$$\delta_5^n = C_{55}^n \left[H_4^n - \frac{H_5^n}{r^2} + H_6^n \right]$$

$$\xi_4^n = C_{55}^n \left[H_3^n + \frac{H_5^n}{r^2} + F_6^n \right]$$

We evaluate the constants in Equation 9 and Equation 11 by:

1. imposing the boundary conditions stated in Equation 1.

2. requiring the tractions and displacements to be continuous at the constituent interfaces

$$u_i^n = u_i^{n+1} \ , \ \sigma_{ir}^n = \sigma_{ir}^{n+1} \tag{12}$$

3. demanding that the displacements and stresses be bounded as r approaches zero, so that

$$\begin{aligned} A_2^1 = A_4^1 = 0 \ , \ B_2^1 = B_4^1 = 0 \\ D_2^1 = 0 \ , \ F_5^1 = 0 \ , \ H_5^1 = 0 \end{aligned} \tag{13}$$

The composite element stress can be determined by volume averaging the stress field over the constituents. The stress-strain relation for the composite element now takes the form

$$\overline{\sigma_{ij}} = \overline{C_{ijkl}}(\overline{\varepsilon_{kl}} - \overline{e_{kl}}) \tag{14}$$

To calculate the effective stiffness properties for the composite element, we first set the expansional strain components identically equal to zero, i.e.

$$e_z^n = 0 \ , \ e_r^n = 0, \quad (for\ n = 1, 2, \ldots N) \tag{15}$$

The stress-strain relation for the composite reduces to (in contracted notation)

$$\overline{\sigma_i} = \overline{C_{ij}}\ \overline{\varepsilon_j}, \quad (i, j = 1, 2, \ldots 6) \tag{16}$$

By setting the *j-th* strain component equal to unity, while all others are zero, we obtain the *j-th* column of the stiffness matrix. The composite engineering constants may then be defined in terms of the elastic compliances, S_{ij}.

To evaluate the effective expansional properties of the composite element, we set the mechanical strain components identically equal to zero. If the e_{kl}^{n} (the local material expansional strains) are given their actual values according to some external stimulus (such as a temperature change), Equation 14 yields

$$\overline{e_{ij}} = - \overline{S_{ijkl}}\ \overline{\sigma_{kl}} \qquad (17)$$

where the compliances have already been determined and the average stresses may be determined by volume averaging the stresses in the composite element.

3.0 FIBER FRACTURE IN UNIDIRECTIONAL COMPOSITES

The importance of micro-parameters (such as the interphase) on the performance of composite materials is only now beginning to be fully appreciated in the scientific community. Experimental work such as that of Madhukar and Drzal [2-4] and Schwartz and Hartness [24] have led researchers to seek to develop accurate micromechanical representations of the stress state in composite materials subjected to various loading configurations. Until recently, validation of these models has been accomplished only by volume-averaging techniques. Verification of the models with such methods leads to a "smearing out" of important details and in questionable validation.

In this chapter, an analytical model is developed which provides an approximate stress state in the region surrounding a fiber fracture in a unidirectional composite material. Using a linear superposition technique in conjunction with a fiber discount analysis, it is possible to determine the stress state in the neighborhood of multiple fiber fractures. This stress state may then be used in strength prediction models such as that described by Batdorf [17] to arrive at the desired macro-level strength predictions. In addition, the theoretical predictions for the stress field in the vicinity of fiber fractures are compared with direct experimental results. Not only can this experimental technique be used to validate the present model, it may be used to validate future models.

3.1 Single Fiber Fracture

To analyze a single fiber fracture in a unidirectional composite, we separate the problem into a near-field analysis and a far-field analysis. The total solution is then just the superposition of the

far-field solution and the near-field solution. For example, the stresses in a constituent material may be given by

$$\sigma_{ij}^{n} = \hat{\sigma}_{ij}^{n} + \tilde{\sigma}_{ij}^{n} \tag{18}$$

where the near-field stresses are denoted by hats and the far-field stresses by tildes, and $n = 1, 2, \ldots N$, where N is the number of constituent materials. The far-field solution for the case of uniform loading on the boundary may be obtained by the method detailed in the previous chapter. To determine the near-field solution, we use the method developed by Carman et al. [14].

In posing the near-field problem, we assume a fiber fracture has occurred in a composite with a hexagonal array of fibers, as shown in Figure 2. The size of the crack is denoted by r_c, the size of the fiber by r_f, and the distance to the nearest adjacent fiber by r_a. Prior to the formation of the crack, load was carried by this region. Following crack formation, however, the crack surface is traction-free. To impose this condition on the crack face, we apply a compressive force P_0 which is given by

$$P_0 = \int_0^{2\pi} \int_0^{r_f} \tilde{\sigma}_{zz}^{f} r\,dr\,d\theta + \int_0^{2\pi} \int_{r_f}^{r_c} \tilde{\sigma}_{zz}^{m} r\,dr\,d\theta \tag{19}$$

Note that the far-field stresses are used in this calculation.

If the assumption is made that the transverse strains do not significantly affect the axial stresses, P_0 may be closely approximately by

$$P_0 = C_{11}^f \tilde{\varepsilon}_{zz} \pi r_f^2 Z + C_{11}^m \tilde{\varepsilon}_{zz} \pi (r_c^2 - r_f^2) \tag{20}$$

If the crack does not extend into the matrix, then the second term in Equation 20 is identically equal to zero. If an interphase region is present, it may be accounted for by the inclusion of the appropriate integral expression in Equation 19.

Following Carman et al. [14], we make the assumption that the fibers immediately adjacent to the fractured fiber may be represented by an annular ring of material (see Figure 2). This assumption reduces the near-field problem to an axisymmetric one. While the point-wise stresses determined in such a manner are not the exact solution to the near-field problem they do accurately depict the trends in the stress variations of interest. The inner radius of the fiber annular ring, r_a, is given by the distance to the adjacent fibers. The outer radius of the fiber annular ring is chosen such that the area of the ring is equal to the area of the adjacent fibers. The outer radius of the matrix annular ring, r_4, is determined from the global fiber volume fraction. For hexagonal packing

$$r_o = \sqrt{6 r_f^2 + r_a^2}$$
$$r_4 = \frac{7 r_f^2}{v_f} \tag{21}$$

At this point, we construct a free-body diagram of the composite in the plane of the fractured fiber (see Figure 3). Since the forces generated by the near-field solution must sum to zero

$$P_0 - F_1 - F_2 - F_3 = 0 \tag{22}$$

where the F_n are given by

$$F_n = \int_0^{2\pi} \int_{r_{inner}}^{r_{outer}} \hat{\sigma}_{zz}^n r\,dr\,d\theta \tag{23}$$

To evaluate the stresses in Equation 23, Carman et al. [14] propose that the radial variation in axial strains in the region $r > r_c$ may be represented as

$$\hat{\varepsilon}_{zz}^n = Br^{-\frac{3}{2}} f(z) \tag{24}$$

where B is a constant yet to be determined and $f(z)$ represents the decay of the strains in the axial direction. For convenience, we impose the constraint that $f(0) = 1$. With this constraint, and the assumption that the axial stresses in each constituent are dominated by the axial strains, the near-field stresses in each constituent in the plane of the crack may be given by

$$\hat{\sigma}_{zz}^n(r,\ z=0) \approx C_{11}^n Br^{-\frac{3}{2}} \tag{25}$$

Combining Equations 22, 23, and 25 it is possible to solve for the unknown constant B:

$$B = \frac{P_0}{4\pi}\left[C_{11}^f\left(r_o^{\frac{1}{2}} - r_a^{\frac{1}{2}}\right) + C_{11}^m\left(r_a^{\frac{1}{2}} - r_c^{\frac{1}{2}} + r_4^{\frac{1}{2}} - r_0^{\frac{1}{2}}\right)\right]^{-1} \tag{26}$$

Once the constant B has been determined, the radial variation in the near-field axial strain (and thus in the near-field axial stress), is known. All that remains is to determine the axial variation of the near-field solution. To do so, we consider three separate approaches to this problem.

First we consider the classical shear lag theory [11]. The assumptions made in the development of this model are: the fibers support only tensile loading, the matrix supports and transfers only

shear loading, and shear transfer between the fibers is assumed to occur only in the matrix region between the fibers. Using equilibrium arguments and constitutive relations, the function $f(z)$ in Equation 24 may be written as

$$f(z) = e^{-\eta z} \tag{27}$$

where

$$\eta = \frac{1}{r_f}\left[\frac{1}{2}\frac{1-\sqrt{v_f}}{\sqrt{v_f}}\frac{E_f}{G_m}\right]^{-\frac{1}{2}} \tag{28}$$

and E_f is the fiber elastic modulus and G_m is the matrix shear modulus [7].

Another approach to this problem has been given by Carman et al. [14] They suggest that the fractured fiber-matrix element embedded in a composite may by represented as a fractured fiber embedded in an infinite matrix. An approximate solution to this problem has been developed by Whitney and Drzal [12]. Based on their results, Carman et al. propose that the axial variation in the near-field strain may be given by

$$\hat{\varepsilon}^{n}_{zz} = Br^{-\frac{3}{2}}(1+\lambda z)e^{-\lambda z} \tag{29}$$

where

$$\lambda = \frac{2}{r_c}\sqrt{\frac{C_{55}^{comp}S_{11}^{fm}}{1+4S_{12}^{fm}C_{55}^{comp}}} \tag{30}$$

The shear stiffness of the composite is given by C_{55}^{comp} and the values S_{11}^{fm} and S_{12}^{fm} are effective compliances for the fractured fiber-matrix element. These mechanical properties may be determined by the method detailed in Chapter 1. Fajardo [15] has shown that this is a better

representation of the axial decay than shear lag. However, the resulting rate of decay is still an inadequate representation of the experimental results. To address this problem, we seek an approximate solution by using the radial decay from the model of Carman et al. [14] First, we assume that the z displacement, u_z, may be represented in the form

$$u_z = R(r)\,Z(z) \tag{31}$$

If we assume that the gradients of the displacements u_r and u_θ are small in comparison to the gradients of u_z, then the third equilibrium equation becomes

$$C_{11}Z'' + C_{55}ZR'' + \frac{1}{r}C_{55}ZR'' = 0 \tag{32}$$

where C_{11} and C_{55} are the effective composite properties. Using the radial decay in strains proposed by Carman et al., the boundary conditions are posed as

$$\begin{aligned}
&1.\quad \frac{\partial u}{\partial z}(r,\,0) = -\varepsilon^0_{zz} \qquad 0 \le r \le r_c \\
&\qquad\quad \frac{\partial u}{\partial z}(r,\,0) = Br^{-\frac{3}{2}} \qquad r_c \le r \le r_4 \\
&2.\quad \frac{\partial u}{\partial z}(r,\,\infty) = 0 \\
&3.\quad \frac{\partial u}{\partial r}(0,\,z) \qquad\qquad \textit{Bounded} \\
&4.\quad u\,(r_4,\,z) = 0
\end{aligned} \tag{33}$$

Employing the technique of separation of variables, it is possible to obtain a solution for R in the form of

$$R = C_1 Y_0(\lambda_n r) + C_2 J_0(\lambda_n r) \tag{34}$$

where Y_0 is the Weber function of order zero, and J_0 is the Bessel function of order zero.

Imposing Boundary Condition 3, we obtain the result that $C_1 = 0$. Imposing Boundary Condition 4, we obtain the final form for the function R:

$$R = C_2 J_0(\lambda_n r) \tag{35}$$

where the λ_n satisfy the condition that

$$J_0(\lambda_n r_4) = 0 \tag{36}$$

With these λ_n known, it is possible to express the function Z in the form

$$Z = e^{-\left(\lambda_n z \sqrt{\frac{C_{55}}{C_{11}}}\right)} \tag{37}$$

As a result, we may express the displacement u_z as

$$u_z = \sum_{n=1}^{\infty} C_n J_0(\lambda_n r)\, e^{-\left(\lambda_n z \sqrt{\frac{C_{55}}{C_{11}}}\right)} \tag{38}$$

and the resulting near-field strains as

$$\hat{\varepsilon}_{zz} = \sum_{n=1}^{\infty} -\lambda_n C_n \sqrt{\frac{C_{55}}{C_{11}}}\, J_0(\lambda_n r)\, e^{-\left(\lambda_n z \sqrt{\frac{C_{55}}{C_{11}}}\right)} \tag{39}$$

Using the orthogonality condition for the function J_0 and Boundary Condition (1) we may calculate the constants, C_n as

$$C_n = -\frac{1}{\lambda_n}\sqrt{\frac{C_{11}}{C_{55}}}\;\frac{-\varepsilon^0_{zz}\int_0^{r_c} r J_0(\lambda_n r)\,dr + B\int_{r_c}^{r_4} r^{-\frac{1}{2}} J_0(\lambda_n r)\,dr}{\int_0^{r_4} r\,[J_0(\lambda_n)]^2 dr} \tag{40}$$

Once the axial variation in the near field strains has been determined, it is possible to calculate

an *ineffective length*, δ (the distance over which stress is transferred back into a fractured fiber). After Rosen [11], the ratio of the stress in the fractured fiber at $z = \delta$ to the far-field fiber stress is defined as the efficiency parameter, ϕ

$$\phi = \frac{\sigma_f(\delta)}{\sigma_f(\infty)} \tag{41}$$

Although the methods for determining the axial variation of stress presented by Carman et al. [14] and using the series solution presented in this manuscript do not admit a closed-form expression for the ineffective length, the shear lag solution does. In terms of the efficiency parameter, ϕ, and the constant η given by Equation 28, the ineffective length, δ, may be given by

$$\delta = -2\frac{\ln(1-\phi)}{\eta} \tag{42}$$

3.2 Multiple Fiber Fracture

Using the results from the previous section, it is possible to determine the near-field stresses for multiple fiber fractures which occur in the same plane. To do so, we use a fiber-discount method proposed by Carman et al. [14].

First we consider two adjacent fibers which have fractured in the same plane as shown in Figure 4. The second fiber does not support any of the load due to the first broken fiber. Therefore, we do not include it in the analysis of the first fractured fiber (see Figure 4). This is equivalent to reducing the area of the fiber annular ring by the area of one fiber. As a result, the value of the outer radius of the fiber annular ring, r_o, for the case of hexagonal packing is given by

$$r_o = \sqrt{5r_r^2 + r_a^2} \tag{43}$$

Using the results from the previous section, we may determine the near-field stresses due to this fiber fracture. To determine the near-field stresses due to the second fiber fracture, we repeat the process employed for the first. The total near-field solution is then the superposition of the near-field solution for the first fiber fracture and the near-field solution for the second fiber fracture. We note that at this point the resulting stress field is no longer axisymmetric. An approach similar to this may be used to evaluate the stress concentrations due to more than two adjacent fiber fractures.

Once the near-field solution in the plane of the crack is known, it is necessary to evaluate the axial variation in the near field solution. Gao et al. [18] have presented a modified shear lag analysis which allows us to determine the ineffective length, δ, in terms of the stress concentration, c, and the efficiency parameter, ϕ:

$$\phi = \left[c+\frac{(1-c)}{\delta\eta}\right]\left[1-\exp(-\delta\eta)\right]-\frac{(1-c)}{\delta\eta}\left[(\delta\eta+1)\exp(-\delta\eta)-1\right] \quad (44)$$

In the case of the axial variation in stress proposed by Carman et al. [14], it is possible, once again, to use an equivalency argument. As the number of fiber fractures increases, the value of r_c should increase. To evaluate the rate of increase, we require that the area of a circle of radius r_c be equal to the area of the fractured fiber-matrix elements. The series solution is no longer applicable because the problem can no longer be reduced to an axisymmetric one.

3.3 Experimental Validation

To evaluate the validity of the model for determining stress concentrations in a composite material we utilize a macro-model composite. A complete description of such a model composite is given

in Carman [25]. Carman et al. [14] have shown that the present theory gives good agreement with experimental data for a the stress concentrations in the plane of a single fiber fracture in a unidirectional composite material. Fajardo [15] has studied the axial decay of the stress concentrations due to a single fiber fracture. Using the results from this study, it is possible to validate the model for ineffective length developed in Section 3.1. First we consider the results for a model composite with a local fiber volume fraction of 20%. The results from this study are given in Figure 5, along with the theoretical predictions from shear lag, the analysis of Carman et al. [14] given by Equation 29, and the results from the present analysis given by Equation 39. It is evident that the present analysis gives a much better representation of the experimental results than either of the previous theoretical predictions. Next we consider the results for a model composite with a local fiber volume fraction of 15%. These results are presented in Figure 6. Once again, we see that the present theory gives a much better representation of the experimental data than either of the two previous theories. At this point, however, it is important to point out that this analysis assumes that the near-field stresses in the plane of the crack may be approximated by the form of Equation 25.

Next we consider the case of two adjacent fiber fractures in a unidirectional model composite as depicted in Figure 7. Using the analytical model developed in the previous section, it is possible to determine the strain concentrations in the plane of the crack. If we take the origin of the r-z coordinate system to be located at the center of one of the fractured fibers, the near-field strains in the plane of the crack ($z = 0$) may be given by

$$\tilde{\varepsilon} = B\left[r^{-\frac{3}{2}} + (r + 3r_f)^{-\frac{3}{2}}\right] \qquad (45)$$

where B is given by Equation 26 and for this geometry

$$r_a = 2r_f$$
$$r_o = \sqrt{3r_f^2 + r_a^2} \qquad (46)$$

The material properties for this composite system are given in Table 1.

A comparison of the predicted strain concentrations and the experimentally measured values is given in Figure 9. The experimentally measured values were obtained by attaching strain gages to the structural fibers in the model composite. Since the strain gages average the strains experienced over their gage length, we would expect that the experimentally measured strains would be slightly lower than the point strains predicted by the analytical model. With the exception of the one data point at $r/r_f = 2$, we see that this is indeed the case. In addition to the fact that we have only an approximate solution to the problem at hand, the discrepancy here may be attributable to experimental error in determining the strains or to some other anomaly (such as porosity) present in the composite.

Finally, we consider the predictions for strain concentration given by Hedgepeth and Van Dyke [13] and Rosen's [11] shear lag analysis. In the shear lag analysis, the matrix is assumed to carry no normal load, and the load originally carried by the fractured fiber is distributed equally to the fibers adjacent to the fractured fibers. For two fiber fractures, this gives a strain concentration of 2.0 on the adjacent fiber and of zero in the matrix (a result of the assumption that the matrix supports no normal loading). Hedgepeth and Van Dyke's analysis predicts a strain concentration of 1.6. We see that the present model gives a more accurate representation of the trends in the strain concentration than either of the previously developed models.

3.4 Application to Composite Tensile Strength

One of the classical models of composite tensile strength is that developed by Batdorf [17]. Batdorf considers a composite containing N fibers, each of length L held together by a matrix. Damage in the composite due to loading is assumed to consist solely of breaks in the fibers. There will be single isolated breaks, designated *singlets*, pairs of breaks (*doublets*), as well as triplets or in general *i-plets*. Each *i-plet* is surrounded by n_i nearest neighbors, each of which is subjected to a maximum stress concentration of c_i in the plane of the break. This stress concentration extends over a length δ_i (exactly the *ineffective length*). We first assume that the fiber failure conforms to a two-parameter Weibull representation. Therefore, when a stress σ is applied to a fiber of length l, the probability of failure, P_f is given by

$$P_f(\sigma) = 1 - \exp\left[-\frac{l}{l_0}\left(\frac{\sigma}{\sigma_0}\right)^m\right] \tag{47}$$

where σ_0 is the Weibull characteristic value, m is the Weibull modulus, and l_0 is the reference length. For the case in which $P_f \ll 1$, this the probability of failure may then be approximated by

$$P_f \approx \frac{l}{l_0}\left(\frac{\sigma}{\sigma_0}\right)^m \tag{48}$$

The number of singlets may be determined by multiplying the probability of failure by the total number of fibers, N, so that

$$Q_1 = N P_f = N \frac{L}{l_0}\left(\frac{\sigma}{\sigma_0}\right)^m \tag{49}$$

We next assume that the stress concentration in the neighboring fibers varies linearly from c_1 to 1 over a distance $\delta_1/2$:

$$f(z) = c_1 + \frac{z}{\delta_1/2}(1 - c_1) \tag{50}$$

The reliability of a fiber having a stress variation of this type may be given by (see Reifsnider [23])

$$R = \exp\left[-\left(\frac{\sigma}{\sigma_{a0}}\right)^m \right] \tag{51}$$

where

$$\sigma_{a0} = \sigma_0 \left(\int_0^l [f(z)]^m \, dz \right)^{-\frac{1}{m}} \tag{52}$$

Using this relation, we can show that the probability of failure in the overstressed region may be approximated by

$$P_1 \approx \frac{\lambda_1}{l_0}\left(c_1 \frac{\sigma}{\sigma_0}\right)^m \tag{53}$$

where

$$\lambda_1 = \delta_1 \frac{c_1^{m+1} - 1}{c_1^m (c_1 - 1)(m + 1)} \tag{54}$$

Because there are n_1 nearest neighbors to each singlet, the probability that a singlet becomes a doublet is given by

$$P_{1\text{-}2} = n_1 \frac{\lambda_1}{l_0}\left(c_1 \frac{\sigma}{\sigma_0}\right)^m \tag{55}$$

The number of singlets, Q_1, is given by Equation 49. Therefore we can estimate the number of doublets by

$$Q_2 = Q_1 n_1 \frac{\lambda_1}{l_0}\left(c_1 \frac{\sigma}{\sigma_0}\right)^m \tag{56}$$

In general, the number of *i-plets* may be approximated by

$$Q_{i+1} = Q_i n_i \frac{\lambda_i}{l_0}\left(c_i \frac{\sigma}{\sigma_0}\right)^m \tag{57}$$

or

$$Q_i = N\frac{L}{l_0}\left(\frac{\sigma}{\sigma_0}\right)^{mi} \prod_{j=1}^{i-1} c_j^m n_j \frac{\lambda_j}{l_0} \tag{58}$$

It can be seen that the slope of Equation 58 on a log-log plot is *im*. Figure 10 shows a representative schematic diagram of Equation 58 for several *i-plets* as a function of the applied stress level. The envelope of intersection points has a special significance. Over the stress range within which an *i-plet* lies on the envelope, it is unstable (that is as soon as it is created it will immediately become an $(i + 1)$-plet, which will immediately become an $(i + 2)$-*plet* until composite failure occurs). This failure stress is the lowest stress at which any unstable *i-plet* is present. This is the stress at which the envelope intersects the horizontal line $Q_i = 1$ (or $\ln Q_i = 0$).

Gao et al. [18] have conducted a detailed study of strength predictions in composites using the analysis of Batdorf presented above. In this study, however, they consider each of the neighbors of an *i-plet* to be subjected to the maximum stress concentration of that any of the neighbors experience. This does not seem appropriate, when we consider that only one or two neighboring fibers may experience this maximum stress concentration. In addition, as pointed out by Batdorf, higher order multiplets can have a number of different shapes each of which have different failure

stresses. Although the stress concentrations for each different shape may be determined using the analysis of Section 3.2, the failure probabilities would become much more complex. When a second order analysis is considered, these probabilities can be considered. Until then, however, we use a simple shear lag type approach in which the stress concentration, c_i, for an *i-plet* may be given by

$$c_i = \frac{X}{n_i} \tag{59}$$

where X = *number of broken fibers*. The ineffective length may then be determined by any of the methods detailed in Section 3.1. However, numerical studies as well as the results of Gao et al. [18] and Harlow and Phoenix [16] show that the strength values are not very sensitive to small changes in the ineffective length. As a result, we assume that the ineffective length for δ_1, δ_2, δ_3, ... may be given by the shear lag expression of Equation 42.

As an example of how we may obtain a strength estimate for a composite material, we consider the case of an AS-4/Epon 828 composite. We assume that the fibers are hexagonally packed in the composite, so that the values of n_i are as given in Table 2. We also assume that the material properties are as given in Table 3 and that the characteristic length of the weakest link, l_0, is 415 μm. The specimen dimensions are taken to be 127 mm X 12.7 mm X 2.54 mm. We may then estimate the number of fibers in the composite, N, by:

$$N = \frac{Cross\ Sectional\ Area\ of\ the\ Composite}{Area\ of\ One\ Fiber} * v_f \tag{60}$$

where v_f is the fiber volume fraction of the composite. The predicted variation in composite strength, σ_c, normalized to the Weibull parameter σ_0 as a function of v_f is shown in Figure 11 for two different values of the Weibull shape parameter, m. The composite strength has been related

to the fiber stress at failure, σ_f, by:

$$\sigma_c = \frac{E_c}{E_f}\sigma_f \qquad (61)$$

As we can see, as fiber volume fraction increases, there is a corresponding increase in composite tensile strength. In addition, there appears to be very little change in predicted tensile strength with reasonable variations in m for this particular composite. Let us next look at the composite strength as a function of the ratio of material properties E_f/G_m as depicted in Figure 12. Since the stress concentrations used in the present analysis are not functions of E_f/G_m this variation in strength is caused solely by changes in ineffective length of the composite. As the ratio of E_f/G_m increases, the ineffective length increases (a greater distance for the matrix to transfer load back to a broken fiber is required), the probability of encompassing a flaw on an adjacent fiber severe enough to cause that fiber to fracture increases. Therefore, we would expect the composite strength to decrease as the value of E_f/G_m increases. This is exactly the result that we see in Figure 12.

3.5 Conclusions

In this chapter, an analysis has been presented for the stress concentrations surrounding a single fiber fracture in a unidirectional composite material. Using a series solution technique with effective composite properties, a theoretical prediction for composite ineffective length has been made. The accuracy of this prediction has been compared with predictions made by other models using experimental results from a macro-model composite. In addition, using a fiber discount methodology, the stress concentration results for a single fiber fracture have been extended to include multiple fiber fractures. As more information on ineffective length as function of the

number of fiber fractures becomes available, these stress concentrations may be included in tensile strength predictions. Numerical results have been presented for tensile strength predictions of composites using a shear-lag analysis in conjunction with a statistical analysis.

4.0 OPTIMIZATION OF TRANSVERSE STRAIN TO FAILURE

One failure mechanism in composite materials that is of particular interest is the development of matrix cracks in composite laminae subjected to transverse loading. In almost every continuous fiber reinforced composite, these cracks initiate at or near the interface between the fiber and the matrix due to stress concentrations that are a result of the mismatch in stiffness properties. If these stress concentrations are reduced (or perhaps even eliminated), then the transverse strain to failure may be increased.

4.1 Analysis

The method that we employ to reduce these stress concentrations is to apply a finite thickness coating to the fibers before embedding them in a composite material. By choosing the properties of this coating, or *interphase*, properly we may reduce the resulting stress concentrations. Carman et al. [9] have suggested a hypothetical argument for the choice of these properties. Consider a representative volume element of a composite consisting of three concentric cylinders. These cylinders represent the fiber, the interphase, and the matrix. Using the analysis presented in the first section, we may calculate the effective stiffness properties of a composite which consists of only the fiber and the interphase region. We may then replace the inner two cylinders by a single cylinder whose stiffness properties are identical to the effective stiffness properties of the fiber-interphase element. Now let us consider varying the stiffness properties of this fiber-interphase element.

First we consider an extremely stiff fiber-interphase element. This problem is analogous to a rigid

inclusion embedded in a homogenous material. If the representative volume element is subjected to transverse loading, the largest stresses occur at the interface between the fiber-interphase element and the matrix element at $\theta = 0°$ (see Figure 13). The maximum principal stress at this location corresponds to $\sigma_{rr}^{m}(z, r_i, 0°) = \sigma_{xx}^{m}(z, r_i, 0°)$. where r_i is the radius of the fiber-interphase element. It is reasonable to expect failure to initiate in this region of stress concentration.

Next we consider an extremely compliant fiber-interphase element. In this case, the problem is analogous to a hole in a plate problem. The stresses $\sigma_{rr}^{m}(z, r_i, 0°)$ are almost negligible in this case as shown in Figure 14 (in the limiting case of a hole they are zero). The largest stress for this case is $\sigma_{\theta\theta}^{m}(z, r_i, 90°) = \sigma_{xx}^{m}(z, r_i, 90°)$. We would therefore expect the hoop stresses at 90° to initiate failure in this case.

Now let us vary the stiffness of the fiber-interphase element from very stiff to compliant. As we do this, the maximum stress changes from the radial stress at $\theta = 0°$ to the hoop stresses at $\theta = 90°$. It is reasonable to expect that there is a stiffness value somewhere between these two extremes which balances these competing physical effects. As a result, Carman et al. [9] have proposed the following relation as the appropriate criterion for choosing the optimum interphase modulus:

$$\sigma_{rr}^{m}(z, r_i, 0°) = \sigma_{\theta\theta}^{m}(z, r_i, 90°) \tag{62}$$

Using the model developed in Section 2.0, it is possible to calculate the stresses in the representative volume element. If we consider the optimum Young's modulus of the interphase

to be unknown, the stress equations in conjunction with Equation 62 represent a system of 19 equations and 19 unknowns. These resulting equations, however, are nonlinear with respect to the unknown Young's modulus of the interphase. Therefore to complete the analysis, we solve Equation 62 and Equation 11 numerically using a secant method.

4.2 Numerical Results

To study the effect of the interphase properties on the stress state in a composite material, we consider the case of a coated AS-4 fiber embedded in an Epon 828 matrix. The material properties for the fiber and the matrix are given in Table 3. The fiber volume fraction is 0.59 and the interphase volume fraction is 0.13. To determine the appropriate boundary conditions to apply to the Representative Volume Element (RVE), we consider the case of a cross ply laminate. When this laminate is subjected to tensile loading, the 90° plies are in transverse tension. If there are a sufficient number of 0° plies present, the transverse strain in the 90° plies will not be significantly effected by hypothetical changes in the mechanical properties of the interphase. Therefore, in this study, we consider the RVE to be subjected to boundary conditions of the form

$$\varepsilon^0_{xx} = C, \quad \varepsilon^0_{yy} = \frac{S^c_{23}}{S^c_{22}} C, \quad \varepsilon^0_{zz} = \frac{S^c_{12}}{S^c_{22}} C \tag{63}$$

where C is a constant strain.

We now investigate the location of maximum stress values in a composite which contains no fiber coating (termed *no interphase*), in a composite which contains fibers coated with an interphase which has a Young's modulus determined by the method described above (termed *optimum interphase*), and in a composite which has a fiber coating of modulus 0.01 times that of the matrix

(termed *compliant interphase*). This optimum interphase modulus is calculated to be 0.335 Ga. Carman et al. [9] have shown that the maximum stresses in the matrix occur at $r = r_i$ (at the boundary between the interphase and the matrix). For this reason, we will limit our discussion to the circumferential variation in the stresses at this location.

The normalized maximum principal stresses, σ_{11}, for the no interphase, the compliant interphase, and the optimum interphase system is shown in Figure 16, where the angle θ is measured with respect to the loading direction. These principal stresses have been normalized to the stress in a pure matrix material subjected to the boundary conditions given by Equation 63. In this way, we are able to see the stress concentration effects of the fibers. For the case of the no interphase system ($E_f/E_m = 1$), the maximum stress concentration of 3.18 occurs at $\theta = 0°$. In the case of the compliant interphase system ($E_f/E_m = 0.01$), the maximum stress concentration of 1.53 occurs at $\theta = 90°$. For the case of the optimum interphase system ($E_f/E_m \approx 0.1$), the maximum stress concentration of 1.27 occurs at $\theta = 0°$ and $\theta = 90°$. Thus we see that the maximum stress concentration due to the uncoated fiber is 2.5 times greater than that due to a fiber coated with the optimum interphase.

4.3 Experimental Validation

4.3.1 Materials

To validate this analysis, we make use of a macro-model composite similar to that used in Section 3.3 to validate the stress concentration predictions. In this case, however, the specimen geometry simulates that of a transverse tensile specimen. The structural fibers used in the present study are 3 mm diameter borosilicate glass stirring rods and 3.125 mm diameter wooden dowel rods. These choices present us with the opportunity to vary the stiffness ratios between the fiber and the

matrix. By changing the fiber spacing, it is possible to vary the local fiber volume fraction. At the present time, we have the capability to study two fiber spacings. In the case of the glass/epoxy system these spacings correspond to fiber volume fractions of 0.44 and 0.25. The matrix material used in all tests is PLM-9 epoxy (manufactured by Micromeasurements). This material is a brittle thermosetting epoxy.

The specimen preparation is almost identical to that explained by Carman [25]. Prior to manufacturing the model composite, the mold is thoroughly cleaned with acetone and a release agent is applied. Any excess release agent is removed with a dry cloth to prevent outgassing. Following the mold preparation, it is necessary for us to make the choice of fiber type (either glass or wood) and of fiber spacing. Once the fibers have been selected, they are cleaned with acetone to remove any oils which may have been deposited on them during handling. If fiber coatings are desired, they are placed on the fibers at this time. In the present study we will consider only one fiber coating, vacuum grease, although we are not limited to this coating. The fibers are then placed in the appropriate locations and secured to the top and bottom of the mold. The mold is then placed in a programmable oven to preheat at 50°C for a period of 1 hour.

During this preheating period, the PLM-9 epoxy is prepared following the manufacture's instructions. Once the preparation of the epoxy is completed, the matrix material is poured slowly along the inside corner of the mold. This slow pouring serves to reduce the amount of porosity present in the composite after curing. Once the pouring process is complete, the mold is once again placed in a programmable oven at the desired cure temperature for the appropriate time period. This time and temperature are extremely crucial. If we cure the composite at an elevated temperature, large residual stresses are present in the fiber and matrix. To reduce these stresses,

a cure cycle of 37°C for a period of 24 hours is used in the present study. This cure cycle decreases the residual stresses and provides a significantly cured composite.

Once the composite is removed from the mold, it is cut into 25.4 mm wide specimens. Extensometer tabs are then placed on the specimen across a 25.4 mm gauge length. Special care is taken to ensure that the tabs are aligned parallel to the structural fibers.

4.3.2 Results and Discussion

All of the tests in this study were conducted using a 10 kN servo-hydraulic test machine operated in load control at an applied loading rate of 200 N per second. This rate of loading was chosen in an attempt to reduce any viscoelastic effects in the matrix. During the testing procedure, load and strain data were taken at a rate of 10 hertz per channel.

In the present study, we consider three material systems. The first material system chosen is a glass/epoxy composite. The fiber volume fraction is 0.44 and the interphase volume fraction is 0.03. The properties of the fiber and matrix are

$$E_{xx}^{f} = 62.7\ GPa,\ E_{zz}^{f} = 62.7\ GPa,\ \nu_{xz}^{f} = \nu_{xy}^{f} = 0.2,\ G_{xz}^{f} = 26.143\ GPa$$
$$E^{m} = 3.5\ GPa,\ \nu^{m} = 0.36$$

Based on these properties and the criterion presented in Equation 62, the optimum interphase modulus is calculated to be 0.113 Ga.

The second material system chosen is also a glass/epoxy composite. In this case, however, the fiber volume fraction is 0.25 and the interphase volume fraction is 0.017. Based on the properties of this system, the optimum interphase modulus is calculated to be 0.121 Ga.

The third material system we consider is that of a wood/epoxy composite. The fiber volume fraction is 0.48 and the interphase volume fraction is 0.03. The properties of the wood fibers are taken as

$$E_{zz}^{f} = 10\ GPa,\ E_{xx}^{f} = 10\ GPa,\ \nu_{xz}^{f} = 0.3,\ \nu_{xy}^{f} = 0.3,\ G_{xz}^{f} = 1.923\ GPa$$

while the properties of the matrix are the same as above. For this case the optimum interphase modulus is calculated to be 0.157 Ga.

We first investigate the effect of the interphase properties on the maximum principal stress in the matrix. For a brittle material, the maximum principal stress is an appropriate failure criterion. By minimizing such a stress, it should be possible to increase the strain to failure or strength of the composite. Three values are used for the interphase modulus. The first of these is equivalent to the modulus of the matrix. This corresponds to a composite in which no interphase region is present. The second modulus chosen corresponds to a case of no adhesion between the fiber and the matrix. To simulate such a case, the interphase modulus is taken to be 1 Pa (roughly nine orders of magnitude less than the matrix modulus). The final value is that of the optimum interphase.

The variation of maximum principal stress with orientation angle, θ, for the 0.44 fiber volume fraction glass/epoxy system is shown in Figure 17. For presentation purposes, the values are normalized to the stress in the pure epoxy subjected to the same strain state. In this way, the stress concentration due to the fibers may be observed. It is important to note at this time that this is not a stress concentration in the usual sense of the term (the ratio of the local stress to the applied far-field stress). For the case in which no interphase region is present, the stress concentration is 3.62 at $\theta = 0°$. The case of no adhesion gives a stress concentration of 1.74 at

$\theta = 90°$. The optimum interphase gives stress concentrations of 1.29 at both $\theta = 0°$ and $\theta = 90°$ (as is required by Equation 62).

Figure 18 shows similar results for the 0.25 fiber volume fraction glass/epoxy system. The case with no interphase region gives a stress concentration of 2.40 at $\theta = 0°$ and the case of no adhesion gives a stress concentration of 2.00 at $\theta = 90°$. The optimum interphase region gives stress concentrations of 1.31 at both $\theta = 0°$ and $\theta = 90°$.

Next we consider the 0.48 fiber volume fraction wood/epoxy system. The variation in principal stress with angle theta is shown in Figure 19. The case with no interphase region present gives a stress concentration of 1.98 at $\theta = 0°$ and the case of no adhesion gives a stress concentration of 1.67 at $\theta = 90°$. The optimum interphase region gives stress concentrations of 1.18 at both $\theta = 0°$ and $\theta = 90°$.

Table 4 summarizes the results from the model composite experimental tests. If we turn our attention to the strain to failure column, we can now evaluate the theoretical predictions given above. First we consider the ratio of the strain to failure of the 0.44 fiber volume fraction glass/epoxy system with a vacuum grease coating to that with no interphase. This ratio is 1411/595 ($\approx$2.37). As seen in Figure 17, the model predicts that the stress concentration for the no interphase system is 2.08 (3.62/1.74) times greater than that of the vacuum grease system. In addition, the model predicts that the maximum principal stress occurs at $\theta = 0°$ for the case of no interphase and at $\theta = 90°$ for the case of no adhesion. These are the locations at which failure was observed to occur in those systems (see Figure 20).

Next we consider the ratio of the strain to failure of the 0.25 fiber volume fraction glass/epoxy system with a vacuum grease to that with no interphase. This ratio is 1275/976 (≈1.31). As seen in Figure 18, the model predicts that the ratio of the stress concentrations for these systems is 1.20 (2.40/2.00). Once again, the failures were observed to occur at the predicted locations (at $\theta = 0°$ in the no interphase system and at $\theta = 90°$ in the vacuum grease system--see Figure 20).

We next consider the ratio of the strain to failure of the 0.48 fiber volume fraction wood/epoxy system with a vacuum grease coating to that with no interphase. This ratio is 1453/1188 (≈1.22). From Figure 19, we see that the model predicts that the stress concentration for the no interphase system is 1.19 (1.98/1.67) times as great as that for the vacuum grease system.

In addition, we can use these results to evaluate the model's sensitivity to fiber properties and fiber volume fraction. First we consider the ratio of the strain to failure of the 0.44 fiber volume fraction glass/epoxy system with no interphase to that of the 0.25 fiber volume fraction glass/epoxy system with no interphase. This ratio is 976/595 (≈1.64). The model predicts a ratio of stress concentrations of 1.51 (3.62/2.40). Next we consider the ratio of the strain to failure of the 0.48 volume fraction wood/epoxy system to that of the 0.44 volume fraction glass/epoxy system. This ratio is 1188/595 (≈2.00). The model predicts a ratio of stress concentrations of 1.83 (3.62/1.98). Thus we can see that the model accurately predicts trends in strain to failure with regard to fiber volume fraction, fiber stiffness, and interphase properties.

4.4 Conclusions

In this chapter, an analysis has been presented by which the transverse strain to failure of a composite can be maximized by the application of an appropriate fiber coating. Numerical results

have been presented for the case of an AS-4/Epon 828 composite. By selecting the appropriate fiber coating, it is possible to reduce the stress concentrations due to the presence of the fibers by 2.5 times. If we use maximum principal stress as a failure criterion, this suggests that the transverse strain to failure of the composite may be increased by this amount. In addition, the stress state predictions given by the model have been compared to experimental results obtained from a macro-model composite. These results have been shown to be in excellent agreement.

5.0 OPTIMIZATION OF SHEAR STRAIN TO FAILURE

The use of composite materials has grown considerably over the past two decades in applications ranging from sporting goods to aerospace vehicles. Even though these materials are more widely used today, the specific physical mechanisms which govern their performance are not fully understood. To address this concern, scientists and engineers have begun to focus their attention on constituent interaction (i.e. fiber, interphase, and matrix) to gain a better understanding of these mechanisms. In fact, recent findings suggest that an opportunity exists to optimize the manufacturing process to maximize a materials performance [2 - 4].

Papers which review our current understanding of the interphase region between the fiber and matrix include Swain et al. [26]. Optimum interphase coatings for metal-matrix and polymeric-matrix composites subjected to thermal loading were studied by Ghosn and Lerch [7]. Carman et al. [9] presented an analysis to determine the optimal fiber coating for a composite subjected to transverse loading to minimize cross-ply cracking. Pak [27] published an analysis of a composite material subjected to shear traction to maximize the shear load supported by the fiber. At the macro-level, Madhukar and Drzal [2 - 4] published experimental results describing the significant effect of the interphase on macro-level strength and stiffness properties.

The purpose of this chapter is to investigate the influence of fiber coatings on the stress distribution in a continuous unidirectional composite subjected to axial shear loading. This analysis is fundamentally different from Pak's [27] analysis in that the stress in the composite is being minimized instead of the load in the fiber being maximized. These two solutions provide

distinctly different results for the optimal coating. The results demonstrate that by choosing a coating with the proposed methodology, the stress and energy state in the matrix is minimized.

5.1 Analysis

Consider a unidirectional composite material subjected to an axial shear strain. By prescribing the displacements along a representative volume element (see Figure 1) in the composite a solution can be generated for the local stress and strain variations in each constituent. Based on the assumption that the representative element experiences the same strain as the composite, the following boundary conditions are applied.

$$\begin{aligned} u_r^m &= u_\theta^m = 0 \\ u_z^m &= \gamma_{xz}^c \, r_m \cos\theta \end{aligned} \qquad (66)$$

In the above equation u is the displacement field, r_m is the radius of the matrix defining the boundary of the element (see Figure 1), γ_{xz}^c is the applied shear strain. Throughout the section, the superscripts *f*, *i*, and *m* refer to the fiber, the interphase, and the matrix, respectively. Equation 66 provides explicit information about the displacement variations which occur in the composite as a function of the θ and z variables. This equation, in addition to the equilibrium equations written in terms of the displacement variables, provide the essential information to generate a solution to the problem. The pertinent governing equation is

$$u_{z,rr} + \frac{1}{r} u_{z,r} + \frac{1}{r^2} u_{z,\theta\theta} = 0 \qquad (67)$$

We can easily solve this partial differential equation subjected to the boundary condition presented in Equation 66. The solution we obtain is

$$u_z^n(r, \theta, z) = \left[\frac{F_1^n}{r} + F_2^n r\right] \cos\theta \tag{68}$$

Employing the stain-displacement and stress-strain relations for a transversely isotropic material, the non-zero stresses are given by

$$\sigma_{rz}^n = C_{55}^n \left[-\frac{F_1^n}{r^2} + F_2^n\right] \cos\theta$$
$$\sigma_{\theta z}^n = C_{55}^n \left[-\frac{F_1^n}{r^2} - F_2^n\right] \sin\theta \tag{69}$$

where C_{55}^n is the axial shear modulus of the n-*th* phase, and F_i^n are constants. The constants in Equations 68 and 69 (F_i^n) can easily be evaluated by

A. applying the boundary conditions stated in Equation 66,

B. demanding continuity of the traction and displacements at each interface (i.e. τ_{rz}^n & u_z^n),

and

C. demanding that the stresses be bounded (i.e. $F_2^f=0$).

For a three-cylinder system representing the fiber, interphase, and matrix, the following system of linear equations is obtained:

$$
\begin{aligned}
\frac{F_1^m}{r_m^2} + F_2^m &= \gamma_{xz}^c \\
\frac{F_1^m}{r_i^2} + F_2^m - \frac{F_1^i}{r_i^2} - F_2^i &= 0 \\
\frac{F_1^i}{r_f^2} + F_2^i - F_2^f &= 0 \\
-C_{55}^m \frac{F_1^m}{r_i^2} + C_{55}^m F_2^m + C_{55}^i \frac{F_1^i}{r_i^2} - C_{55}^i F_2^i &= 0 \\
-C_{55}^i \frac{F_1^i}{r_f^2} + C_{55}^i F_2^i - C_{55}^f F_2^f &= 0
\end{aligned}
\tag{70}
$$

where r_f and r_i are the fiber and interphase radii respectively. The five unknown constants F_i^n can easily be determined by solving this system of linear equations. If we treat the interphase shear modulus C_{55}^i as an unknown, a total of 6 unknowns exist in the above system of equations and an additional equation is required to evaluate this parameter. The equation is given as

$$
\sigma_{rz}^m (r_i, 0°, z) = -\sigma_{\theta z}^m (r_i, 90°, z) \tag{71}
$$

The rational behind this additional equation is detailed at the end of this section. Equation 71 with Equations 70 represents a system of six equations with 6 unknowns. The system of equations can easily be reduced by noting that Equation 71 implies that $F_1^m=0$. Using this result in the 1st equation in Equations 70, one can easily show that $F_2^m=\gamma_{rz}^c$. This result suggests that the stress and the displacement fields in the matrix are identical to a homogeneous matrix material. With further manipulations of Equation 70, we can develop the following closed-form relationship for the optimum interphase shear modulus:

$$(C_{55}^{i})^{2}+\left[\frac{(-C_{55}^{m}+C_{55}^{f})\ (1+\frac{r_i^2}{r_f^2})}{(\frac{r_i^2}{r_f^2}-1)}\right]C_{55}^{i}-C_{55}^{f}C_{55}^{m}=0 \qquad (72)$$

We note that the optimum interphase is not a function of the matrix radius (i.e. fiber volume fraction) and is solely dependent upon mechanical properties of the constituents and the relative ratio of the interphase to fiber radii.

To understand the choice of Equation 71, one must first appreciate the context of what is meant by "optimum." From a materials perspective, an optimum interphase will minimize the stress state in the matrix, such that the strength or strain to failure of the composite is increased, or more appropriately, maximized. With this concept in mind, an explanation is provided for the physical existence of severe stress concentrations which occur in composite materials.

The easiest way to understand the presence of stress concentrations in a composite is to consider two extreme examples: a rigid inclusion and a hole. For simplicity, let us consider only a fiber-matrix element and disregard the presence of an interphase region. First, if a rigid inclusion is embedded in a composite which in turn is subjected to an axial shear in the *xy*-plane, large shearing stresses are generated along the fiber-matrix interface at $\theta=0°$. On the other hand, if the "inclusion" is a hole, large shearing stresses are generated along the fiber-matrix interface at $\theta=90°$. However, if the inclusion described in the preceding two examples had the same elastic properties as the surrounding matrix no stress concentration would exist in the medium. The stress state in the matrix would be the same as a homogenous medium. It is on this basis that we suggest the existence of an optimum interphase.

Next, consider a fiber-interphase-matrix element existing in a composite material. If we chose an interphase material such that the effective mechanical properties of the fiber-interphase element are identical (or nearly identical) to those of the matrix, the deformation of this element would be similar to the surrounding matrix. This suggests that the interphase capable of achieving this goal will minimize the stress state.

While the fundamental approach described above gives a general understanding of the problem a more precise formulation is necessary. As stated above there are two competing physical mechanisms, a hole and a rigid inclusion, driving the stress concentrations in the composite. The maximum stress concentration for the two physical mechanisms are located at different positions in the composite (θ=0° and 90°). By constraining these off-setting quantities to be equivalent, the stress state will be "minimized" in this sense.

5.2 Results and Discussions

To determine if the aforementioned methodology actually minimizes the stress state in a composite, several AS-4/Epon 828 composites each with a different fiber coating are analyzed. The fiber volume fraction for each composite studied is v_f=0.59, the interphase volume fraction is v_i=0.13, the pertinent fiber property is C_{55}^f=28 Ga, and the pertinent isotropic matrix property is C_{55}^m= 1.1 Ga. Using these physical quantities in the analysis described in the preceding section, an optimum interphase shear modulus of C^i_{55}=0.11 Ga is calculated.

In discussing the results, it is more convenient to define a normalized shear modulus referred to the matrix value. Therefore, the primed shear modulus $C'^i_{55}=C^i_{55}/C^m_{55}$ represents a normalized value and for the optimum interphase C'^i_{55}=0.1. A total of four different interphase shear modulus

values will be studied in this discussion, that is a normalized shear modulus of C'^{i}_{55} =1e-7, 0.1, 1.0, and 5.1. These values range from an extremely compliant interphase value (i.e. actually a hole) to the geometric mean of the fiber and matrix shear moduli. This geometric mean was published as being an optimum interphase by Pak [27] for optical fibers.

In the present studies, a constant shear strain is applied to each composite element containing the different interphase materials. We note that this is not identical to applying the same shear stress to each element (see Carman et al. [9]). The stress quantities and the strain energy density values presented in this chapter are normalized to a homogeneous matrix material subjected to a similar strain

$$\sigma' = \frac{\sigma^{n}_{ij}}{\bar{\sigma}} \quad where \ \bar{\sigma} = C^{m}_{55}\gamma^{c}_{xz} \qquad (73)$$
$$U' = \frac{U}{\bar{U}} \quad where \ \bar{U} = \frac{1}{2}\bar{\sigma}\gamma^{c}_{xz}$$

where U is defined to be strain energy density.

The shear stress variations in the composite as a function of the normalized radial coordinate (r/r_m) for $\theta = 0°$ is shown in Figure 21. As the shear modulus of the interphase increases, the stress concentration in each of the constituents increases. This should be expected, since the shear stress concentrations at $\theta = 0°$ are due to rigid inclusions. The optimum interphase C'^{i}_{55}=0.1, while not apparently minimizing the stress at this specific location, does provide a stress distribution similar to a homogeneous matrix material (i.e. σ'_{rz}=1).

When reviewing the stress variations as a function of the normalized radial coordinate for $\theta = 90°$, as shown in Figure 22, we see a distinctly different trend in the matrix. While the stress

variations in the fiber and the interphase regions are similar to those in Figure 21, the ordering of the stress concentrations in the matrix are dissimilar. As the shear modulus of the matrix increases the stress concentrations decrease. This phenomena is attributed to the hole problem and is the opposite trend to that noted for Figure 21.

To provide a more complete picture of the shear stress concentrations that occur in the four material systems, a plot of the shearing stresses at the matrix/interphase interface as a function of θ is shown in Figure 23. This radial location is chosen consistent with the results presented in Figures 21 and 22, that is, relatively larger stress concentrations exist in this region, at least for the optimum value which this investigation deals with. As shown in Figure 23, the shearing stresses are minimized in the composite containing the optimum interphase. For stiff interphase values large shearing stresses occur at $\theta = 0°$ while for compliant interphases they occur at $\theta = 90°$. On the other hand the optimum composite has virtually no stress concentration (i.e. values of 1), and has no dependence on the angular position. This is typical of a homogeneous material systems subjected to axial shear.

Failure criteria are typically based on maximum shear (shown to be minimized in the preceding section), maximum principal stress or strain energy. The variation of the normalized maximum principal stress σ'_{11} in the matrix material at $r = r_i$ is depicted in Figure 24. The optimum interphase value minimizes this quantity also. The variation of the normalized strain energy density in the matrix is presented in Figure 25. Here, once again, the optimum interphase value minimizes the strain energy density in the matrix material. As stated previously, stiffer interphases have large excursions at $\theta = 0°$ while compliant interphases have excursions at $\theta = 90°$. The stress variation in the optimum composite as a function of θ is the same as expected for a

homogenous material system, that is no variation in θ, while the other material systems are typical of inhomogeneous systems.

The results presented in this section demonstrate that an optimum interphase applied to the fibers will minimize the stress state in a composite subjected to axial shear. The modulus of this material is smaller than the matrix material and is typical of rubbery materials. Rubbery materials are normally thought to be capable of large elongations prior to failure. The results presented in this section are also in agreement with the results published by Carman et al. [3] for minimizing the stress state in a composite subjected to transverse strains. That is, the modulus values for minimizing either stress state is similar. Therefore it may be advantageous to investigate the possibility of coating structural fibers with elastomers in more detail.

By applying optimum fiber coatings, the shear strength of the composite can theoretically be increased as much as fifteen times if an energy criteria is utilized to predict failure (see Figure 24). However, application of this coating results in a predicted composite shear modulus three times smaller than an AS4-Epon 828 composite without a fiber coating. This may affect the composite's compression strength which raises serious concerns about its applicability. This topic needs further attention to quantify these theoretical results as well as determine if any deleterious effects arise in other mechanical properties.

5.3 Conclusions

A methodology was presented to optimize a composite performance by coating the structural fibers. This technique resulted in a composite which responded to an axial shear load similar to a homogenous material as opposed to inhomogeneous. Theoretical results generated for an

AS-4/Epon 828 composite material shows that the maximum shear stress, maximum principal stress, and strain energy density is minimized in the matrix. These results suggested that the shear strain-to-failure of a composite can be increased as much as fifteen times with the appropriate coating. The optimum interphase value for this composite was suggested to be typical of natural rubber and is in agreement with the optimal results obtained for maximizing the transverse strength of a composite.

6.0 COMPRESSION STRENGTH OF COMPOSITES CONTAINING EMBEDDED SENSORS/ACTUATORS

The scientific and engineering communities have come to realize the potential benefits which can be derived from materials which contain integrated sensors and actuators. These benefits include health monitoring capabilities, in/post-flight inspections, active control, and noise suppression. Such material systems, which have been coined "smart" materials, offer a unique opportunity to explore a new scientific frontier and to significantly expand current operating envelopes of aircraft systems.

If sensor/actuators are embedded in a composite material, the most plausible shape to utilize is a cylindrical geometry (e.g. nitanol fibers and optical fibers). This geometry is most plausible because of its smooth, regular boundaries. The only corners or edges present in a structure containing such cylindrical geometry are at ingress or egress locations. If this is true, the pertinent question which plagues the engineering mechanics community is the development of an *appropriate embeddment procedure* which minimizes the adverse affect that these sensors and actuators will have on structural performance. Carman and Sendeckyj [28] have compiled a literature review of this topical area to aid researchers in their attempts to understand the effect of embedded sensors on performance issues. These individuals have identified *two fundamental static mechanical properties* which are adversely effected by the presence of a cylindrically shaped inclusion: *transverse tensile strength* and *axial compression strength.* While transverse strength has been analytically studied by Carman and Reifsnider [10] and has been experimentally investigated by Roberts and Davidson [19] as well as Carman et al. [20], compression strength has not been fully evaluated.

A few individuals have experimentally measured severe deteriorations in axial compression strength (up to 65%) [19, 29, 30]. On the other hand, some researchers have suggested a milder impact on compression strength 20-35% [31, 32], while one researcher has suggested no decrease whatsoever [33]. The scientific community qualitatively understands the parameters which cause the degradation in compression strength associated with embedded sensors/actuators. When an sensor/actuator is embedded between plies that are not aligned with the sensor/actuator, a local undulation exists in the composite plies. This local undulation results in compression strength degradation of the laminate. The fact that the stiffness of the plies, the ply layup, the diameter of the optical fiber, and manufacturing parameters play a role in determining the extent of this undulation and thus compression strength is signified by the analytical model developed by Dasgupta et al. [21].

In this chapter, we use a modified version of Dasgupta's model to obtain the local geometry of the plies around the embedded sensor or actuator. By using the predicted geometry in a revised micromechanical model of compression strength developed for composite materials, we can obtain predictions of this mechanical property for a variety of situations. The fundamental analysis provided herein can be employed by manufacturers of "smart" materials to gain insight into developing design limits for these material systems. This approach is much more cost efficient than the out-dated make-it-and-break-it mentality.

6.1 Geometry of the Undulation

To model the shape of the undulation due to an embedded sensor or actuator, we follow much of the analysis of Dasgupta et al. The potential energy of the entire structure is given by the difference between the strain energy, U, and the work, W, done by the applied loads, or:

$$\Pi = U - W \tag{74}$$

Dasgupta et al. assume that the axial stiffness of the reinforcing fibers, compressive transverse stiffness, and lamination pressure are the dominant parameters affecting the shape of the undulation. Higher order effects such as resin shrinkage and warpage and shear deformations are ignored. The present analysis differs from the one presented by Dasgupta et al. in that the stiffness of the surrounding *plies*, and not just the surrounding fibers, is considered. With these effects in mind, the strain energy, U, is assumed to be solely due to bending and compressive deformations:

$$U = U_b + U_c \tag{75}$$

The domain for the analysis is shown in Figure 26. The composite is symmetric about the midplane with the sensor or actuator embedded at the plane of symmetry. The embedded sensor/actuator is assumed to be perfectly rigid. Therefore the kinematic boundary conditions for the domain of interest are:

$$\begin{aligned} \frac{\partial v}{\partial x} &= 0 \ at \ (0, y) \\ v &= -r_0\left(1 - \frac{y}{h}\right) - \frac{h_c}{h} y \ at \ (0, y) \\ \frac{\partial v}{\partial x} &= 0 \ at \ (a, y) \\ v &= 0 \ at \ (a, 0) \end{aligned} \tag{76}$$

where v is the displacement of the plies in the y coordinate direction (this describes the shape of the undulation), a is the width of the effected region, r_0 is the radius of the embedded sensor/actuator, h is the half-thickness of the laminate, and h_c is the displacement of the laminate top surface ($y = h$) as the lamination pressure is applied during the curing process.

To complete the solution process, it is necessary to compute U_b and U_c. For elastic deformations, the strain energy, U, is given by

$$U = \int_V \frac{\sigma^2}{2E} dV \tag{77}$$

From elementary beam theory, the stress state for a beam subjected to pure bending is given by

$$\sigma_b = E_x \frac{\partial^2 v}{\partial x^2} y \tag{78}$$

Therefore

$$U_b = \frac{1}{2} \int_V E_x \left(\frac{\partial^2 v}{\partial x^2} \right)^2 y^2 dV \tag{79}$$

where E_x is the lamina stiffness in the direction perpendicular to the embedded sensor/actuator. This stiffness is dependent upon ply orientation and therefore may vary through the thickness of the laminate depending upon the stacking sequence.

We next evaluate U_c. For a laminate subjected to uniaxial through-the-thickness loading, the stress state is given by

$$\sigma_y = E_y \frac{\partial v}{\partial y} \tag{80}$$

where E_y is the through the thickness stiffness of the laminate. As a result, the strain energy due to transverse compression of the laminate is given by

$$U_c = \frac{1}{2} E_y \int_V \left(\frac{\partial v}{\partial y} \right)^2 dV \tag{81}$$

The work done by the lamination pressure, q, is computed by:

$$W = -q\int_S (v_{y=h})\, dA \tag{82}$$

At this point we can obtain an expression for the total potential energy of the composite by substituting Equations 75, 79, 81, and 82 into Equation 74. Such a substitution yields

$$\Pi = \frac{1}{2}\int_V E_x\left(\frac{\partial^2 v}{\partial x^2}\right)^2 y^2 dV + \frac{1}{2}E_y\int_V\left(\frac{\partial v}{\partial y}\right)^2 dV + q\int_S (v_{y=h})\, dA \tag{83}$$

An approximate displacement field is chosen which satisfies the kinematic boundary conditions given by Equation 76. The displacement field chosen is as follows:

$$v = -\frac{1}{2}r_0\left[1 + \cos\left(\frac{\pi x}{a}\right)\right]\left(1 - \frac{y}{h}\right) - \frac{h_c}{h}y \tag{84}$$

where a and h_c are unknown constants which govern the shape of the undulation. This displacement field is much simpler in form than the one presented by Dasgupta et al.

To evaluate the unknown constants a and h_c in the approximation function, we use the principle of minimum potential energy. If the system is in equilibrium, then the first variation of potential energy is stationary, i.e.

$$\delta\Pi = \frac{\partial\Pi}{\partial a}\delta a + \frac{\partial\Pi}{\partial h_c}\delta h_c = 0 \tag{85}$$

This must hold for arbitrary variations. Therefore, it follows that

$$\frac{\partial\Pi}{\partial a} = 0 \tag{86}$$

and

$$\frac{\partial \Pi}{\partial h_c} = 0 \tag{87}$$

Due to the simple nature of the displacement function chosen, it is possible to obtain closed-form expressions for a and h_c (in general, higher-order approximation functions do not permit such a closed-form solution for this problem). To do so, we first impose the condition given by Equation 86 on Equation 83. This yields

$$h_c = \frac{hq}{E_y} + \frac{r_0}{2} \tag{88}$$

By imposing the condition required by Equation 85, we obtain (for the case in which E_x does not vary with y)

$$a^4 = \frac{E_x r_0^2 \pi^4 h^4}{10E_y\left[3r_0^2 - 8r_0 h_c + 8h_c^2 - 16hh_c\frac{q}{E_y}\right]} \tag{89}$$

6.2 Compression Strength Evaluation

To evaluate the effect of the undulation on composite compression strength, we follow the model presented in Tsai and Hahn [32] with minor modifications. Consider a composite subjected to compression in the direction of the structural fibers as in Figure 27. The initial curvature, v_0, of the plies is assumed to be due to an embedded sensor/actuator and therefore has the same form as that given by Equation 84:

$$v_0 = \frac{1}{2} r_0\left[1 + \cos\left(\frac{\pi x}{l}\right)\right] \tag{90}$$

where l is the half-length of the undulation. When a compressive load is applied, the final deflection of the plies is assumed to be of the form:

$$v = f\left[1 + \cos\left(\frac{\pi x}{l}\right)\right] \tag{91}$$

where f is the amplitude of the final deflection.

We then take a representative volume element of length dx and cross-sectional area A as shown in Figure 28. From moment equilibrium, we obtain

$$\frac{dM}{dx} - V + \sigma A\frac{dv}{dx} = 0 \tag{92}$$

where M is the bending moment, V the shear, and σ the applied compressive stress. We next assume that the bending moment is born by the structural fibers alone, while the shear is the result of the overall shear deformation of the representative volume element. Therefore the moment and shear are given by

$$\begin{aligned} M &= E_{11}^{f} I_f \frac{d^2}{dx^2}(v - v_0) \\ V &= AG_{12}^{c}\frac{d}{dx}(v - v_0) \end{aligned} \tag{93}$$

where G_{12}^{c} is the in-plane shear modulus of the lamina, E_{11}^{f} and I_f are the stiffness and area moment of inertia respectively of the structural fiber. Substituting Equation 93 into Equation 92, we can solve for the compressive stress, σ

$$\sigma = \left[G_{12}^{c} + E_{11}^{f}\frac{I_f}{A}\left(\frac{\pi}{l}\right)^2\right]\left(1 - \frac{r_0}{2f}\right) \tag{94}$$

For circular fibers, $I_f/A = v_f r^2/4$. In composites with embedded sensors or actuators, r_f/l is much less than unity and therefore the second term in brackets may be neglected. As the applied stress, σ, increases, f increases according to Equation 93 until it reaches a critical value, f_c, at which the composite fails. The compressive strength is therefore given by

$$\sigma_c = G_{12}^c\left(1 - \frac{r_0}{2f_c}\right) \tag{95}$$

Following Tsai and Hahn, we realize there are two possible sources of composite failure: local shear failure and bending failure of the structural fibers. Local shear failure occurs when the maximum shear stress determined from Equation 93 reaches the shear strength, S, of the composite. The critical value f_c for local shear failure is therefore given by

$$f_c = \frac{l}{\pi}\frac{S}{G_{12}^c} + \frac{r_0}{2} \tag{96}$$

Next we consider bending failure of the structural fibers. This occurs when the maximum bending stress determined from Equation 93 reaches the fiber strength, X_f. The critical value of f_c for structural fiber bending failure is therefore given by

$$f_c = \frac{X_f}{E_{11}^f}\frac{l}{\pi}\frac{l}{r_f} + \frac{r_0}{2} \tag{97}$$

Since l/r_f is much larger than unity, Equation 97 suggests that f_c can become quite large before bending failure of the fibers occurs. As a result, the composite fails due to local shear failure and the critical value f_c is given by Equation 96. Substituting Equation 96 into Equation 95, we obtain the composite compression strength

$$\sigma_c = G_{12}^c\left(\frac{1}{1 + \frac{r_0\pi}{2l}\frac{G_{12}^c}{S}}\right) \tag{98}$$

For the special case in which no sensor or actuator is present, the term r_0/l is equal to zero, and the compression strength is predicted to be equal to the shear modulus, G_{12}^c. As pointed out by Tsai and Hahn, the compression strength is never this large (usually about one third). Other than the inherent initial curvature of the structural fibers, they suggest that this discrepancy may be due

to the nonlinear shear behavior of composites.

To evaluate the compression strength, it is necessary to relate the parameter l in Equation 98 to the parameter a given by Equation 91. The parameter l corresponds to the distance the undulation extends along the length of the composite fibers and a is the distance this region extends in a direction perpendicular to the embedded sensor or actuator. From geometry

$$l = \frac{a}{\sin \theta} \tag{99}$$

where θ is the angle between the embedded sensor/actuator and the reinforcing fibers (see Figure 26). As expected this length goes to infinity as θ approaches zero (the case in which the sensor/actuator is parallel to the composite fibers) and approaches a as θ goes to 90°.

6.3 Validation of the Model

To evaluate the model's ability to predict the geometry of the undulation, we consider a 145 micron diameter and a 185 micron diameter optical fiber embedded in a 28-ply unidirectional composite. The properties for this material system are given in Table 5. The 145 micron optical fiber was embedded at 45° with respect to the structural fibers and the 185 micron optical fiber was oriented at 90° with respect to the structural fibers. This gives us the opportunity to evaluate the model's sensitivity to the radius of the embedded sensor and to the orientation angle of the surrounding plies.

A comparison of the actual and computed geometry for the 90° sensor is given in Figure 29. We can see that the model gives a reasonably good approximation to the actual geometry, although the length of the undulation is, in reality, slightly larger than predicted. A similar observation may be made for the 45° sensor (Figure 30). The cut of the 45° sensor was made parallel to the

structural fibers, and therefore the apparent length of the undulation in Figure 30 is given by $2l$ (not $2a$). There are a number of competing effects which determine the geometry of the undulation for the 45° sensor in comparison to the 90° sensor. First of all, as the sensor diameter is decreased from 185 microns to 145 microns, the value of l/r_0 given by Equations 89 and 99 increases. In addition, as θ decreases from 90° to 45°, the value of l/r_0 given by Equation 99 increases (an increase in l/r_0 corresponds to an increase in compression strength as given by Equation 98). However, as θ decreases, the stiffness, E_x, in the direction perpendicular to the embedded sensor decreases as given by the fourth-order tensor transformation. This decrease in stiffness causes the value of l/r_0 to decrease. The net result of these competing mechanisms is that the value of l/r_0 increases for the 45° sensor. The consequences of these physical parameters on compression strength are discussed subsequently.

6.4 Application to Compression Strength

We next apply the model to the prediction of composite compression strength. For the composite described in the preceding section, the model predicts an a/r_0 value of 12.5 for the 90° sensor and an a/r_0 value of 9.27 for the 45° sensor. These values correspond to l/r_0 values of 12.5 and 13.1 respectively. Using these values in Equation 98, we predict that failure occurs at the 90° arm at an applied stress level of 743 MPa. The actual experimentally measured value reported by Lesko et al. [29] was 490 MPa. The result, however, was obtained using an unsupported gage length which should lower the measured compression strength.

To further evaluate the applicability of the model, we next consider the work of Roberts and Davidson [19] who embedded 93 micron diameter polyimide-coated fibers and 103 micron diameter acrylate-coated fibers in a T300/Hexcel F263 composite system. Using the material

properties published by the authors (Table 6), we obtain a predicted compression strength of 679 MPa for the 93 micron fiber. The reported measured value is 902 MPa (25% discrepancy). For the 103 micron fiber, we obtain a predicted compression strength of 618 MPa. The reported strength is 863 MPa (28% discrepancy). Although the absolute values of compression strength are incorrect, we see that the model correctly predicts the trend in the measured strength (the strength is inversely related to the size of the embedded sensor/actuator). In fact, the ratio of the predicted strengths for the two systems is 1.09, compared to an experimentally measured value of 1.04.

6.5 Parametric Studies

Finally we consider the effect of sensor/actuator diameter, laminate thickness, laminate stiffness, laminate shear strength, and sensor/actuator orientation angle on compression strength. To evaluate these effects we perform a number of parametric studies on compression strength of unidirectional composites with sensors/actuators embedded at an angle θ. The composite properties (except as otherwise noted) are given in Table 5.

In Figure 31, we study the variation in compression strength with sensor/actuator diameter and orientation angle. As expected the strength is a maximum at $\theta=0°$. The strength then decreases rapidly with orientation angle until θ is approximately equal to 20°. After this point, it is relatively constant. It is intuitive that strength should be maximum in the case when the sensor/actuator is aligned with the structural fibers (we should see no degradation in strength in this case) and a minimum in the case where the sensor/actuator is perpendicular to the structural fibers. However, the model suggests that a sensor/actuator aligned at 30° is just as severe. This result is of particular importance in the design of engineering structures containing embedded sensors and actuators. In these systems, it may not always be possible to orient the embedded

devices along the structural fibers, particularly at ingress or egress locations.

As depicted in Figure 31 the strength varies inversely with embedded sensor/actuator diameter, as we would expect (the smaller the sensor/actuator, the less severe the undulation). The minimum that occurs at θ approximately equal to 60° is most likely a result of the low-order approximation function chosen to represent the geometry. By using a higher-order approximation (such as that of Dasgupta et al.) for the geometry, this minor effect should be eliminated.

In Figure 32, we study the effect of laminate thickness on the compression strength. A similar trend with orientation angle is presented in this figure as that exhibited in Figure 31. We also see that the compression strength increases as the laminate increases. This trend makes sense intuitively if we consider extreme cases. Suppose we have a one laminate which is only two plies thick and another which is much thicker--for example 100 plies thick. If each of these laminates contains an embedded sensor/actuator of the same diameter, it seems reasonable to expect that the sensor/actuator would be less obtrusive in the thick laminate than in the thinner one. Such an intuitive conclusion is born out in Figure 32. However, by using the model, we are able to obtain a quantitative measure of the effects of laminate thickness on compression strength.

In Figure 33, we study the effect of laminate shear strength. We note that for values of shear strength representative of graphite/epoxy systems we see a less dramatic variation in compression strength than we did in the previous two figures (the compression strength is much more sensitive to sensor/actuator diameter and laminate thickness than it is on shear strength). However, as the shear strength of the laminate increases from 75 MPa to 100 MPa, there is a 35% increase in predicted compression strength. While this may appear to be a large increase in strength it corresponds to an increase from 23% to only 31% of the laminate compression strength without

an embedded sensor/actuator.

In Figure 34, we present the effect of structural fiber Young's modulus on the value of a/r_0. We choose not to study compression strength directly because of the complex interaction between stiffness and strength in composite materials. It is unreasonable to keep the shear modulus and shear strength of the composite constant while varying the Young's modulus of the structural fibers. Therefore we study the size of the undulated region as a function of structural fiber modulus of elasticity. To determine the ply stiffness, we use a modified rule of mixtures approach [35] and assume both the fiber and matrix to be isotropic. We see that as the fiber Young's modulus is increased, the value of a/r_0 increases. An increase in this value suggests an increase in compression strength if the shear strength and shear modulus were to remain constant. In actual composite systems, as the Young's modulus of the fibers increases, it is reasonable to expect the shear modulus (G_{12}^c) to increase as well. This would also lead to an increase in compression strength. The only remaining question is how the shear strength varies. At the present time, the relation between stiffness and strength is not fully understood, so no presentation of compression strength is given. Once a candidate material system is chosen, however, its shear strength and stiffness values are known quantities. It is then possible to determine the detrimental effect on compression strength of embedding actuators and sensors.

6.6 Conclusions

In this chapter, we have presented an approximate analytical model describing the geometry of the plies in the region near embedded sensors and actuators. By using a simple compression strength analysis in conjunction with the model of the geometry, we have obtained predictions for the compression strength of composite materials containing such embedded sensors. Although the absolute values of the predicted compression strength are off by approximately 25-30%, the model

has been demonstrated to accurately predict trends in compression strength. We have also conducted a number of parametric studies on compression strength of composites containing embedded sensors or actuators. These studies show that a sensor embedded at 30° is as obtrusive as one embedded at 90°. This analysis should provide starting points for the development of proper embeddment techniques associated with sensors and actuators. This work also provides a fundamental basis onto which higher order models for compression strength can be constructed.

7.0 CONCLUSIONS

Micromechanical models have been developed to represent fiber composite performance under a number of loading conditions. The first case considered was that of a unidirectional composite subjected to axial loading in the presence of a single fiber fracture. Using an existing analysis for the stress concentrations in the plane of the fractured fiber, it was possible to develop an approximate series solution to the ineffective length problem. A macro-model composite was then used to directly validate this analysis. The experimental results from this macro-model suggest that the series solution developed in this thesis gives a better representation of the axial decay of the stresses in the vicinity of a fractured fiber than either shear lag or the annular ring model presented by Carman et al. [14]. However, when compared to the experimental results, all of these micromechanical models overestimate the ineffective length.

The next case of loading considered was that of a unidirectional composite subjected to axial loading in the presence of multiple fiber fractures. To evaluate the stress state in such a case, a fiber discount methodology was used. This fiber discount methodology involves analyzing each of the fractured fibers separately. In each separate case, the adjacent broken fibers are discounted from the analysis since they no longer can support load. The total stress state is then simply the linear superposition of each of the individual cases analyzed. Once again, the predictions from this analysis were validated by use of the macro-model composite. In this case, the stress concentrations in the plane of two adjacent fractured fibers were measured. These experimental results suggest that the present model gives a better representation of the stress concentrations due to multiple fiber fractures than the shear lag analysis or the influence function approach presented by Hedgepeth and Van Dyke [13].

Once the ineffective lengths and stress concentrations due to multiple fiber fractures is known, it is possible to use a statistical analysis such as that presented by Batdorf [17] to arrive at macro-level tensile strength predictions. In this thesis, two parametric studies are conducted to determine the influence of fiber volume fraction and fiber-matrix properties on composite tensile strength. To perform these studies a number of simplifying assumptions were made. First of all, it was assumed that the load that was originally carried by the broken fibers was transferred equally to the neighboring unbroken fibers. Also, it was assumed that the ineffective lengths could be adequately represented by a shear lag analysis. These assumptions simplify the mathematics of Batdorf's analysis and make it possible to easily obtain tensile strength predictions. As more detailed (and accurate) depictions of the stress concentrations and ineffective lengths (as well as details concerning local inelastic effects) become available, the tensile strength predictions may be made more accurate.

The next case of loading considered was that of a unidirectional composite subjected to transverse loading. By applying a fiber coating of the appropriate modulus, it was shown that the stress concentrations in the surrounding matrix material could be minimized. A criterion was presented by which the modulus of this coating could be determined. To validate this analysis, once again a macro-model composite was used. Six different material systems were studied. In each case, the experimentally determined strain-to-failures were shown to be in excellent agreement with the theoretical analysis. In addition, the location of the failures in the test specimens was shown to be consistent with the predictions made by the analysis.

The next case considered was that of a unidirectional composite subjected to longitudinal shear loading. An analysis similar to that used for the transverse loading case was used to determine the appropriate fiber coating modulus to minimize the stress concentrations in the matrix. The

stress state in the matrix was shown to be identical to that of an isotropic material subjected to shear loading. For a typical graphite-epoxy composite (AS-4/Epon 828), this modulus was shown to be almost identical to that which minimized the stress concentrations due to transverse loading. This modulus was typical of elastomeric materials. However, the predicted shear modulus of the composite containing this coating was three times less than that predicted for the composite containing no coating. This reduction in shear modulus could have serious detrimental effects on the composite's compression strength.

The final case studied was compressive loading of a composite containing an embedded sensor or actuator. A linear-elastic analysis was developed to model the geometry of the composite plies in the vicinity of the embedded sensor or actuator. By using this model in a modified micromechanical model of compression strength, it was possible to make predictions of this mechanical property. The computed geometries and compression strengths were compared with values obtained from actual smart material systems. Also, a number of parametric studies were conducted to determine the effect of sensor orientation, sensor diameter, laminate thickness, and composite shear strength on the compression strength of smart materials. The most striking result is that a sensor embedded at 30° to the reinforcing fibers appears to degrade the strength as much as one embedded at 90°.

The models presented herein are not intended to provide the final word on any of the cases studied. In particular, work still remains to be done on the ineffective length problem and the compression strength problem. It is hoped, however, that this work will provide a base on which future work may build.

REFERENCES

1. Tsai S. W. and Wu E. M., "A General Theory of Strength for Anisotropic Materials." *Journal of Composite Materials*, Volume 5 (1971), pp. 58-80.

2. Madhukar M. S. and Drzal L. T., "Fiber-Matrix Adhesion and Its Effect on Composite Mechanical Properties: I. Inplane and Interlaminar Shear Behavior of Graphite/Epoxy Composites," *Journal of Composite Materials*, Volume 25 (1991), pp. 932-957.

3. Madhukar M. S. and Drzal L. T., "Fiber-Matrix Adhesion and Its Effect on Composite Mechanical Properties: II. Longitudinal (0°) and Transverse (90°) Tensile and Flexure Behavior of Graphite/Epoxy Composites," *Journal of Composite Materials*, Volume 25 (1991), pp. 958-991.

4. Madhukar M. S. and Drzal L. T., "Effect of Fiber-Matrix Adhesion on the Longitudinal Compressive Properties of Graphite/Epoxy Composites, " *Proceedings of the Fifth Technical Conference of the American Society for Composites*, 1990, pp. 849-858.

5. Pagano N. J. and Tandon G. P., "Elastic Response of Multi-Directional Coated-fiber Composites," *Composites Science and Technology*, Volume 31 (1988), pp. 273-293.

6. Aboudi J., "Micromechanical Analysis of the Strength of Unidirectional Fiber Composites," *Composites Science and Technology*, Volume 33 (1988), pp. 79-96.

7. Ghosn L. J. and Lerch B. A., "Optimum Interface Properties for Metal Matrix Composites", NASA Technical Memorandum 102295, August 1989.

8. Arnold S. M. and Wilt T. E., "Influence of Engineered Interfaces on Residual Stresses and Mechanical Response in Metal Matrix Composites", NASA Technical Memorandum 105438, March 1992.

9. Carman G. P., Averill R. C., Reifsnider K. L., and Reddy J. N. "Optimization of Fiber Coatings to Minimize Stress Concentrations in Composite Materials," submitted to *Journal of Composite Materials*, March 1992.

10. Carman G. P. and Reifsnider K. L., "Analytical Minimization of the Obtrusive Behavior of Embedded Actuators and Sensors," *Journal of Intelligent Material System and Structures*, to appear January 1993.

11. Rosen B. W., "Fiber Composite Materials," *American Society of Metals*, Chapter 3 (1964), pp. 37-75.

12. Whitney J. M. and Drzal L. T., "Axisymmetric Stress Distribution Around an Isolated Fiber Fragment," *ASTM STP 937* (1987), pp. 179-196.

13. Hedgepeth J. M. and Van Dyke P., "Local Stress Concentrations in Imperfect Filamentary Composite Materials," *Journal of Composite Materials,* Volume 1 (1967), pp. 294-309.

14. Carman G. P., Lesko J. J, and Reifsnider K. L., "Micromechanical Analysis of Fiber Fracture," *ASTM STP 1156* (1991), in press.

15. Fajardo A. B., *Stress Concentration Measurements in a Composite Macro-Model Containing Fiber Fracture*, Senior Project Report, Virginia Polytechnic Institute & State University, (1992).

16. Harlow D. G. and Phoenix S. L., "Probability distributions for the strength of composite materials I: two-level bounds," *International Journal of Fracture*, Volume 17, No. 4 (1981), pp. 347-372.

17. Batdorf S. B., "Tensile Strength of Unidirectional Reinforced Composites--I," *Journal Reinforced Plastics and Composites,* Volume 1 (1982), pp. 153-176.

18. Gao Z., Reifsnider K. L., and Carman G. P., "Strength Prediction and Optimization of Composites with Statistical Fiber Flaw Distributions," *Journal of Composite Materials*, Volume 26, No. 11 (1992).

19. Roberts S. S. and Davidson R., "Mechanical Properties of Composite Materials Containing Embedded Fibre Optic Sensors," *SPIE*, V. 1588, Fiber Optic Smart Structures & Skins IV (1991), pp. 326-341.

20. Carman G. P., Paul C., and Sendeckyj G. P., "Transverse Strength of Composites Containing Optical Fibers," Smart Materials and Structures Conference, Albuquerque, NM (1993).

21. Dasgupta A., Wan Y., Sirkis J. and Singh H., "Micro-mechanical Investigation of an Optical Fiber Embedded in a Laminated Composite," *SPIE,* V. 1370, Fiber Optic Smart Structures & Skins III (1990), pp. 119-128.

22. Hashin Z. and Rosen B. W., "The Elastic Moduli of Fiber-Reinforced Materials," *Journal of Applied Mechanics*, (1964), pp. 223-232.

23. Reifsnider K. L., ESM 6104 Class Notes, Department of Engineering Science and Mechanics, Virginia Polytechnic Institute & State University.

24. Swartz H. S. and Hartness J. T., "Effect of Fiber Coatings on Interlaminar Fracture Toughness of Composites," *Toughened Composites, ASTM STP 937*, Norman J. Johnston, Ed., American Society for Testing and Materials, Philadelphia, 1987, pp. 150-178.

25. Carman G. P., *Micromechanics of Finite Length Fiber in Composite Materials*, PhD Dissertation, Virginia Polytechnic Institute & State University, December 1991.

26. Swain R. E., Reifsnider K. L., Jayraman K., and El-Zein M., "Interface/Interphase Concepts in Composite Material Systems," *Journal of Thermoplastic Composites*, Volume

3 (1990), pp. 13-23.

27. Pak Y., "Longitudinal Shear Transfer in Fiber Optic Sensor," *Smart Materials and Structures*, Volume 1 (1992), pp. 57-62.

28. Carman G. P. and Sendeckyj, "A Review of Mechanics of Embedded Optical Sensors," to be submitted *Comp. Tech.*

29. Lesko J. J, Case S. W., Fogg B. R., and Carman G. P., "Embedded Fabry Perot Fiber Optic Strain Rosette Sensor for Internal Stress State Assessment," *Proceedings of the Seventh Technical Conference of the American Society for Composites*, (1992).

30. Jensen D. W., Pascual J., and August J. A., "Performance of Graphite/Bismaleimide Laminates with Embedded Optical Fibers. Part 2 Uniaxial Compression," *Smart Mater. Struct.*, Volume 1 pp. 31-36.

31. Jensen D. W. and Pascaul J., "Degradation of Graphite/Bismaleimide Laminate with Multiple Embedded Fiber Optic Sensors," *SPIE*, Volume 1370, Fiber Optic Smart Structures & Skins III (1990), pp. 228-237.

32. Yarcho W. B., "In-House Study to Determine the Effects of Embedded Optical Glass Fibers on the Strength of Graphite Composite Material," Materials and Processes Report, Wright Patterson AFB, Flight Dynamics Lab, MoP-89-Jan-FDBC-006.

33. Measures R. M., Glossop N. D. W., Lymer J., Leblanc M., West J., Dubois S., Tsaw W., and Tennyson R. C., "Structurally Integrated Fiber Optic Damage Assessment Systems for Composite Materials," *Applied Optics*, Volume 28 #13 (1989), pp. 2626-2633.

34. Tsai S. W. and Hahn H. T., *Introduction to Composite Materials,* Technomic (1980), pp. 414-416.

35. Jones R. M., *Mechanics of Composite Materials*, Hemisphere Publishing Corporation (1975), p. 97.

36. Reddy J. N., *Energy and Variational Methods in Applied Mechanics*, Wiley (1984), pp. 184-186.

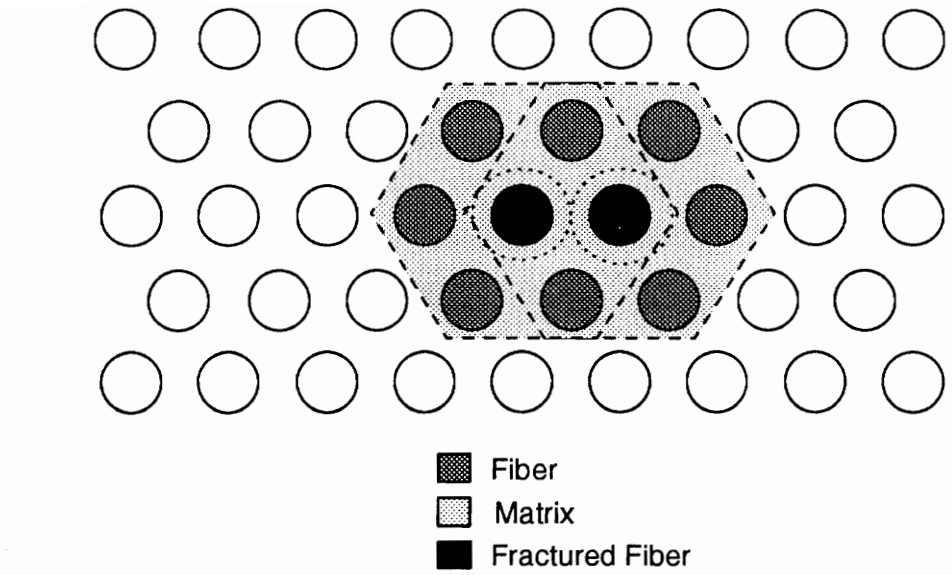

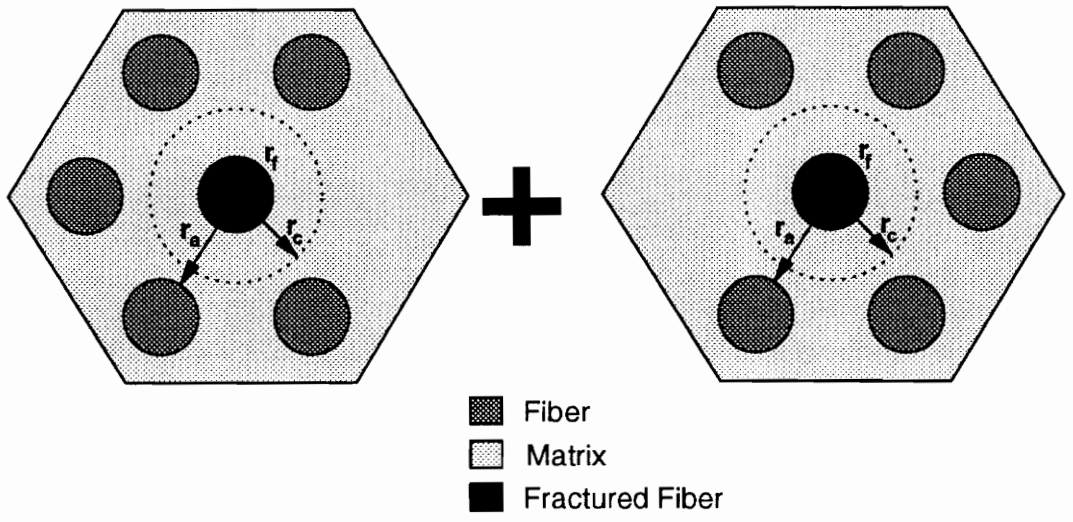

Figure 4. Representation of a composite containing two adjacent fiber fractures using a fiber discount methodology.

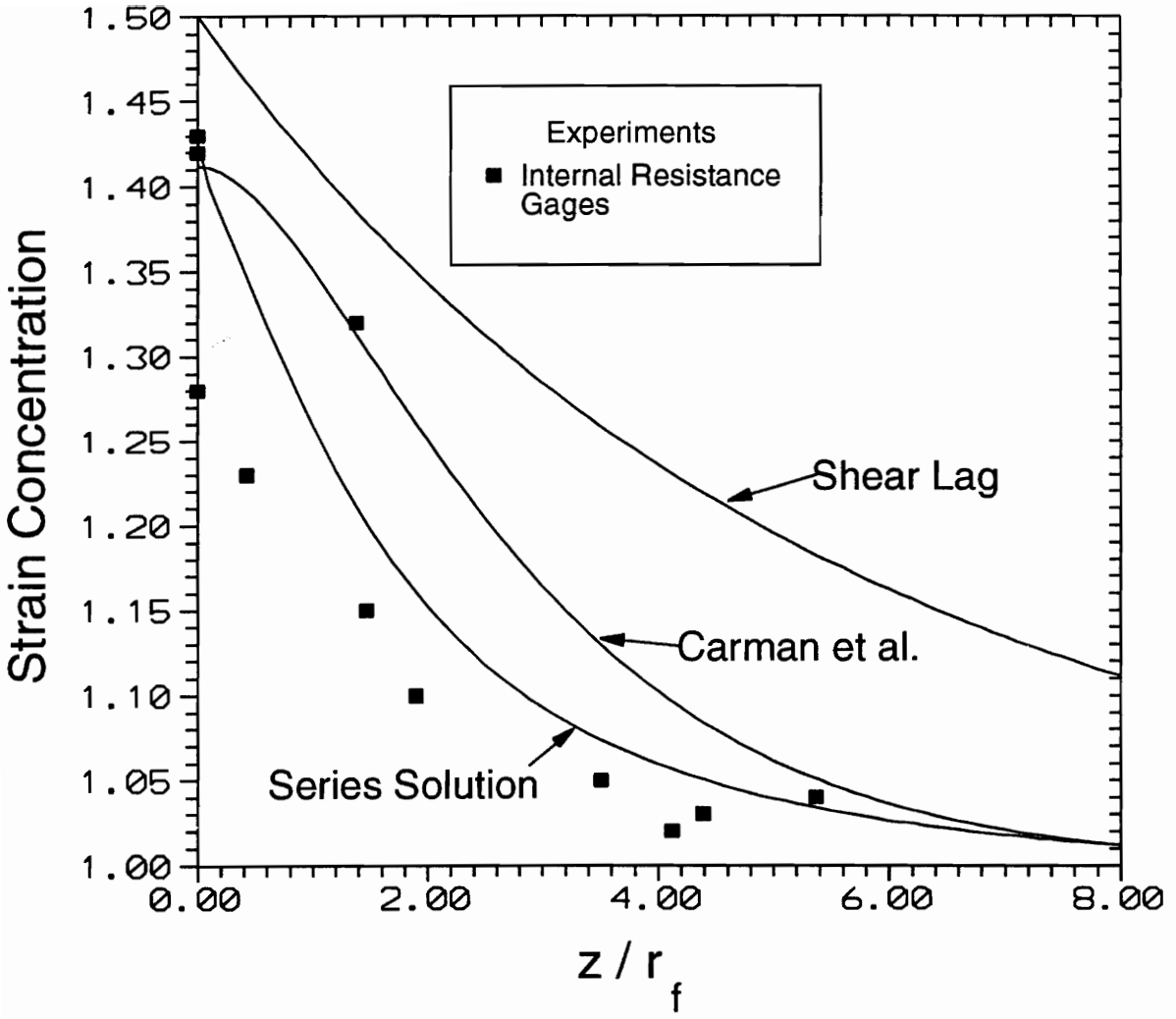

Figure 5. Comparison of strain concentration values determined experimentally with theoretical predictions as a function of axial distance ($r = r_a$) from the plane of the fractured fiber. Results are a 20% fiber volume fraction model composite with $r_c = r_f$.

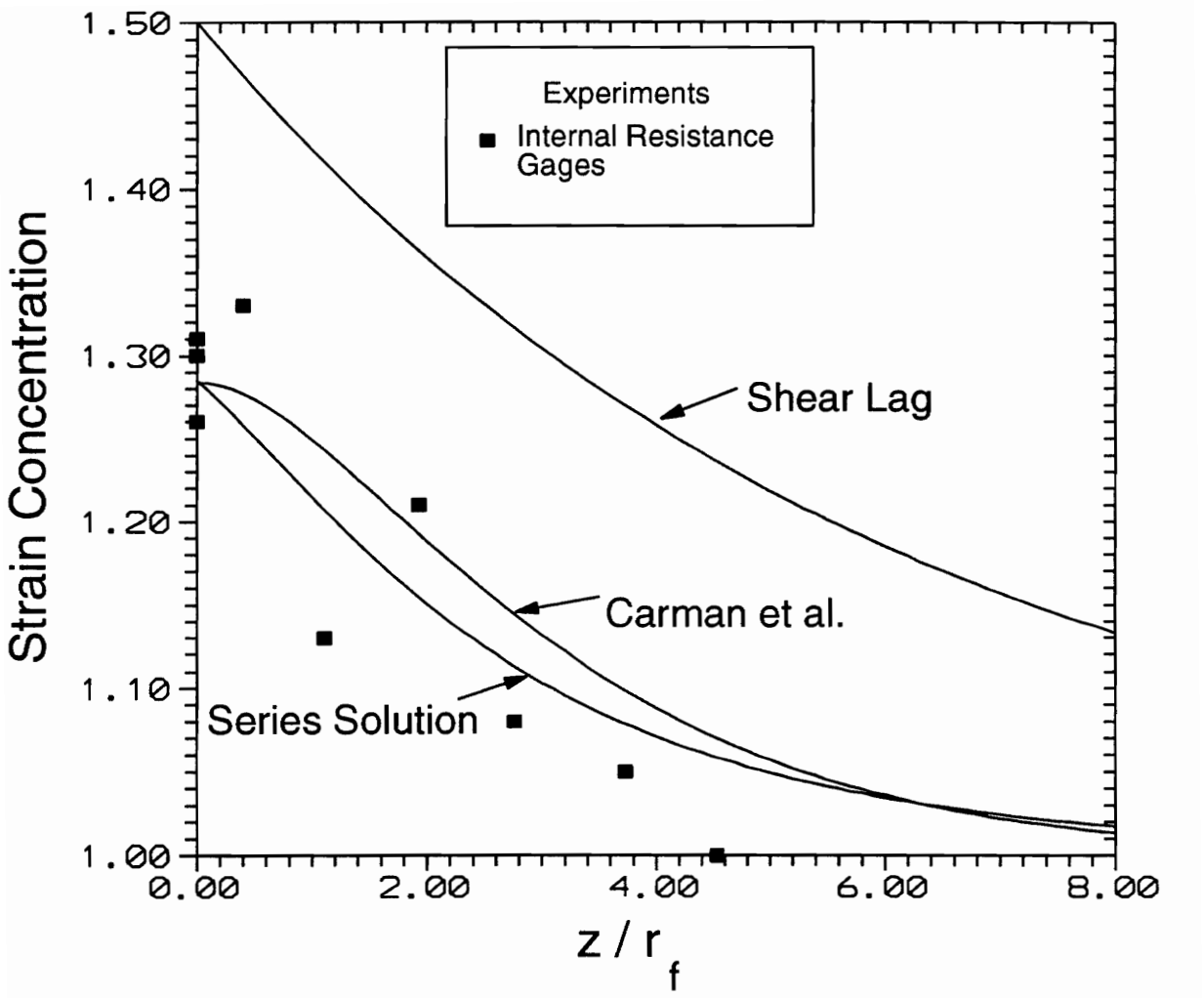

Figure 6. Comparison of strain concentration values determined experimentally with theoretical predictions as a function of axial distance ($r = r_a$) from the plane of the fractured fiber. Results are a 15% fiber volume fraction model composite with $r_c = r_f$.

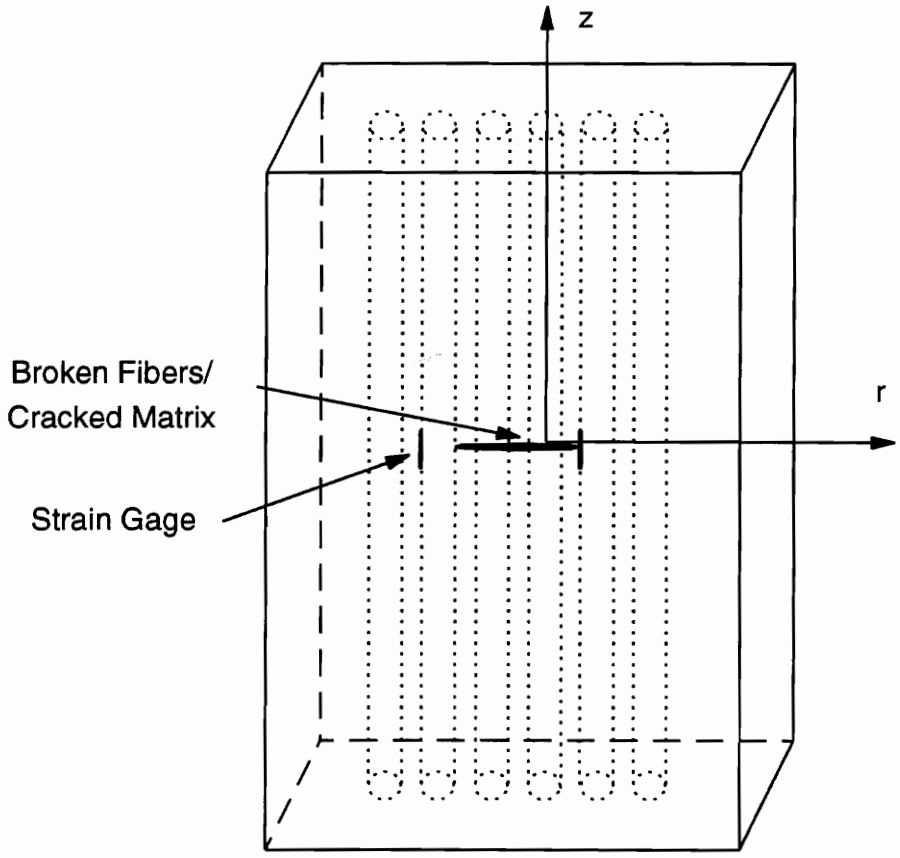

Figure 7. Model composite containing two adjacent fractured fibers.

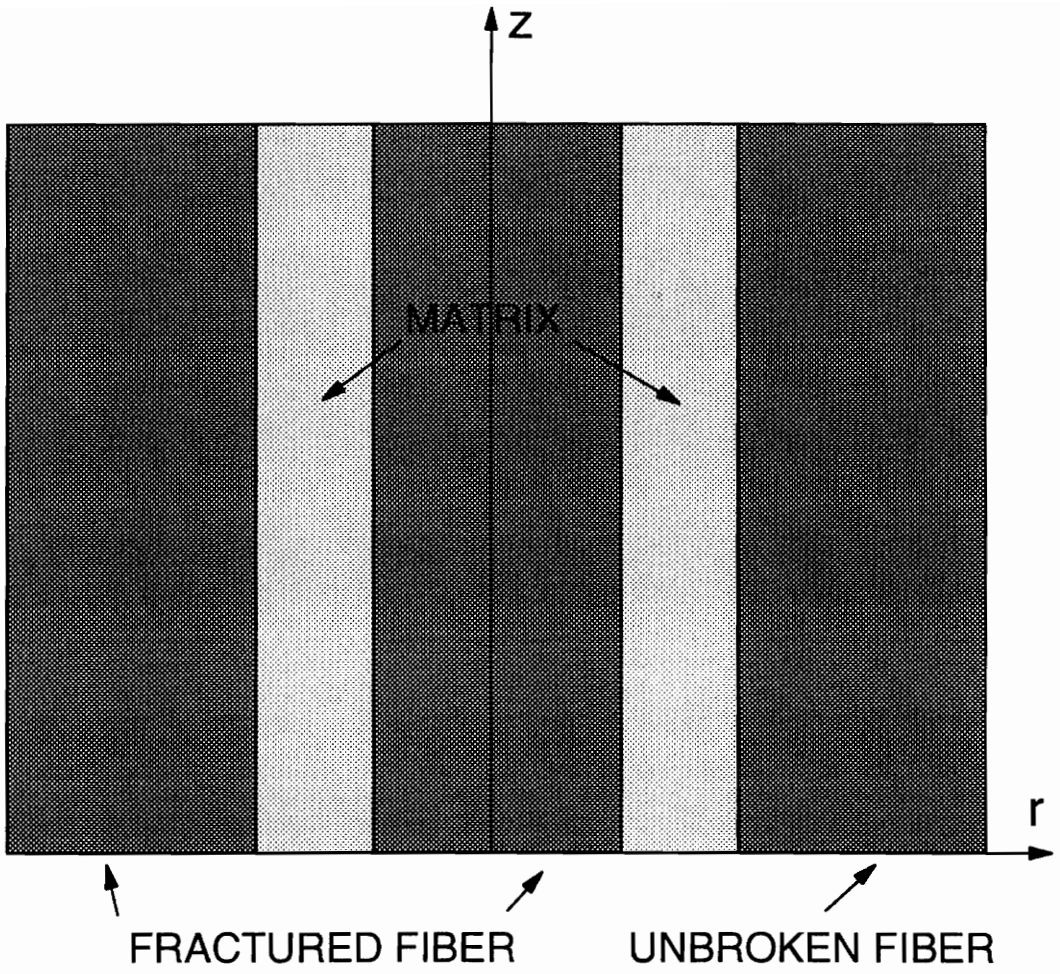

Figure 8. Coordinate system for a model composite containing two adjacent fractured fibers.

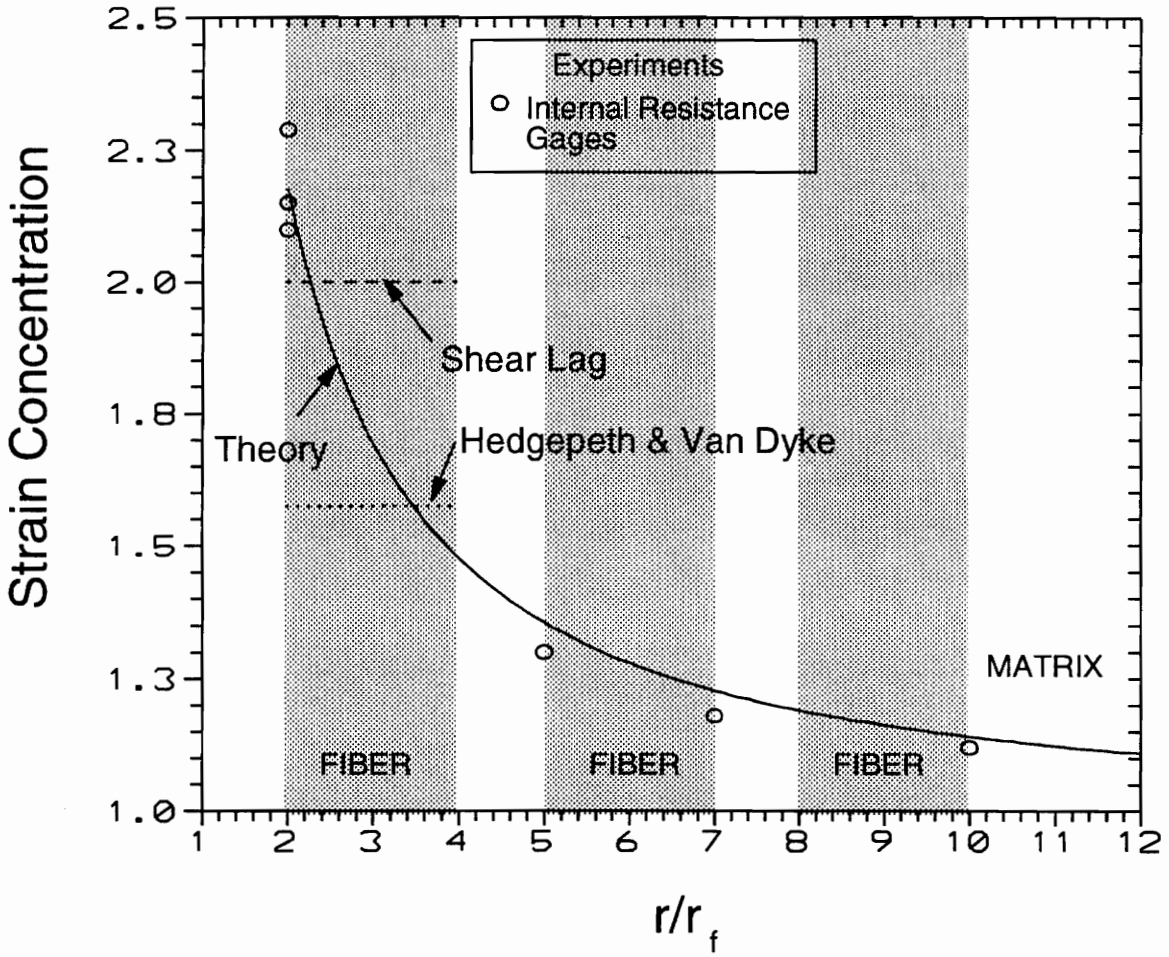

Figure 9. Comparison of strain concentrations determined experimentally with theoretical predictions as a function of radial distance ($z = 0$) from the center of one broken fiber. Results depict a 20% fiber volume fraction model composite in which two adjacent fibers have fractured and $r_c = r_a$.

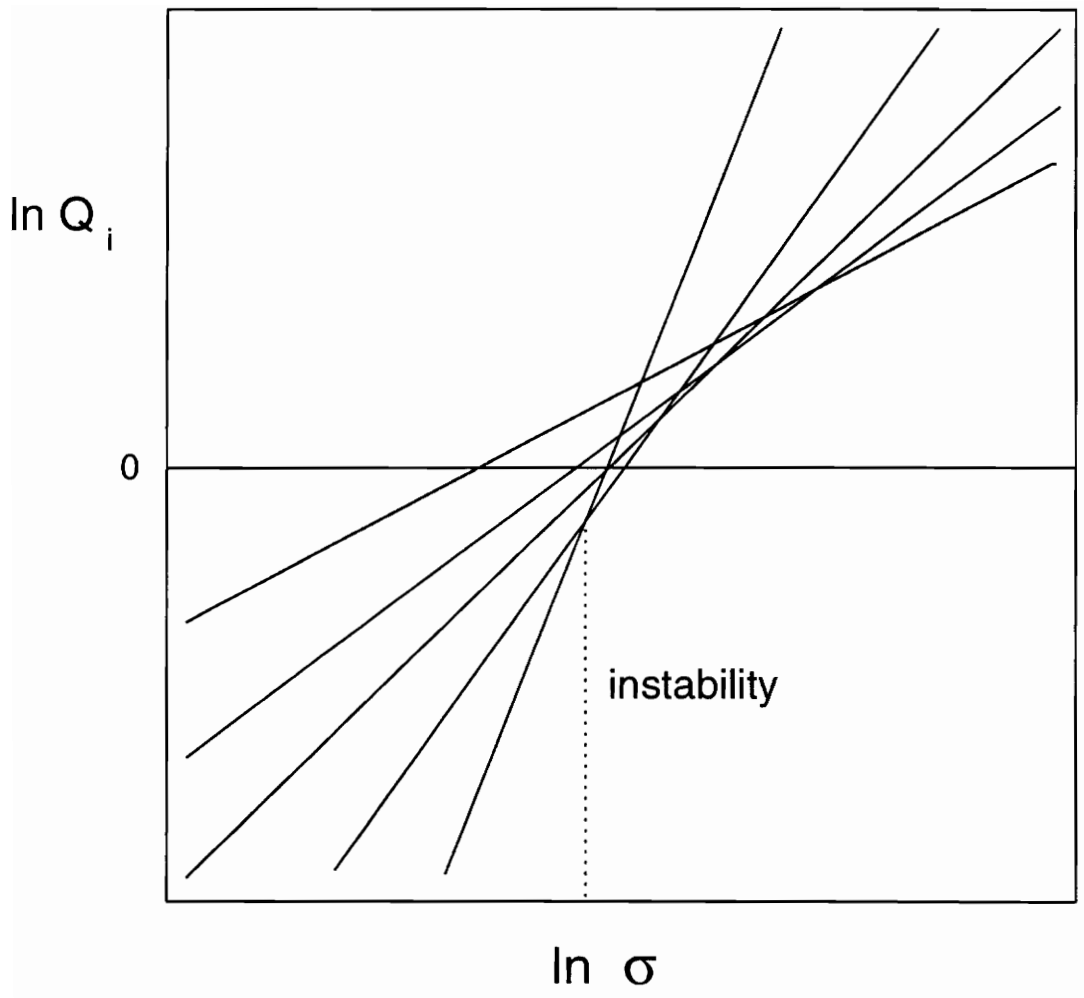

Figure 10. Schematic diagram of a Q-plot from the statistical analysis of Batdorf [17]. Composite failure is predicted to occur at the instability.

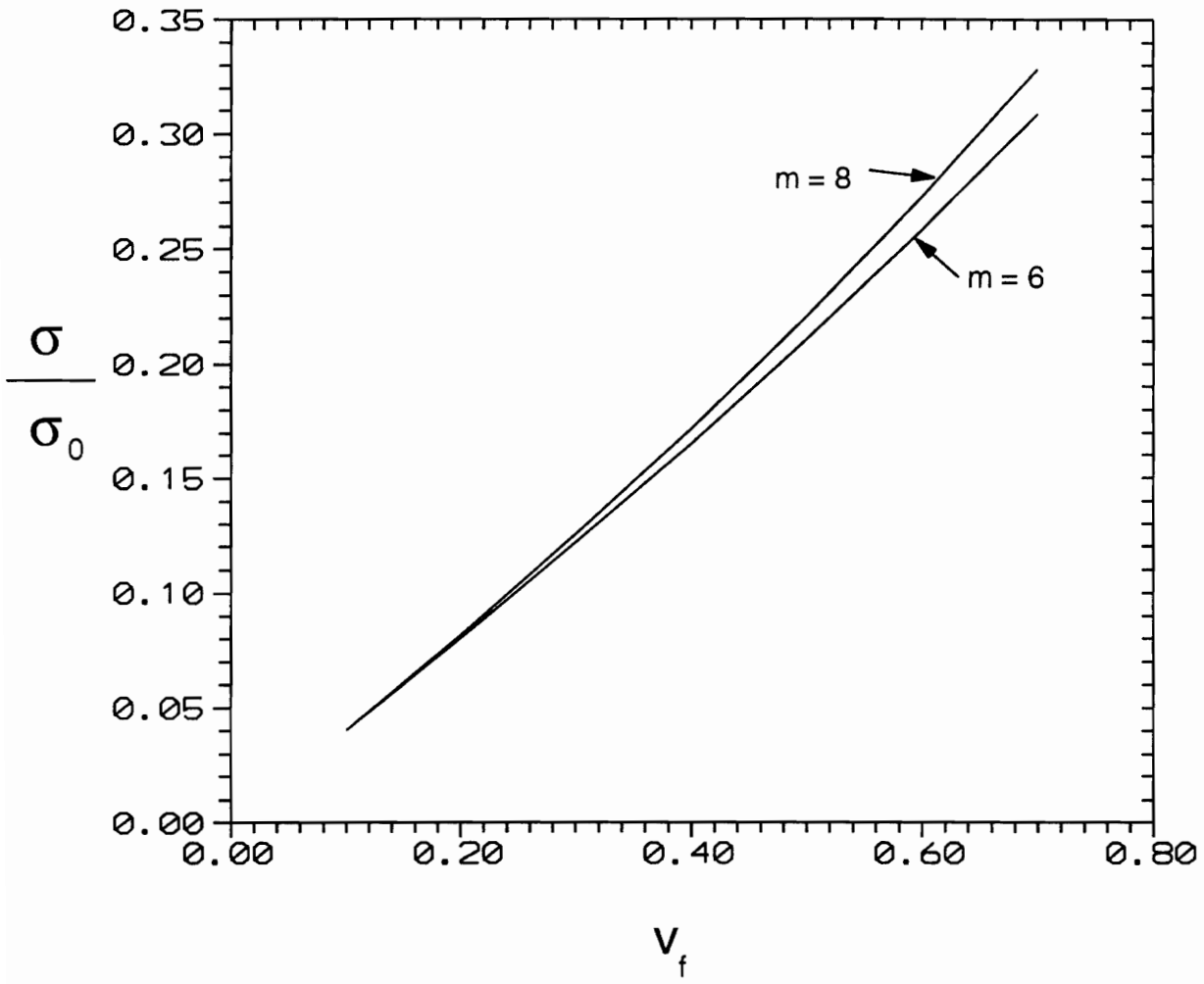

Figure 11. Normalized predicted tensile strength as a function of fiber volume fraction for two values of the Weibull shape factor.

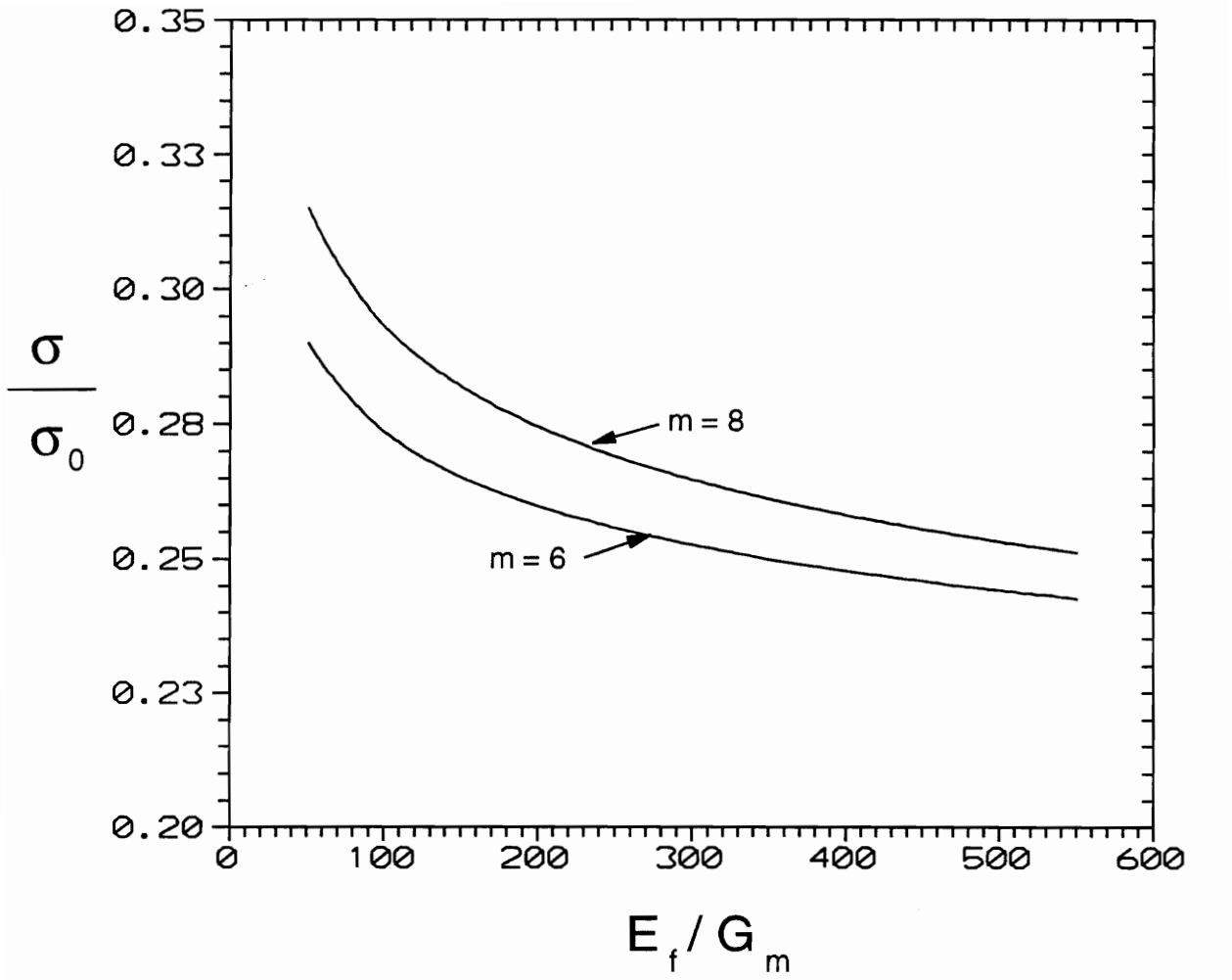

Figure 12. Normalized predicted tensile strength as a function of fiber-matrix stiffness ratio for two values of the Weibull shape factor.

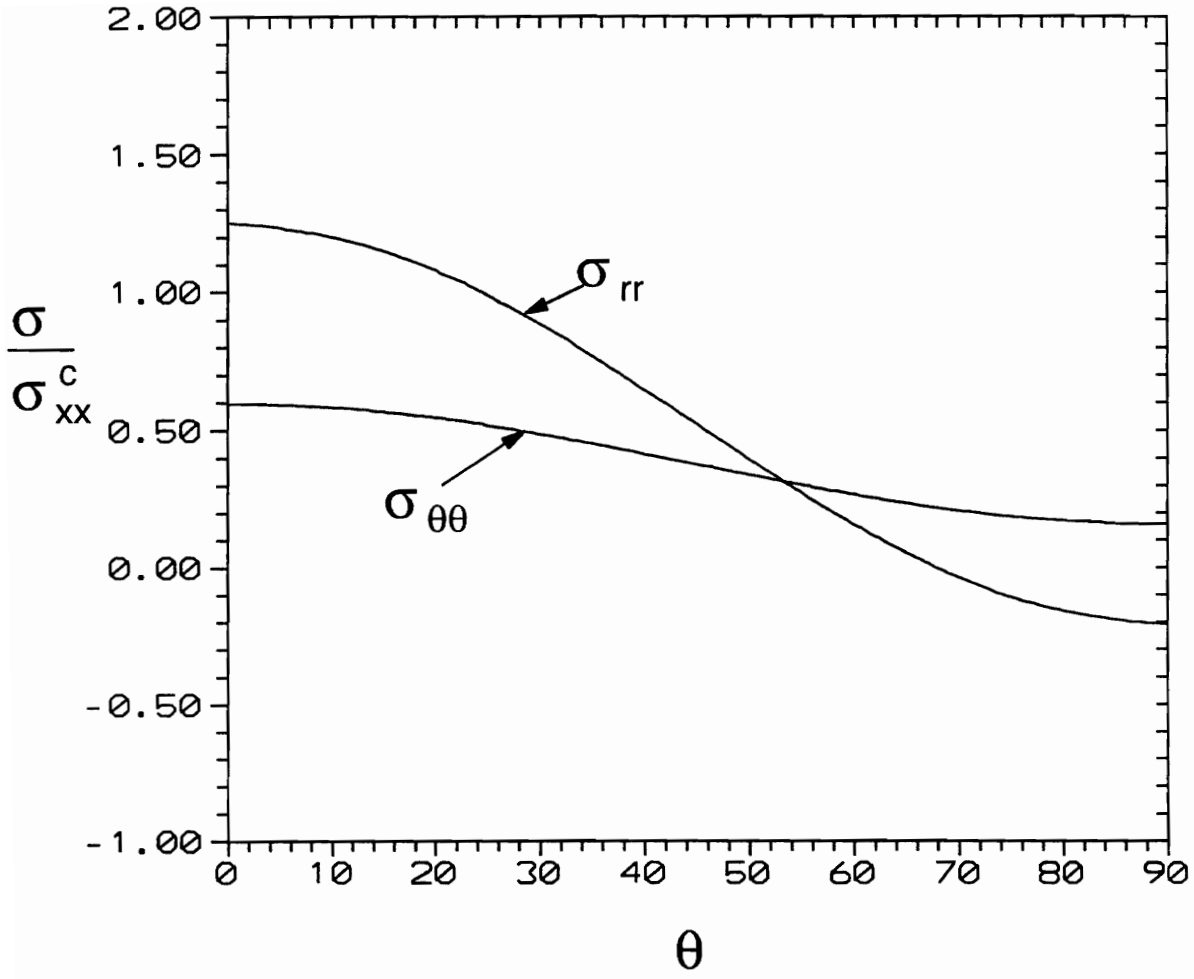

Figure 13. Stress variation for a stiff fiber embedded in a matrix material.

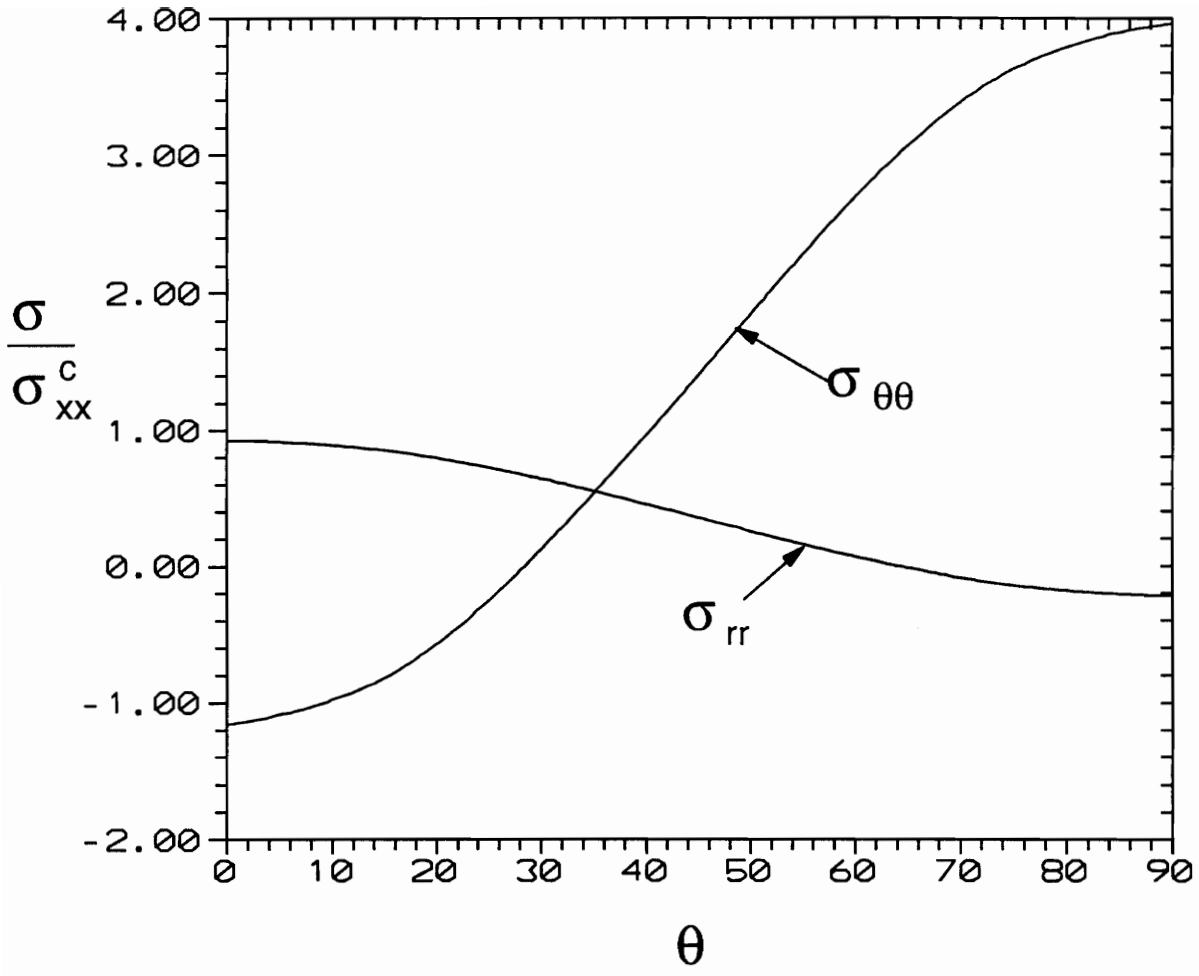

Figure 14. Stress variation for a compliant fiber embedded in a matrix material.

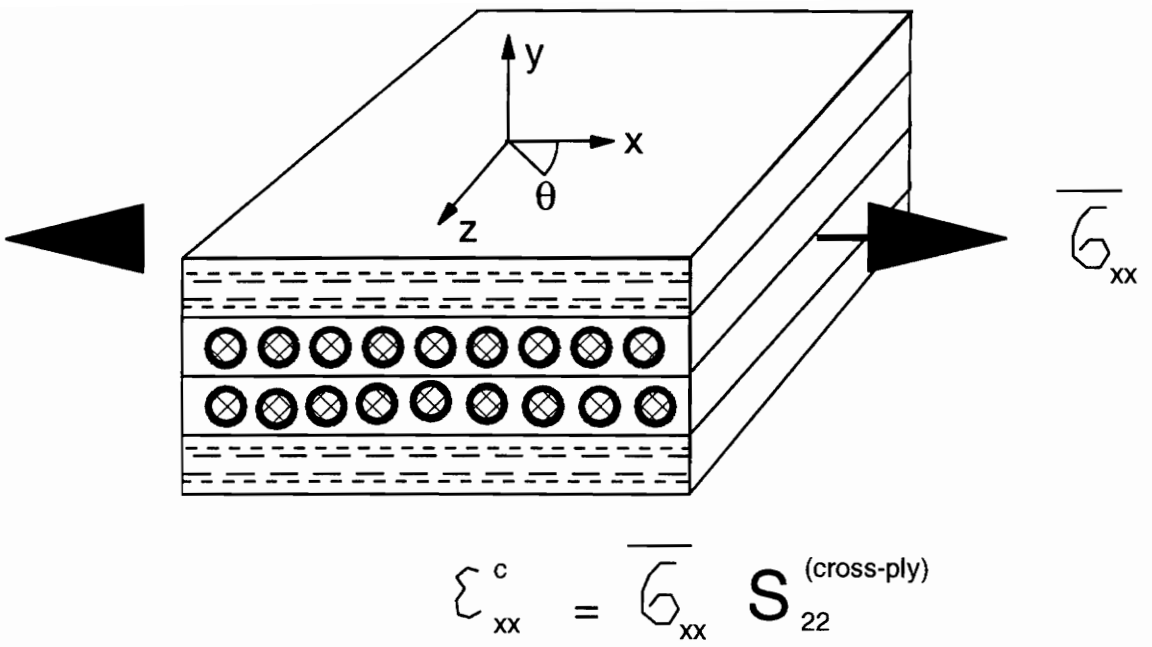

Figure 15. Illustration of the motivation for the boundary conditions applied to the representative volume element.

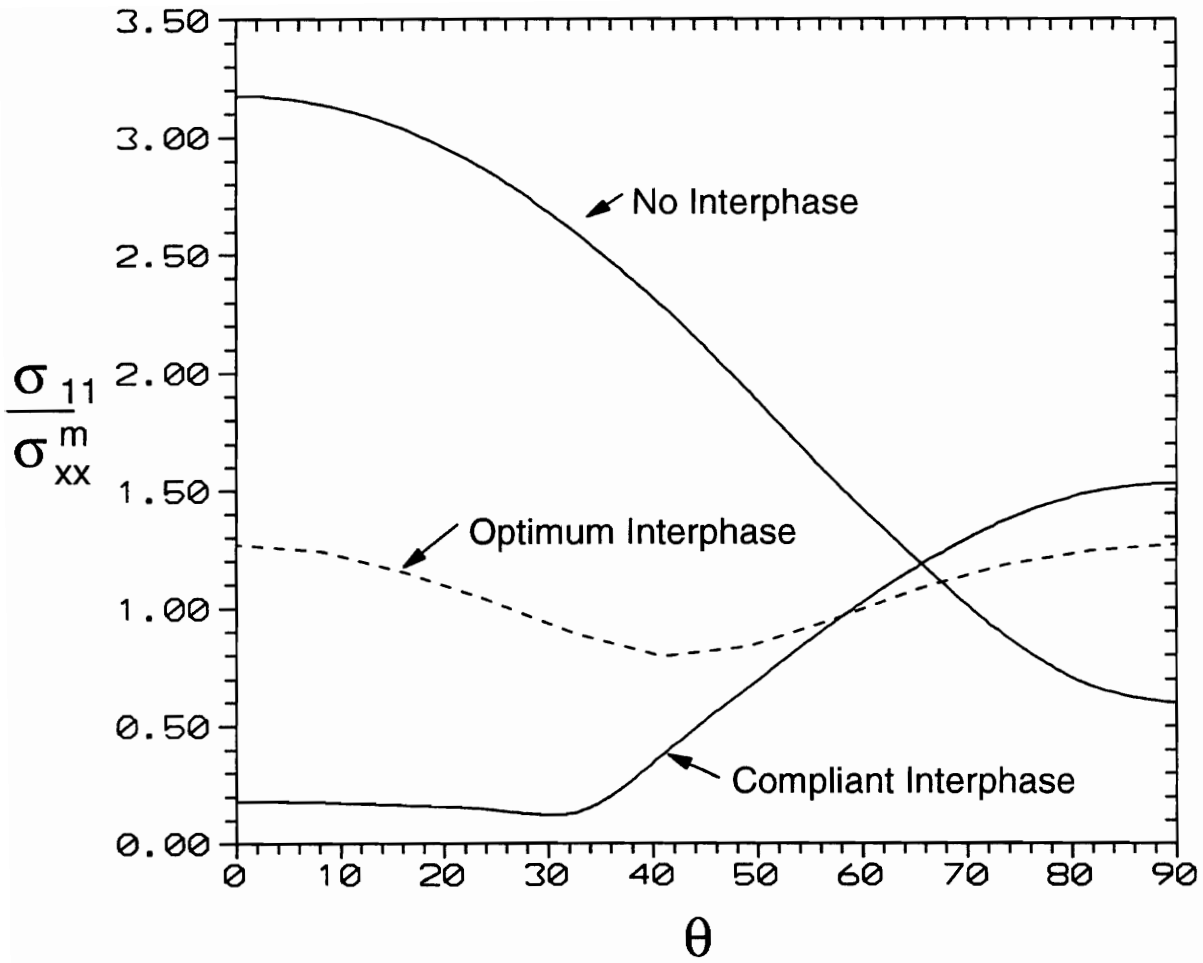

Figure 16. Maximum principal stress variation with orientation angle ($r = r_i$) for a 59% fiber volume fraction AS-4/Epon 828 composite for various interphase materials ($v_i = 13\%$).

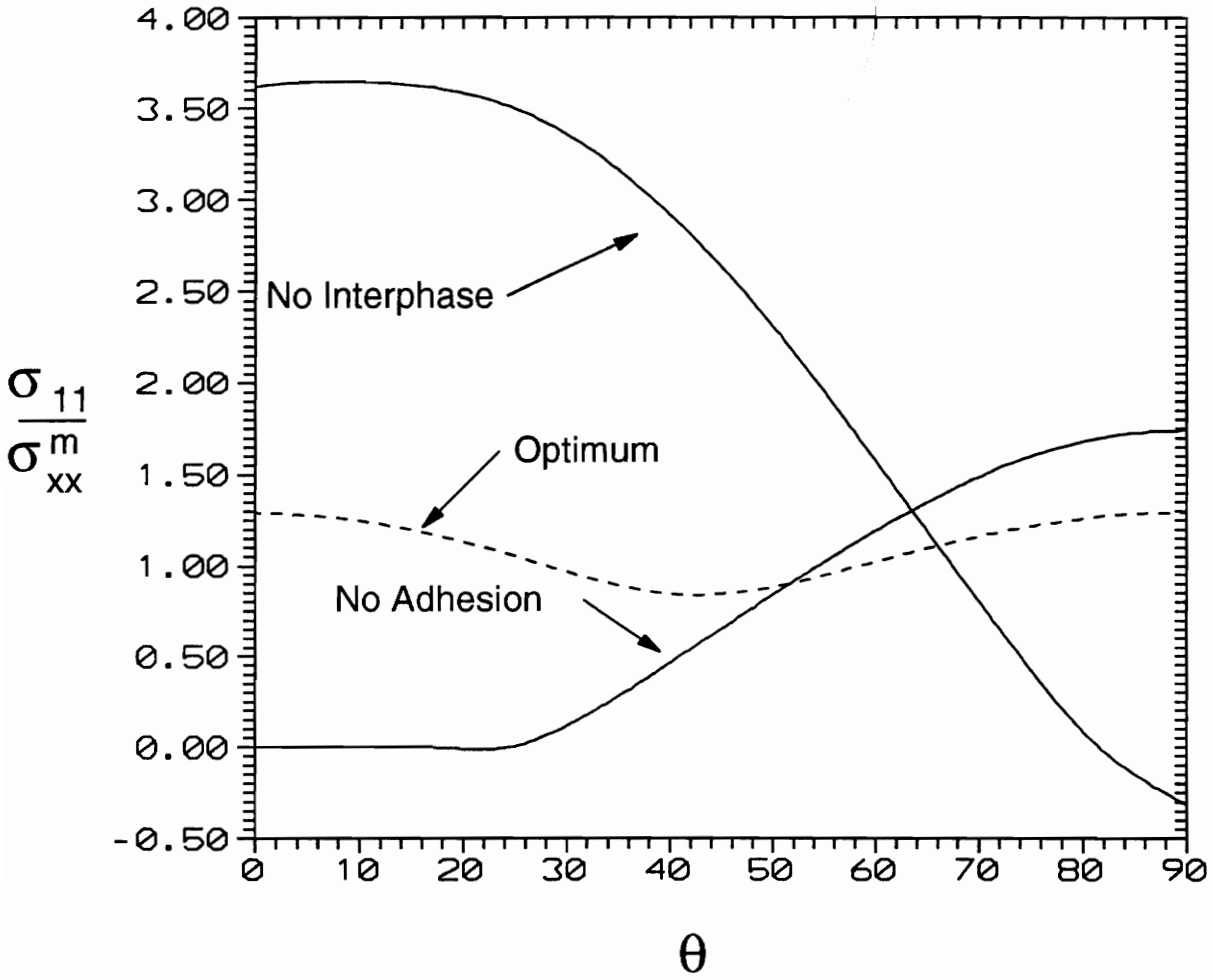

Figure 17. Maximum principal stress variation in the matrix for a glass/epoxy system with a 44% fiber volume fraction.

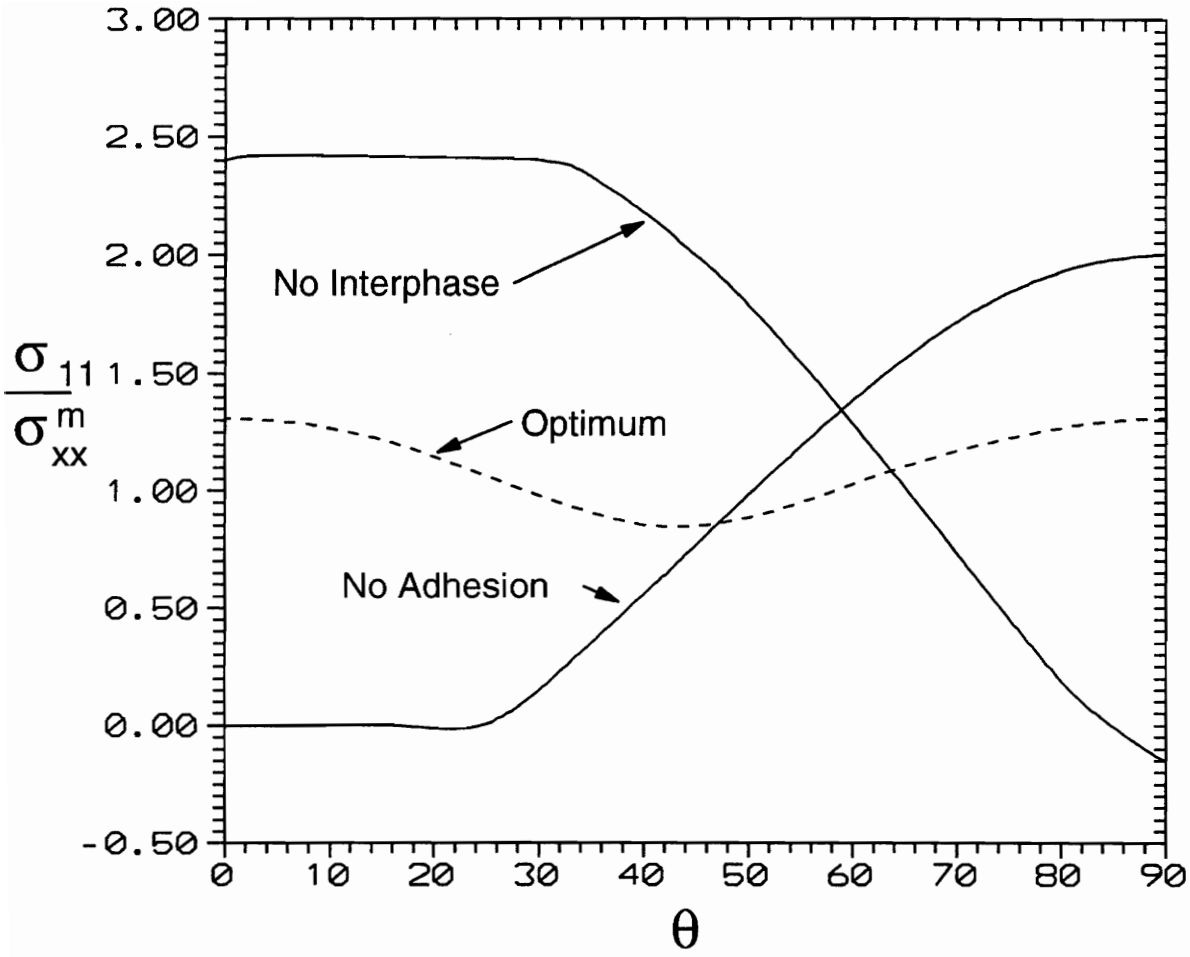

Figure 18. Maximum principal stress variation in the matrix for a glass/epoxy system with a 25% fiber volume fraction.

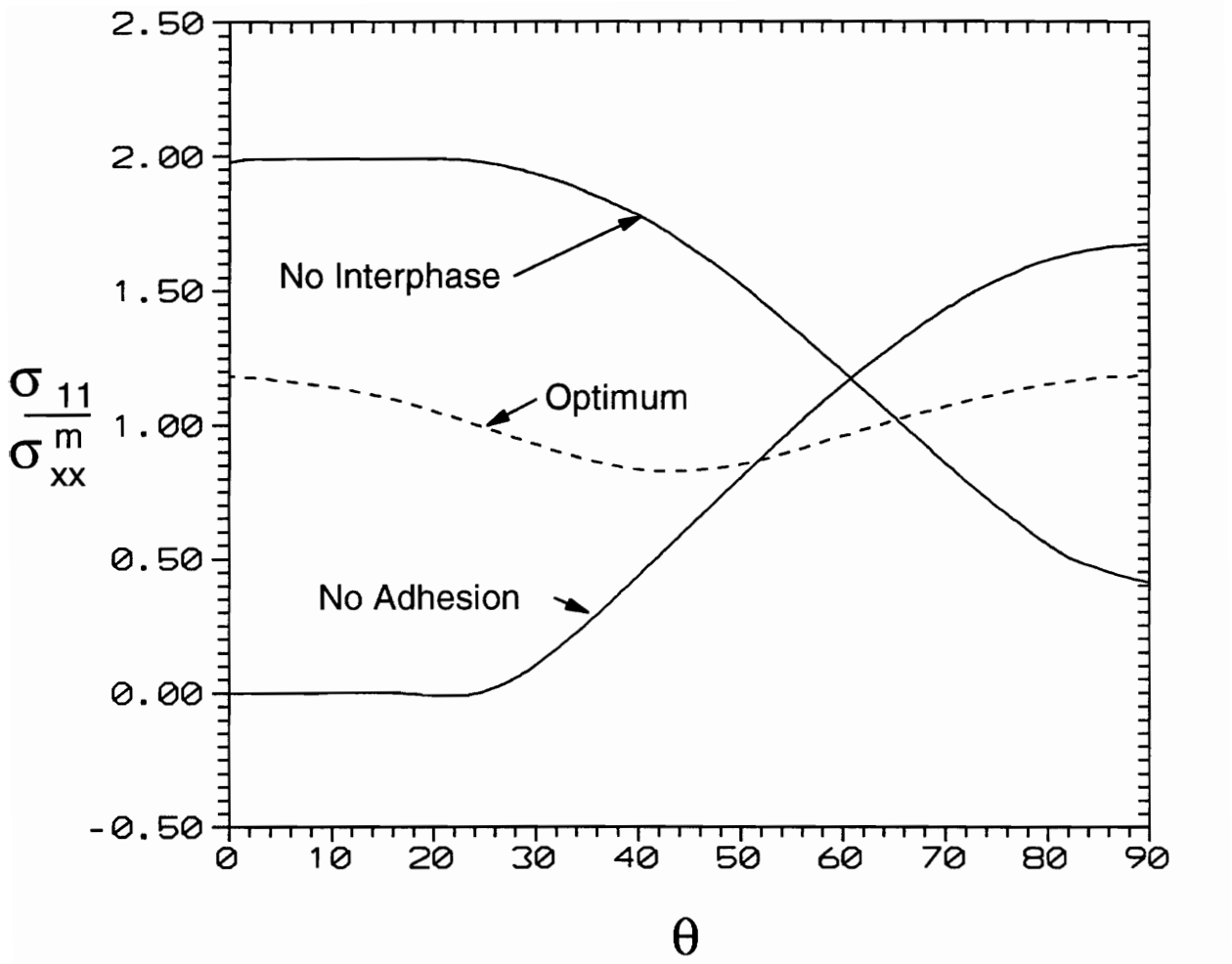

Figure 19. Maximum principal stress variation in the matrix for a wood/epoxy system with a 48% fiber volume fraction.

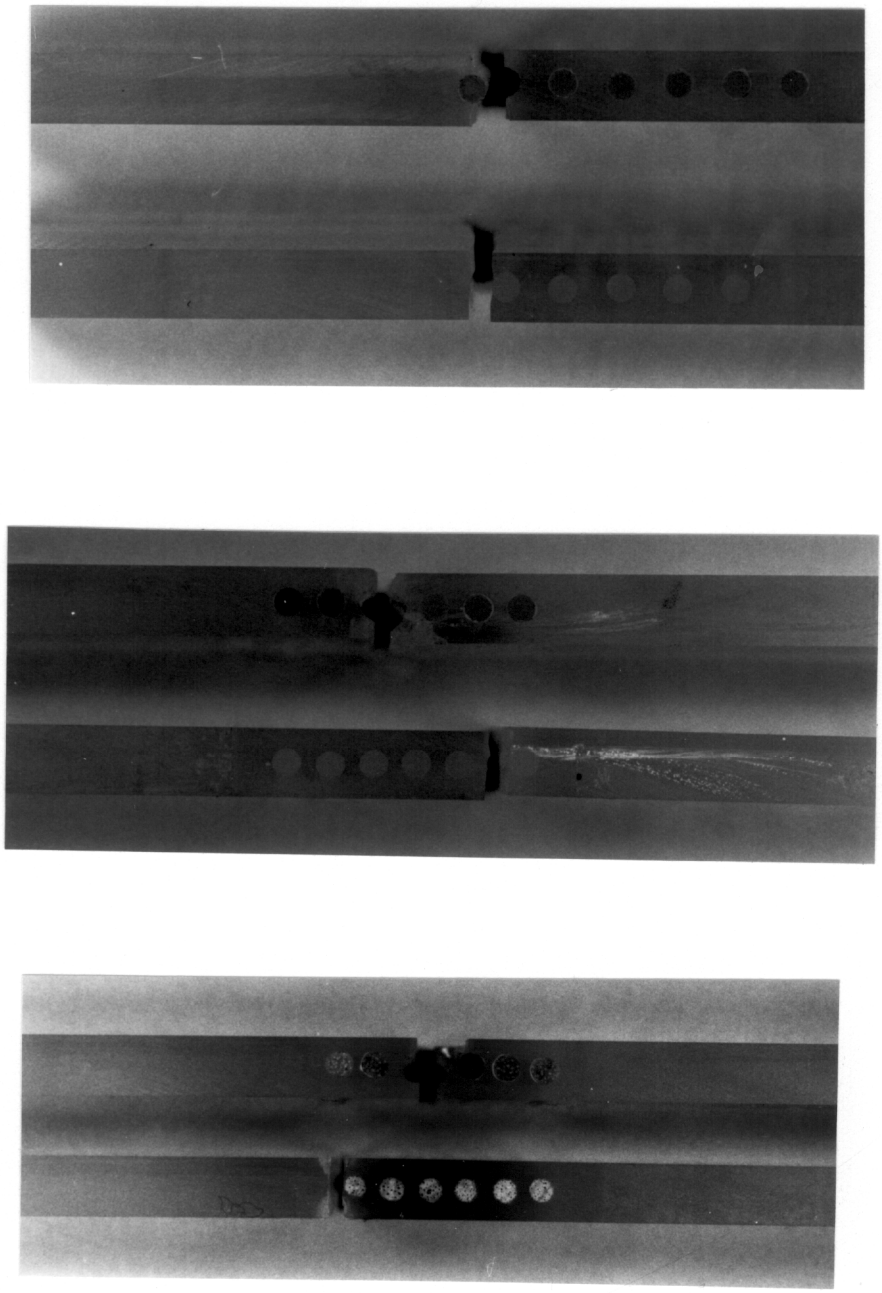

Figure 20. Comparison of failure locations for the three model composite systems studied. Specimens are, from the top: Glass/epoxy (25% fiber volume) no adhesion, Glass/epoxy (25% fiber volume) no coating, Glass/epoxy (44% fiber volume) no adhesion, Glass/epoxy (44% fiber volume) no coating, Wood/epoxy (48% fiber volume) no adhesion, and Wood/epoxy (48% fiber volume) no coating.

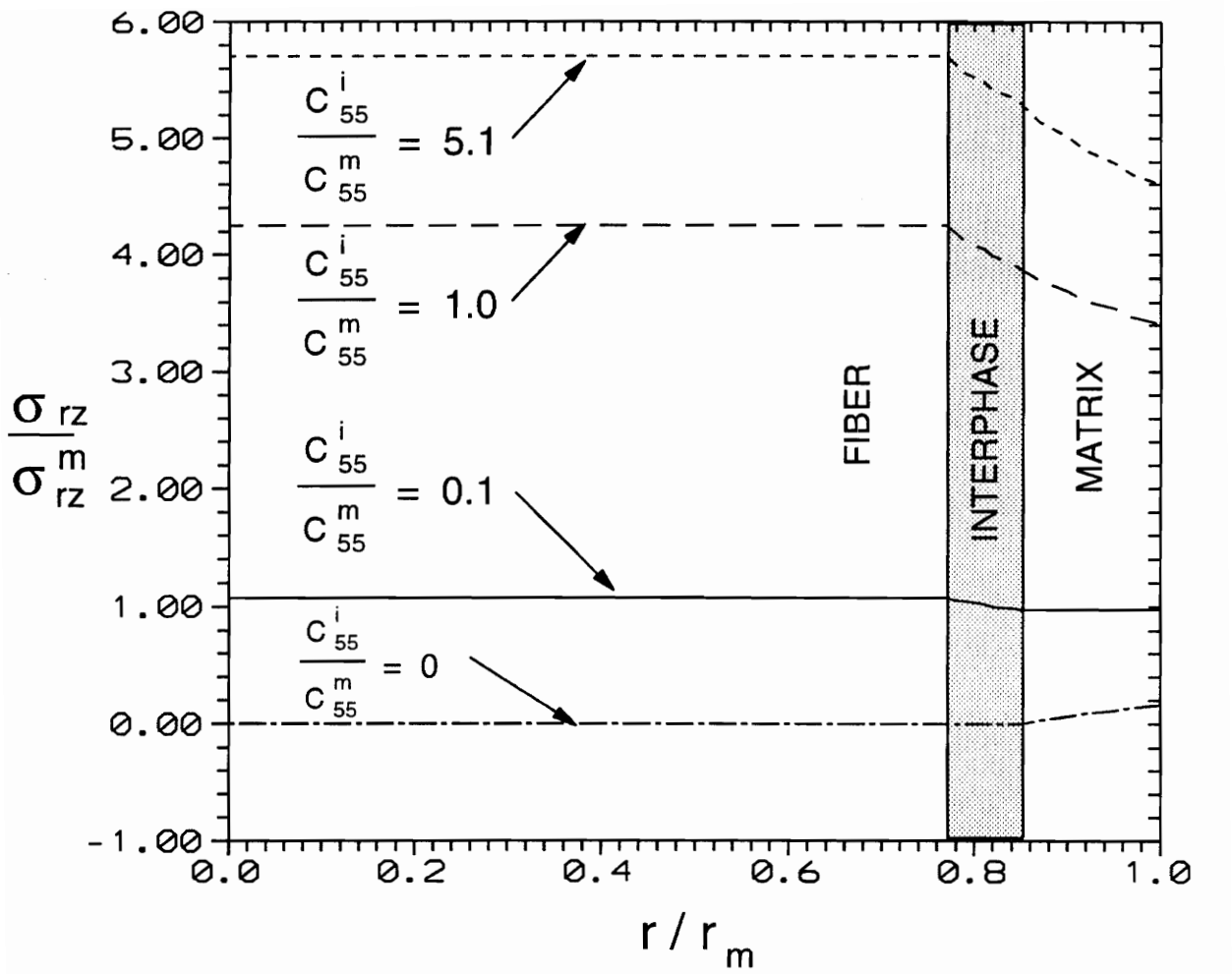

Figure 21. Shear stress variation along $\theta = 0°$ for an AS-4/Epon 828 composite subjected to longitudinal shear loading.

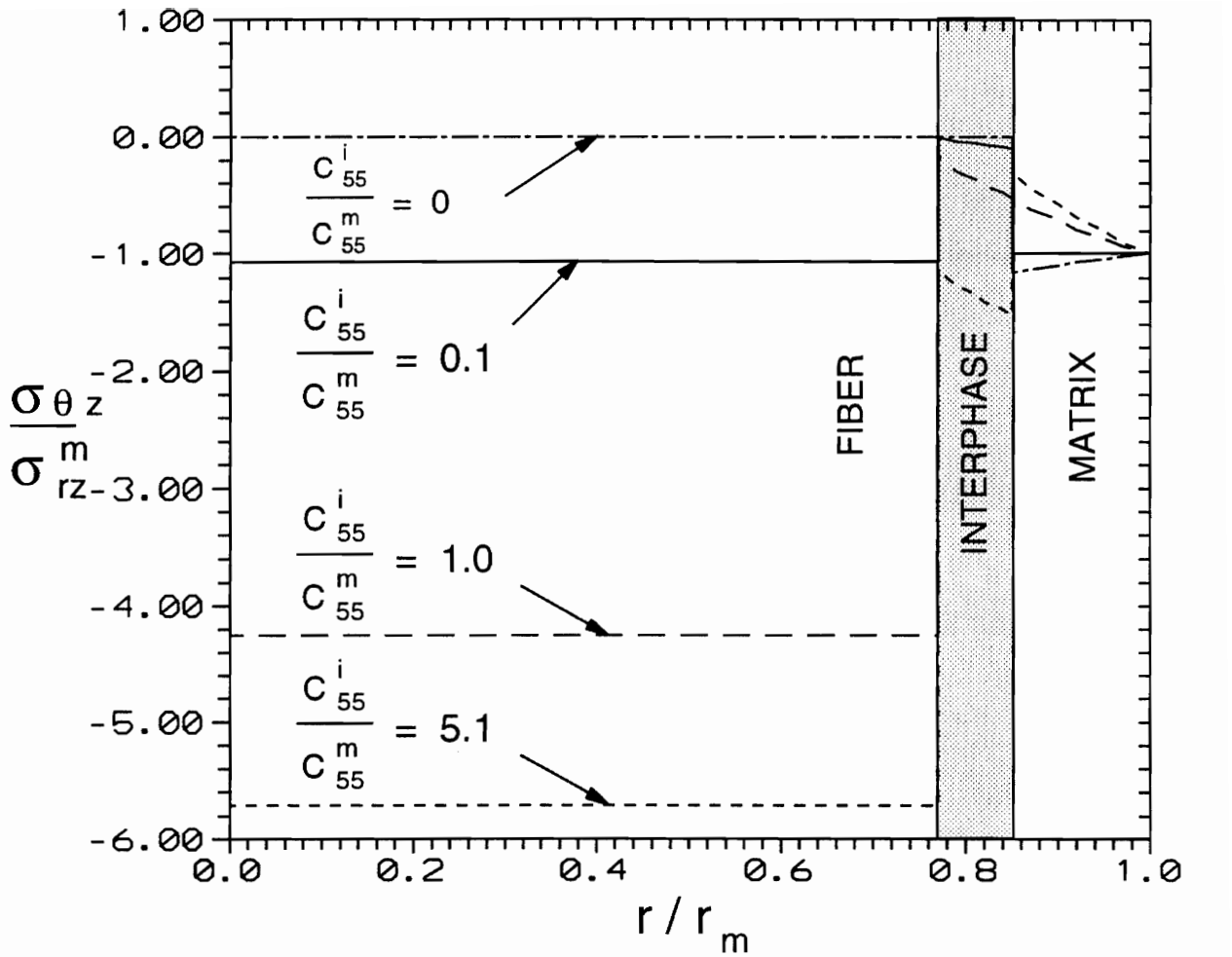

Figure 22. Shear stress variation along $\theta = 90°$ for an AS-4/Epon 828 composite subjected to longitudinal shear loading.

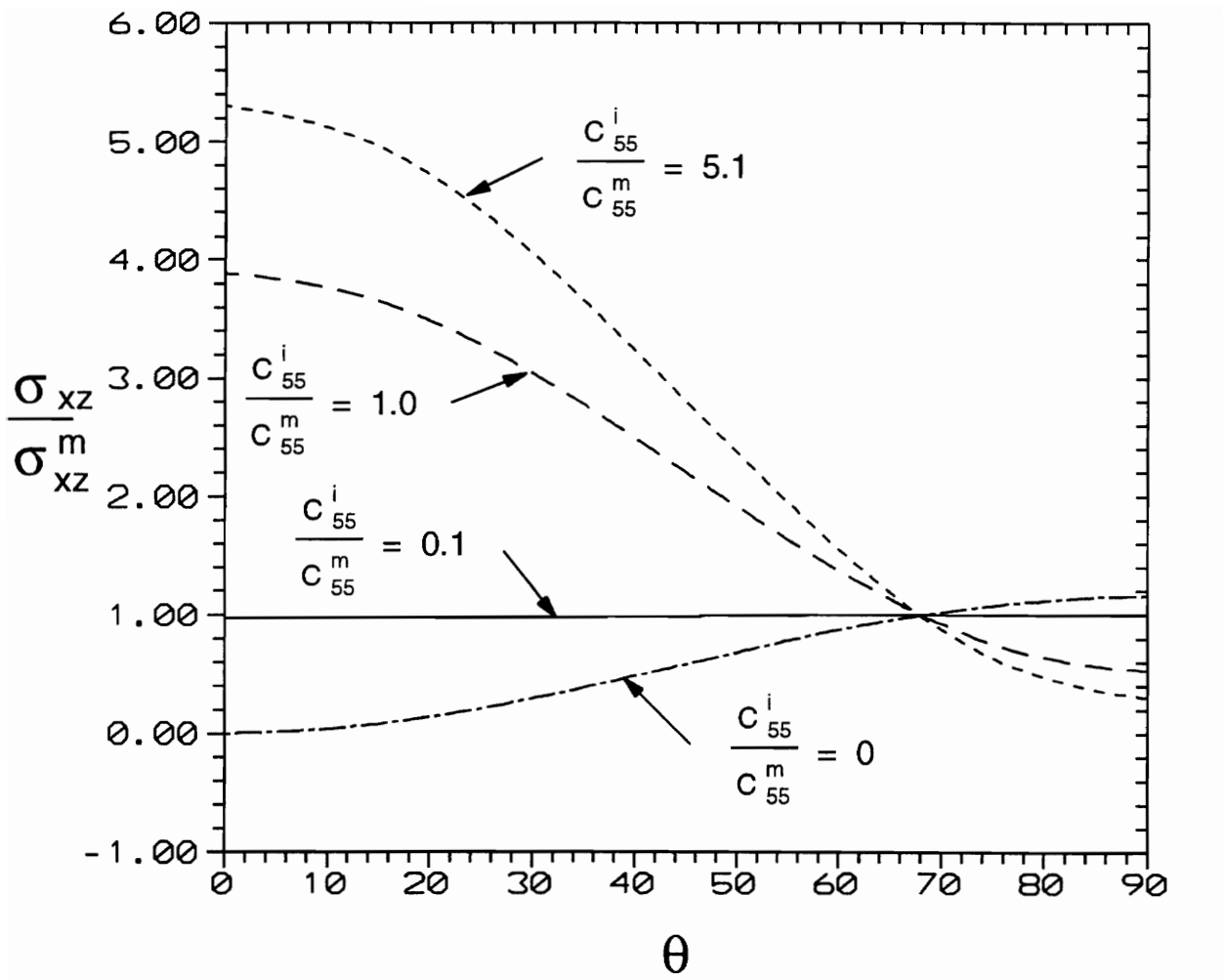

Figure 23. Cartesian shear stress variation for the composite systems studied.

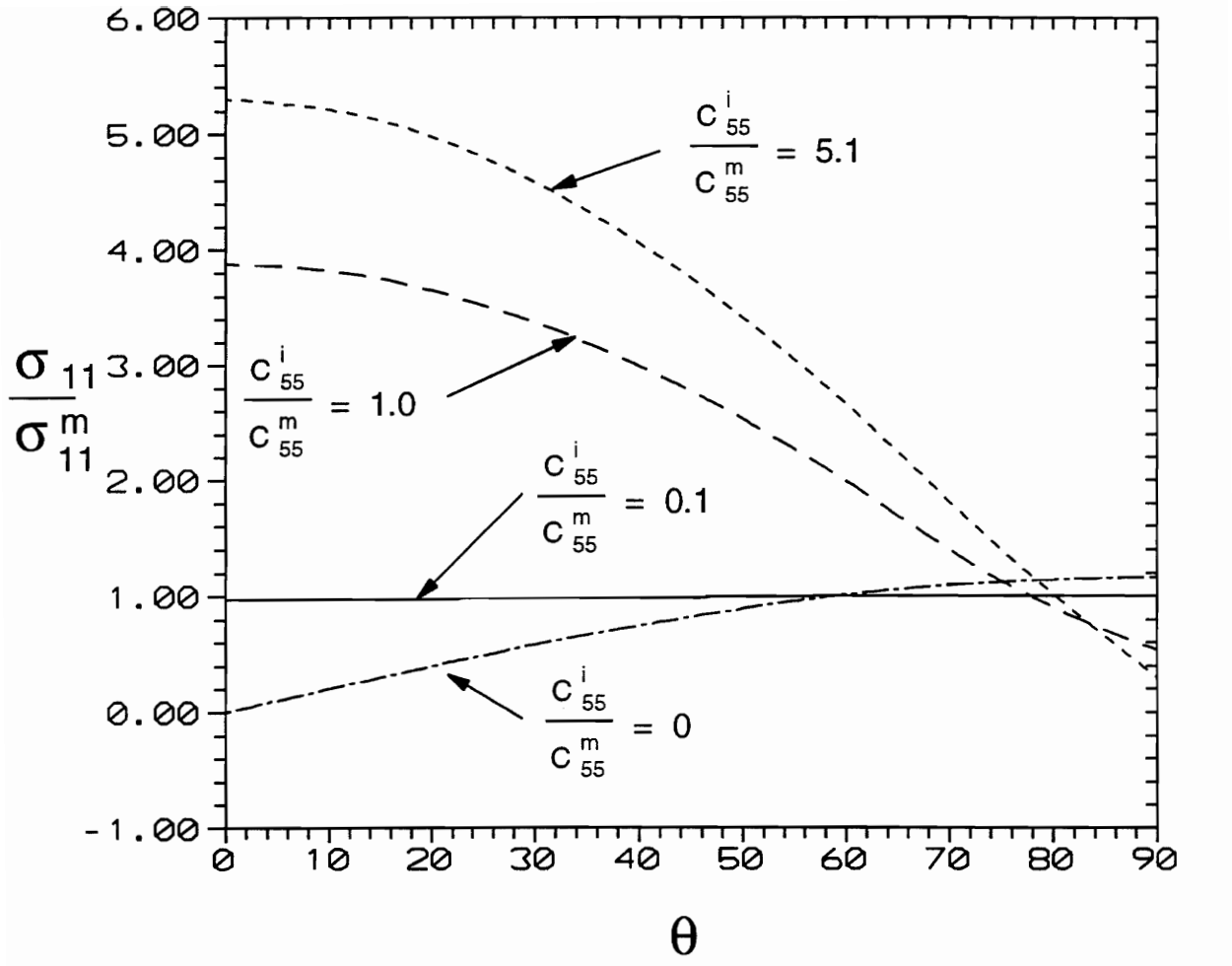

Figure 24. Maximum principal stress at the matrix/interphase interface.

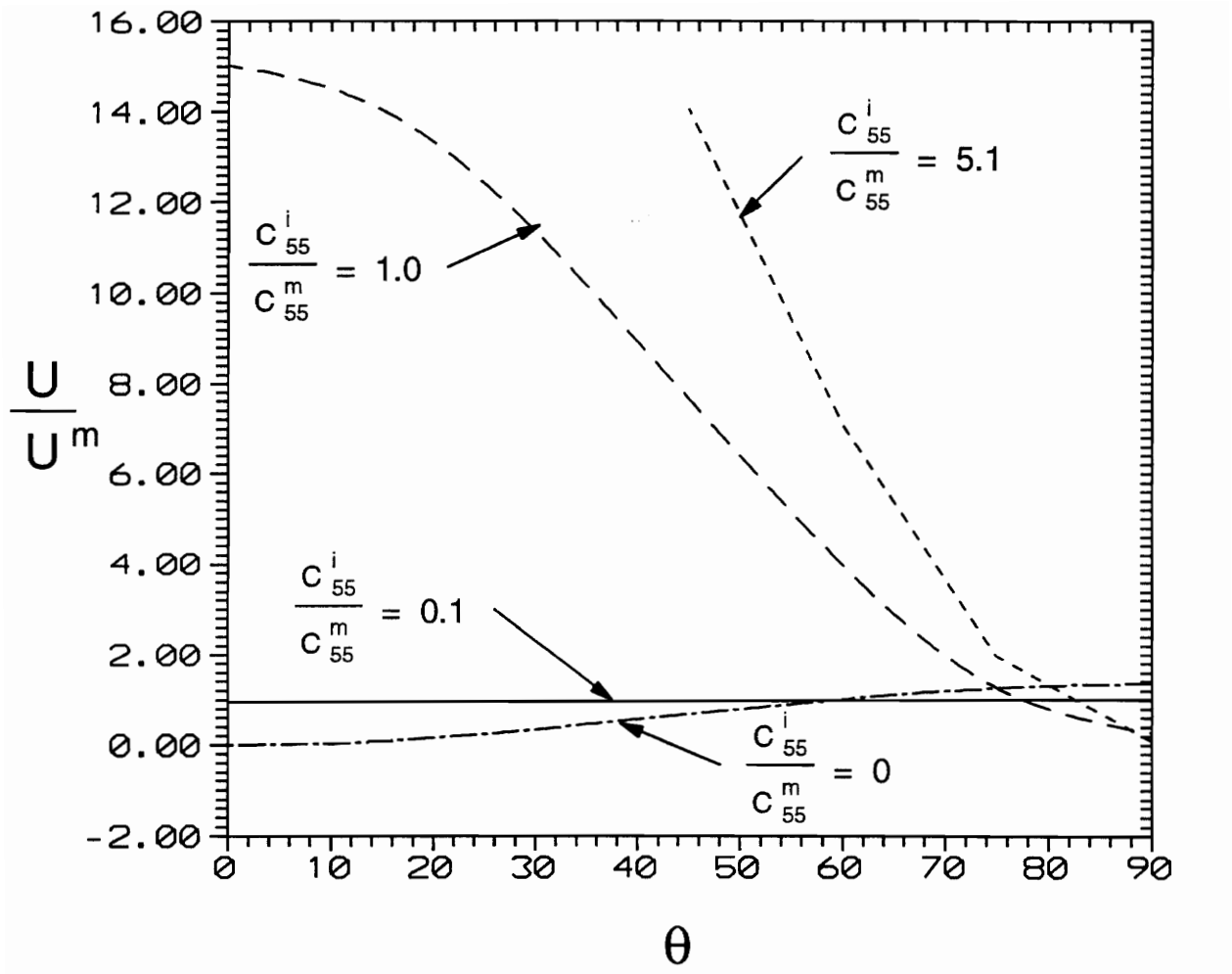

Figure 25. Strain energy density at the matrix/interphase interface.

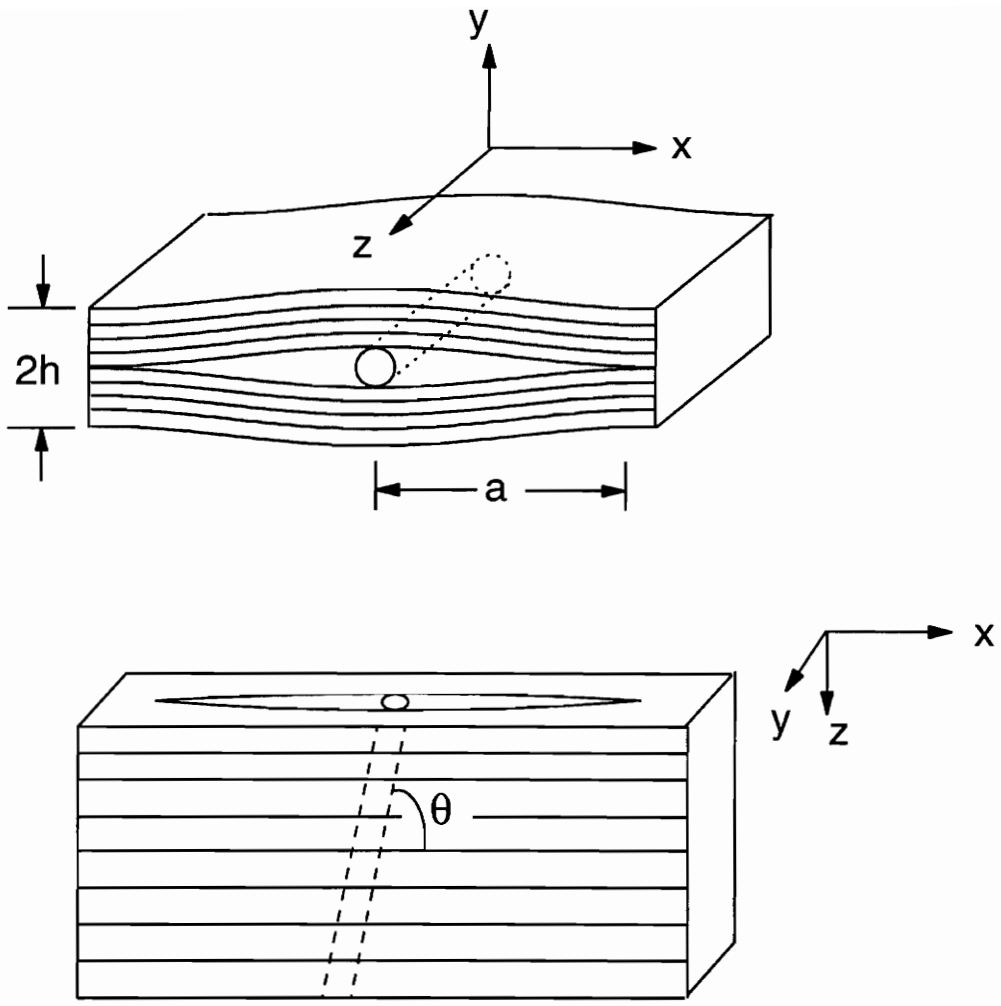

Figure 26. Domain of analysis for composites containing an embedded sensor or actuator.

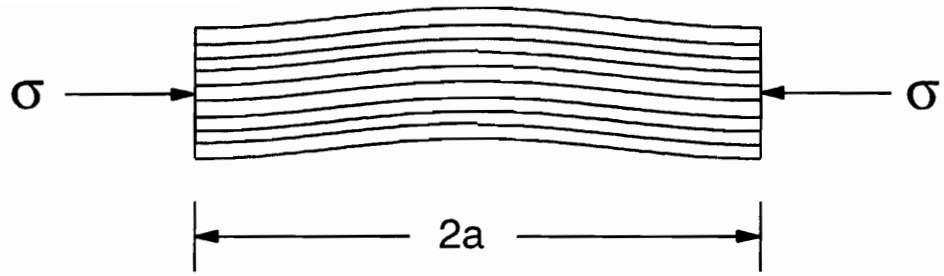

Figure 27. Local buckling of a composite subjected to a compressive load.

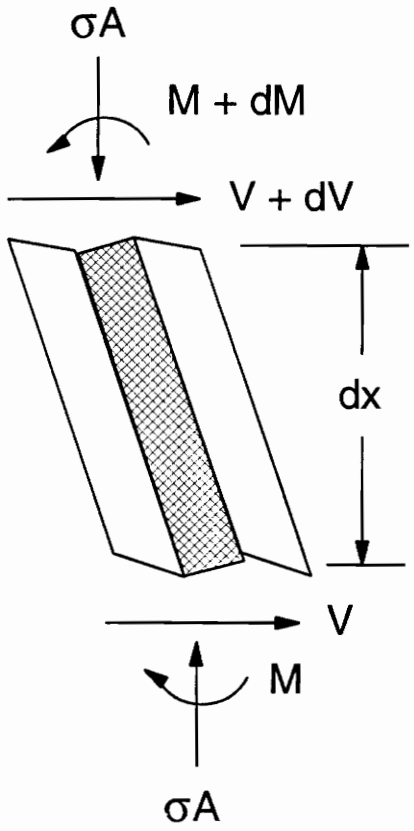

Figure 28. Free-body diagram of a representative volume element of a composite subjected to a compressive load.

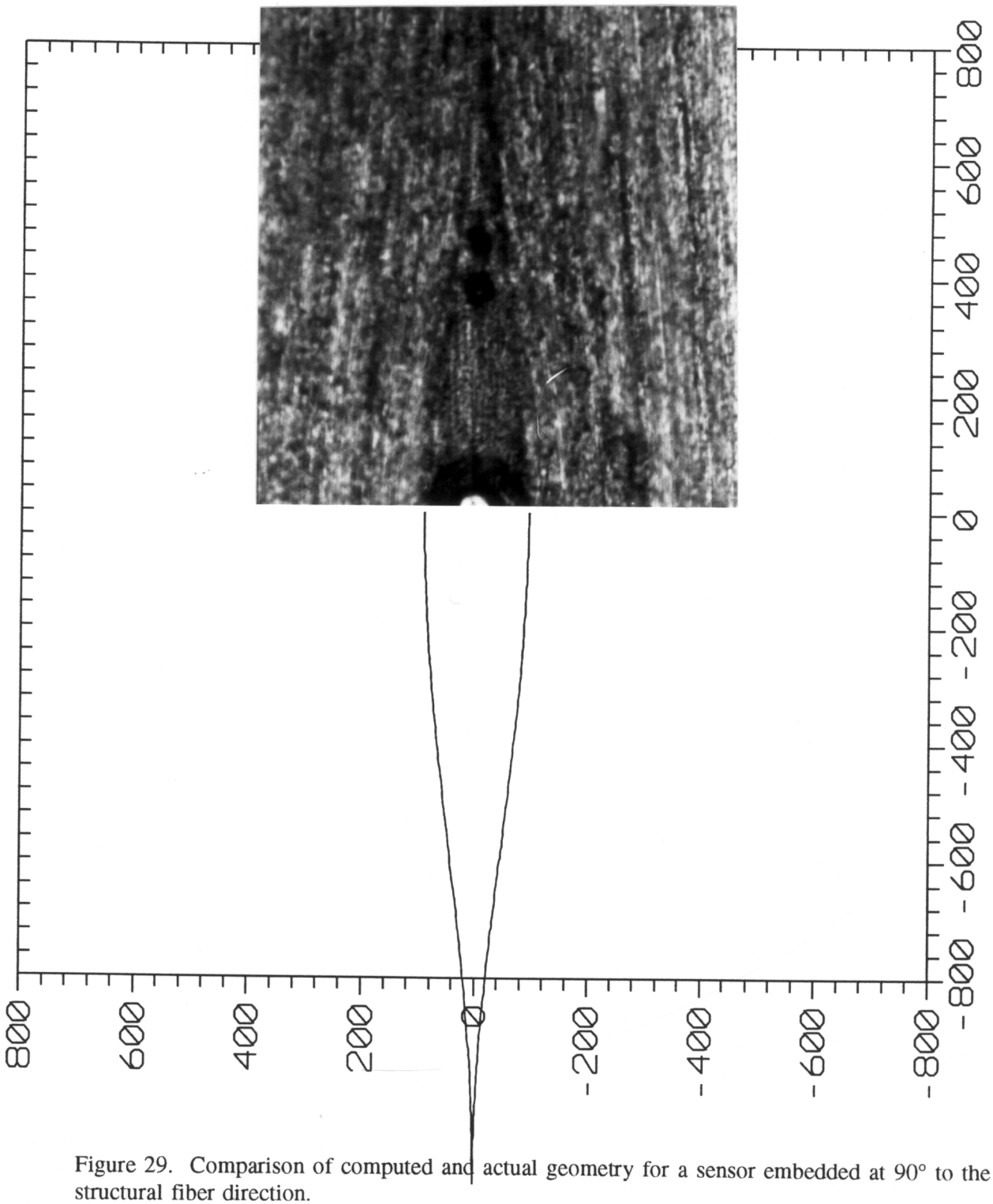

Figure 29. Comparison of computed and actual geometry for a sensor embedded at 90° to the structural fiber direction.

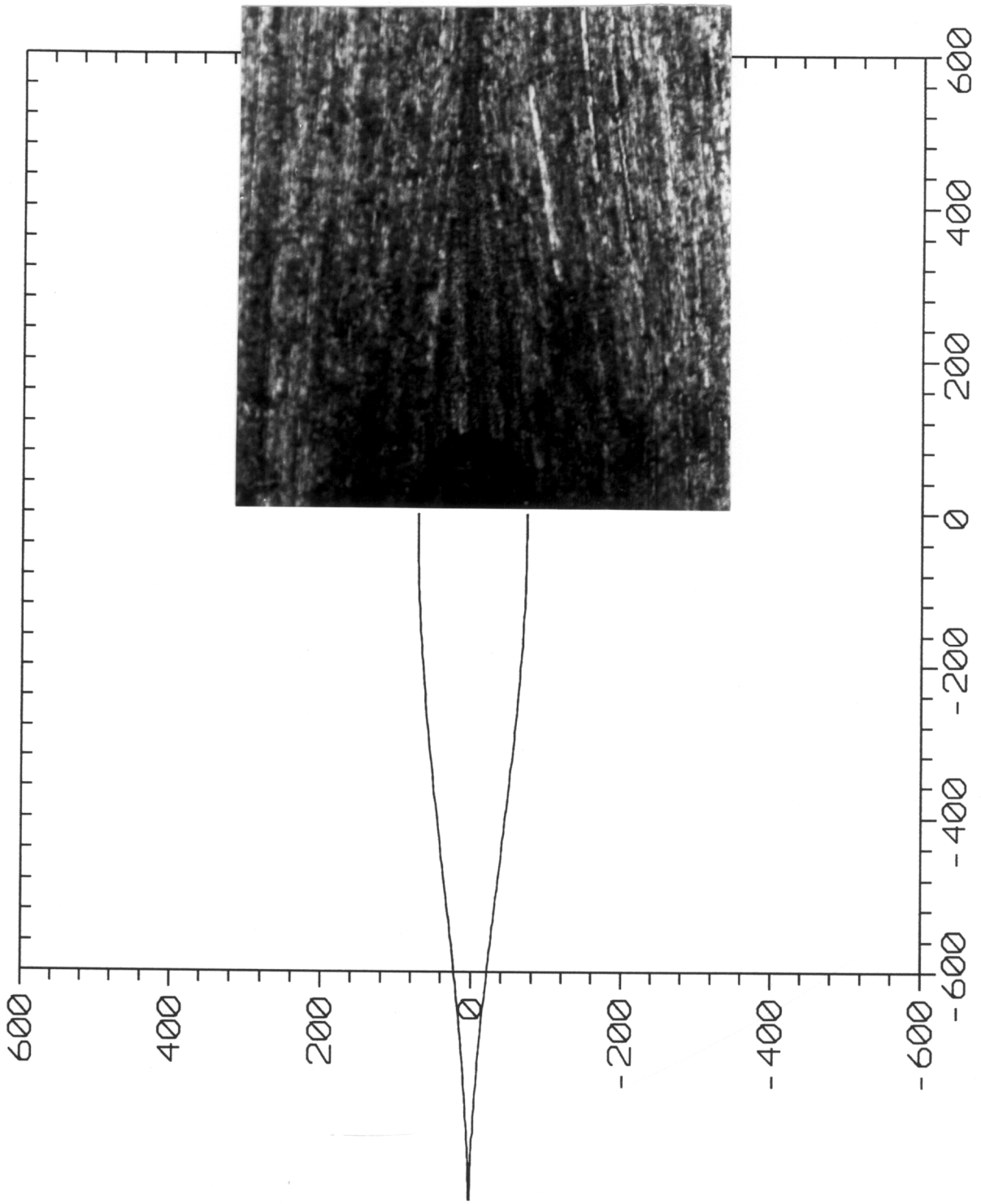

Figure 30. Comparison of computed and actual geometry for a sensor embedded at 45° to the structural fiber direction.

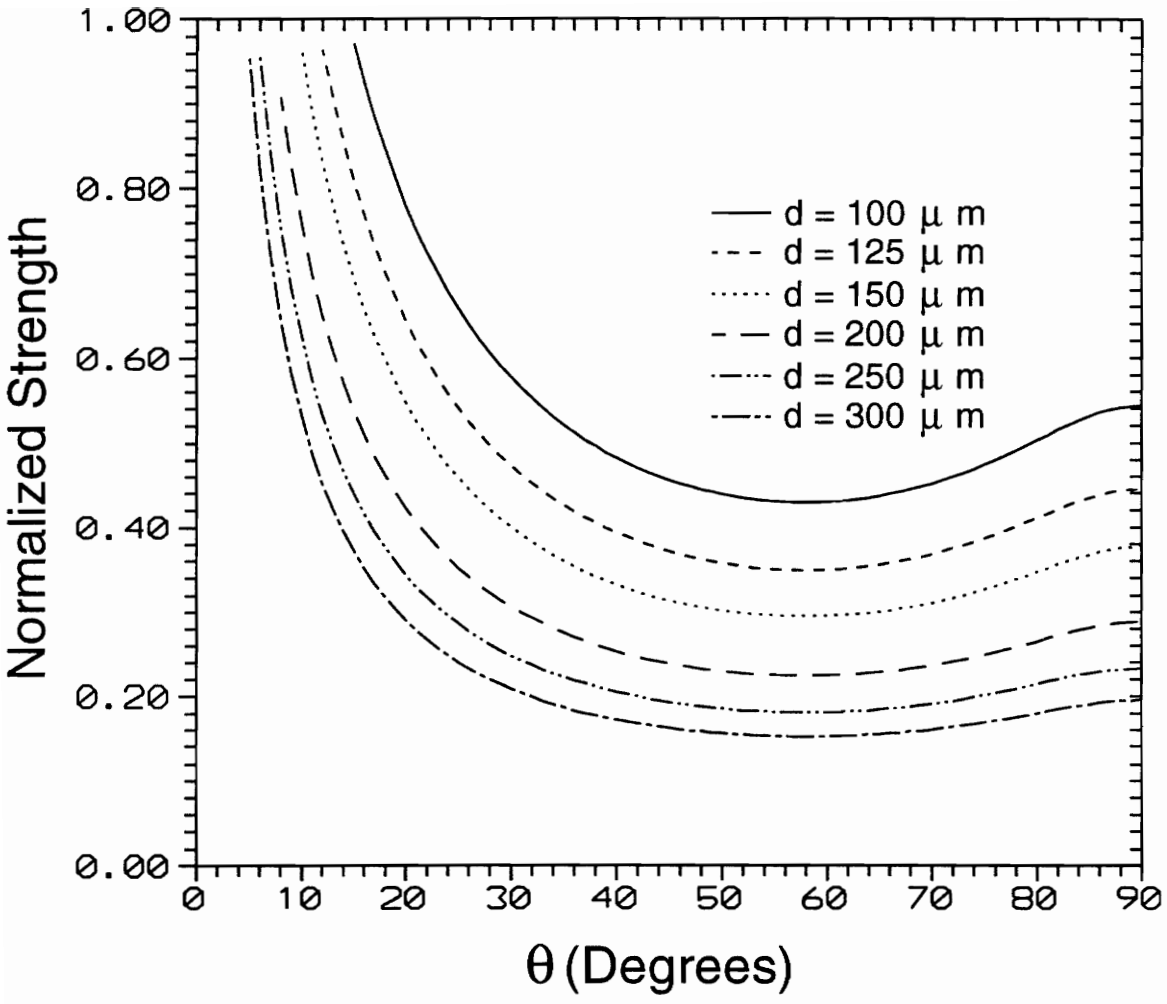

Figure 31. Variation of compression strength with orientation angle, θ, and embedded sensor or actuator diameter, d_0.

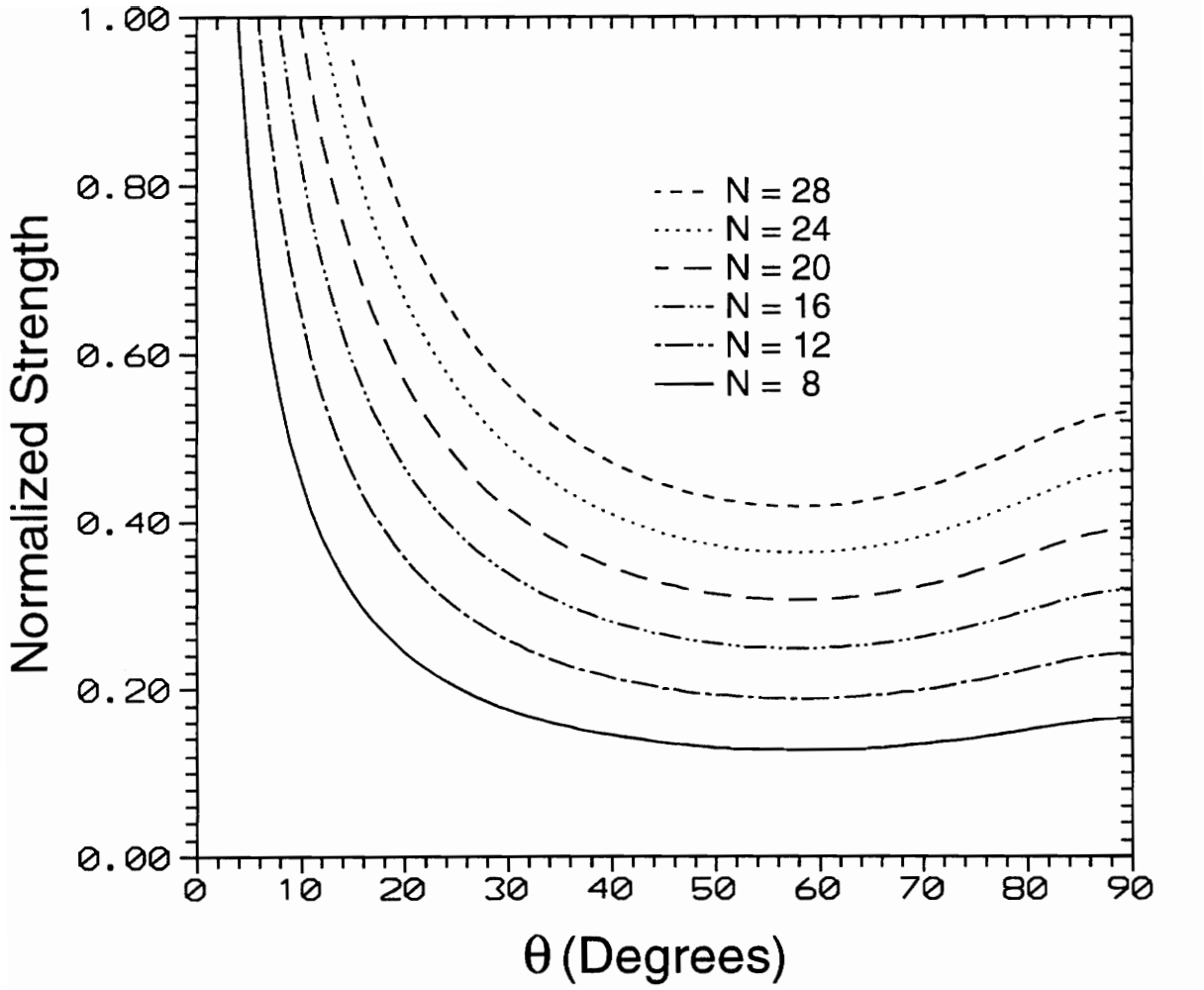

Figure 32. Variation of compression strength with orientation angle, θ, and number of plies, N.

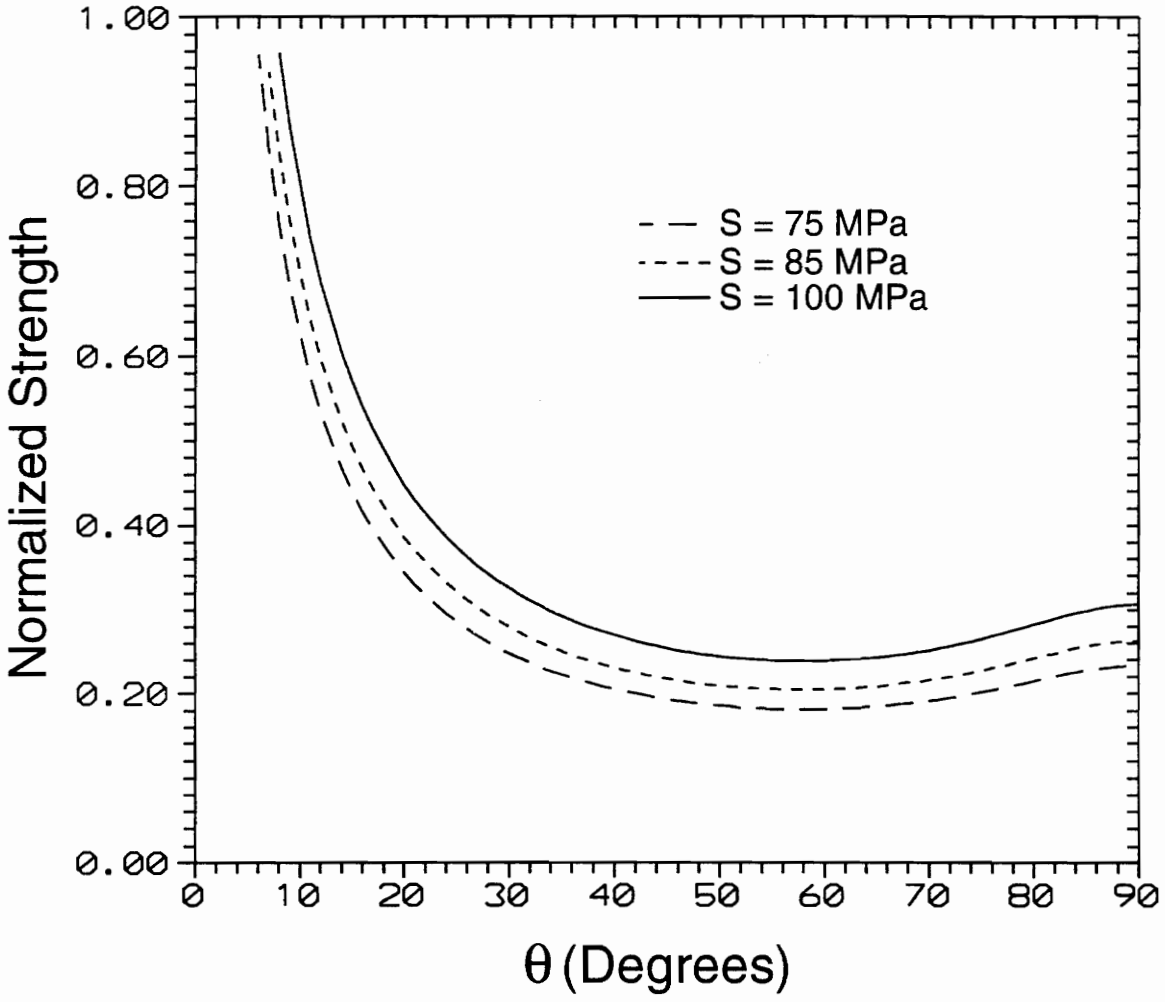

Figure 33. Variation of compression strength with orientation angle, θ, and laminate shear strength, S.

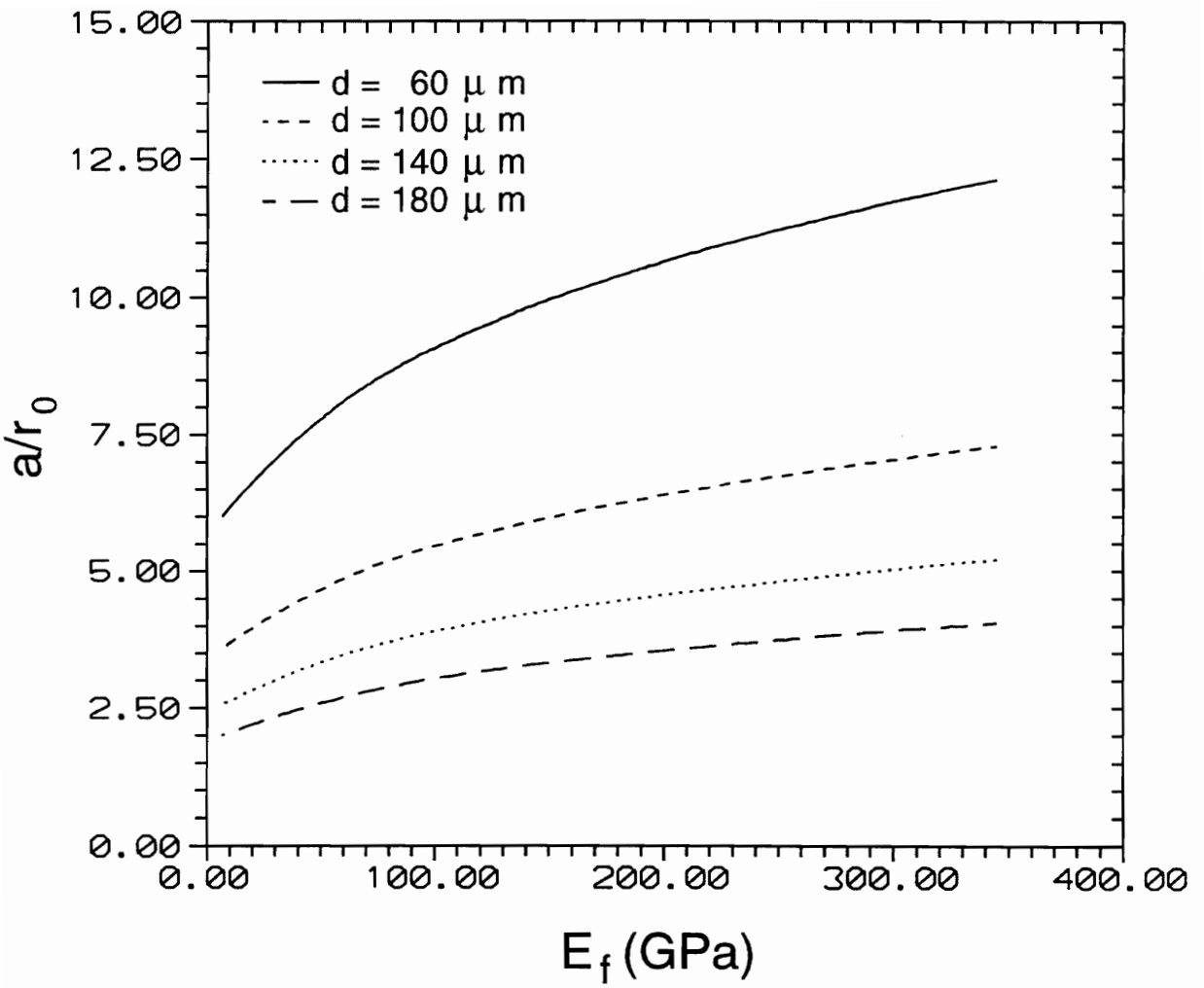

Figure 34. Variation of the normalized undulation size with structural fiber modulus for composites with isotropic structural fibers.

Table 1. Properties of Materials used in fabricating model composites

Material	Young's Modulus E (GPa)	Shear Modulus G (GPa)	Poisson's Ratio ν
7740 Glass	62.7	26.1	0.20
PLM-9 Epoxy	3.3	1.1	0.36

Table 2. Stress concentration and number of fibers adjacent multiple fiber fractures for hexagonal packing

Number of Adjacent Fractured Fibers i	Stress Concentration c_i	Number of Nearest Neighbors n_i
1	1.167	6
2	1.250	8
3	1.333	9
4	1.400	10
5	1.455	11
6	1.545	11
7	1.583	12
8	1.571	14
9	1.643	14
10	1.667	15
11	1.733	15
12	1.750	16

Table 3. Properties of AS-4 Fiber and Epon 828 matrix used in theoretical calculations.

Property	
E_{11}^{f}	235 GPa
E_{22}^{f}	14 GPa
G_{12}^{f}	28 GPa
ν_{12}^{f}	0.20
ν_{23}^{f}	0.25
E^{m}	2.986 GPa
G^{m}	1.075 GPa
ν^{m}	0.35

Table 4. Experimental Results for Model Composite Tests

COMPOSITE	TRANSVERSE MODULUS (GPa)	σ_f (MPa)	ε_f ($\mu\varepsilon$)
Glass/Epoxy v_f = 44% No Interphase	11.6 ± 0.071	6.89 ± 0.63	595 ± 58
Glass/Epoxy v_f = 44% Vacuum Grease	11.9 ± 0.017	16.7 ± 3.04	1411 ± 170
Glass/Epoxy v_f = 25% No Interphase	7.67 ± 0.046	7.40 ± 0.21	976 ± 26
Glass/Epoxy v_f = 25% Vacuum Grease	7.65 ± 0.011	9.66 ± 1.62	1275 ± 212
Wood/Epoxy v_f = 48% No Interphase	7.37 ± 0.010	8.76 ± 0.89	1188 ± 121
Wood/Epoxy v_f = 48% Vacuum Grease	7.36 ± 0.011	10.7 ± 1.95	1453 ± 265

Table 5. Properties of Graphite Epoxy Composite

Property	
E_1	138 GPa
E_2	8.96 GPa
E_y	4.15 GPa
ν_{12}	0.30
G_{12}	7.10 GPa
S	104 MPa

Table 6. Properties of T300/Hexcel F263 Composite

Property	
E_1	135 GPa
E_2	8.65 GPa
E_y	8.65 GPa
ν_{12}	0.30
G_{12}	4.40 GPa
S	81.3 MPa

VITA

Scott Wayne Case was born on February 9, 1970 to Karen and Wilburn Ross Case in Martinsville, Virginia. He grew up in Collinsville, Virginia, a small town in Southwestern Virginia. He attended Fieldale-Collinsville High School, from which he graduated in 1988. Upon graduation, he enrolled as an undergraduate student at Virginia Polytechnic Institute and State University. He completed his B.S. degree in Engineering Science and Mechanics in 1992. During this period he worked as an undergraduate research assistant and then accepted a position as a graduate research assistant in January 1992.

Scott Wayne Case